

STRUCTURE AND DYNAMICS OF INTERFACES IN ORGANIC AND INORGANIC
MATERIALS USING ATOMIC LEVEL SIMULATION

By

DONGHWA LEE

A DISSERTATION PRESENTED TO THE GRADUATE SCHOOL
OF THE UNIVERSITY OF FLORIDA IN PARTIAL FULFILLMENT
OF THE REQUIREMENTS FOR THE DEGREE OF
DOCTOR OF PHILOSOPHY

UNIVERSITY OF FLORIDA

2010

© 2010 Donghwa Lee

To my family with love

ACKNOWLEDGMENTS

I want to show my gratitude to my advisor Prof. Simon R. Phillpot for his kind instruction and all efforts to guide me during Ph. D study. His continuous supports, useful suggestions and helpful discussions have made me pass through all difficulties during my research. I also would like to thank Prof. Susan B. Sinnott for her advices for resolving lots of issues for the study. I also wish to express my appreciation to committee members Prof. Aravind Asthagiri, Prof. David Norton and Prof. Jacob L. Jones.

I cannot resist mentioning all computational science focus group members for their kindness, friendship and supports. From the beginning of my study, they are always my mentors, friends and resources for all kinds. Without their help, I cannot get to this stage.

I personally express my appreciation to my family. My parents have been always mental supporters in my side. I deeply thanks to my wife, Minjung Kim, for all she has made. I never forget how much efforts she spent for me during my graduate study periods.

TABLE OF CONTENTS

	<u>page</u>
ACKNOWLEDGMENTS.....	4
LIST OF TABLES.....	8
LIST OF FIGURES.....	9
ABSTRACT	13
CHAPTER	
1 GENERAL INTRODUCTION	16
1.1 Imperfections In Solids.....	16
1.1.1 Point Defects (0-D)	17
1.1.2 Line Defects (1-D)	18
1.1.3 Interfacial or Planar Defects (2-D)	19
1.1.4 Bulk or Volume Defects (3-D).....	20
1.2 Interface Science	20
2 SIMULATION METHODS	22
2.1 Simulation Methodologies.....	22
2.2 First Principles Calculations.....	23
2.3 Density Functional Theory (DFT).....	26
2.3.1 Hohenberg-Kohn Theorems.....	26
2.3.2 Kohn-Sham Self-Consistent Field Methodology.....	27
2.3.3 Exchange-Correlation Functional	30
2.3.4 Pseudopotentials.....	31
2.3.5 Plane-wave Implementation	32
2.3.6 Linear Scaling	33
2.3.7 Application to LiNbO ₃ Study	35
2.3.8 Application to Molecular Beam Deposition.....	36
2.3.9 Charge analysis Methods.....	37
2.3.10 Limitations on DFT	39
2.4 Molecular Dynamics (MD) Simulation.....	40
2.4.1 Introduction.....	40
2.4.2 Interatomic Interactions	41
2.4.3 Shell Model for Describing Polarizability of Electrons.....	44
2.4.4 Three-body Interactions.....	45
2.4.5 Potential for LiNbO ₃ study	45
2.4.6 Integration Algorithms.....	46
2.4.7 Geometry Optimization.....	49
2.4.8 Thermodynamic Conditions (Ensembles).....	52

3	STRUCTURAL ANALYSIS	54
3.1	Trigonal Ferroelectrics	54
3.1.1	Introduction on LiNbO ₃	54
3.1.2	Crystallography of LiNbO ₃	55
3.1.3	Temperature Effects on LiNbO ₃	63
3.1.4	Domain Walls in LiNbO ₃	65
3.2	Conductive Polymers	67
3.2.1	Introduction	67
3.2.2	Structure of Polythiophene	69
3.2.3	Conduction Mechanism in Polythiophene	71
3.2.4	Growth of Polythiophene	73
4	DOMAIN WALLS IN FERROELECTRIC LITHIUM NIOBATE	76
4.1	Introduction	76
4.2	Domain Wall Preparation	77
4.3	Domain Wall Energy	78
4.4	Atomic Displacement around Domain Walls	80
4.4.1	Y-walls, Parallel to c-glide Planes	81
4.4.2	X-walls, Perpendicular to c-glide Plane	85
4.5	Polarization at Domain Walls	89
4.5.1	Y-walls	90
4.5.2	X-walls	92
4.6	Domain Wall Width	94
4.7	Threshold Field for Domain Wall Motion	96
4.8	Conclusions and Discussion	98
5	DOMAIN WALL-DEFECT INTERACTIONS IN FERROELECTRIC LITHIUM NIOBATE	100
5.1	Introduction	100
5.2	Methodology and Validation	100
5.2.1	Empirical Study with Two Different Methods	100
5.2.2	DFT with Thermodynamic Frame Works	102
5.2.3	Comparison of DFEs of Neutral Defect Complexes	103
5.3	Configurations of Two Different Intrinsic Defect Pairs	105
5.3.1	Li Frenkel Pair ($\text{Li}_i^\bullet + \text{V}_{\text{Li}}'$)	105
5.3.2	Nb antisite Pair ($\text{Nb}_{\text{Li}}^{\bullet\bullet\bullet\bullet} + 4\text{V}_{\text{Li}}'$)	106
5.4	Domain Wall-intrinsic Defect Interactions	109
5.4.1	Y-wall with Individual Point Defects	110
5.4.2	Y-wall with Li Frenkel Pair	111
5.4.3	Y-wall with Antisite ₁ ($\text{Nb}_{\text{Li}}^{\bullet\bullet\bullet\bullet} + 4\text{V}_{\text{Li}}'$)	112
5.4.4	X-walls with Point Defects	113
5.4.5	X-walls with Li Frenkel Pair	114
5.4.6	Two X-walls with Antisite ₁ Pair	115
5.5	Extrinsic Defect, Mg	116

5.5.1 Reaction Schemes with Mg Dopants.....	116
5.5.2 Domain Wall-Mg Dopant Interactions.....	119
5.6 Conclusion.....	124
6 DOMAIN WALLS IN LITHIUM TANTALATE.....	126
6.1 Introduction.....	126
6.2 Potential Development.....	128
6.3 Validation of LiTaO ₃ Potential.....	128
6.4 Energetics of Domain Walls in Lithium Tantalate.....	132
6.5 Domain Wall Structure at Transition State.....	136
6.6 Defects in Lithium Tantalate.....	138
6.7 Conclusion.....	140
7 SURFACE DEPOSITION ON POLYTHIOPHENE MOLECULES.....	142
7.1 Introduction.....	142
7.2 SPIAD.....	143
7.3 C ₂ H ⁺ ion deposition on 3T polymer with PbS nanocrystalline.....	151
7.4 Conclusions.....	152
8 ADATIVE KINETIC MONTE CARLO (AKMC).....	154
8.1 Introduction.....	154
8.2 Mechanism.....	155
8.2.1 Kinetic Monte Carlo (KMC).....	155
8.2.2 Adaptive Kinetic Monte Carlo (AKMC).....	157
8.3 Dimer Method with Two Dimensional Potential.....	158
8.4 Diffusion Process on (111) Aluminum(Al) Surface.....	159
8.5 Conclusion.....	163
9 GENERAL CONCLUSIONS.....	164
9.1 Domain Walls.....	164
9.2 Organic-Gas Interface.....	167
9.3 Metal-gas Interface.....	168
LIST OF REFERENCES.....	170
BIOGRAPHICAL SKETCH.....	187

LIST OF TABLES

<u>Table</u>	<u>page</u>
2-1 The potential parameters for LiNbO_3	46
3-1 Wyckoff positions for R3c	57
3-2 Wyckoff positions for R3c	60
3-3 Comparison of positional parameters of LiNbO_3 between empirical calculations, DFT calculations and experimental data	62
3-4 The comparison on conductivity, stability and Processing attributes of representative conducting polymers	69
4-1 Comparison of constants	97
5-1 DFEs calculated by various methods. The interstitials are places at the center of an empty oxygen cage.....	102
5-2 Lattice energy (eV) per unit formula of oxides for empirical study and DFT	104
5-3 Lattice energy of oxides.....	117
5-4 DFE of isolated defects: comparison of bulk DFEs calculated with a supercell method and the Mott-Littleton method.....	118
5-5 Energies for five reactions, calculated from the DFEs of isolated defects and the bulk lattice energies in Tables 5-2, 5-3 and 5-4.....	118
6-1 The comparison of potential parameters between LiNbO_3 and LiTaO_3	128
6-2 Comparison of structural parameters and elastic properties of LiTaO_3 between experiments and simulations.....	130
6-3 Intrinsic defect formation energies.....	138
6-4 Frenkel, Schottky and pseudo-Schottky defect formation energies.....	139
6-5 Lattice energies of different oxide states	139
6-6 Energies of possible reactions that lead to Li_2O deficiency	140

LIST OF FIGURES

<u>Figure</u>	<u>page</u>
1-1 Various classes of imperfections over the size range.....	16
1-2 Geometrical production of dislocations.....	18
2-1 Flow chart of the Kohn-Sham SCF procedure.....	29
2-2 2D Schematic of the charge neutralization scheme used in the direct sum method	43
2-3 Illustration of potential energy surface of a arbitrary function.....	50
2-4 Schematic of steepest descent method.....	51
3-1 Crystallographic direction of rhombohedral axes and hexagonal axes in a unit-cell of LiNbO_3	55
3-2 Schematic of the paraelectric and ferroelectric phase	58
3-3 [001] projection of the rhombohedral structure	61
3-4 Schematic of Y1, Y2 and Y3 axis along with three oxygen ions, O1, O2 and O3.....	63
3-5 Temperature dependence of polarization of LiNbO_3 from experiment and MD calculation	64
3-6 Schematic of surface charge associated with spontaneous polarization, and formation of 180° domains to minimize electrostatic energy.....	66
3-7 Schematic view parallel to the (0001) plane showing two structurally distinct domain wall structures.....	66
3-8 The comparison of calculated thiophene structure	69
3-9 The structure of terthiophene.....	70
3-10 The variation of polythiophene polymer chain with p-type doping	72
3-11 The variation of electron band during oxidation	73
4-1 Structure of LiNbO_3	77
4-2 Energies of domain walls in equilibrium and in transition states.....	80
4-3 Displacement pattern in z-direction of oxygen ions and cations around Y-wall ..	82

4-4	Atomic displacements of O1, O2 and O3 ions.....	84
4-5	Crystallographies of the X_I -wall and X_{II} -wall.	86
4-6	The Z-displacements patterns around X_I -wall and X_{II} -wall.....	87
4-7	Normal displacements of three different oxygen ions.....	88
4-8	Comparison of z directional polarization (P_z) around Y-walls, determined by DFT and empirical simulation methods	91
4-9	Schematic representation of three different polarization, P_z , P_t and P_n	92
4-10	Comparison on Z directional polarization around X-walls between DFT and empirical simulation methods	93
4-11	A fit of P_z to hyper-tangent function around Y-wall.....	95
4-12	Fits of P_z of X_I -wall and X_{II} -wall.....	96
5-1	DFE comparison of stoichiometric and non-stoichiometric defect pairs in LiNbO_3 using DFT and empirical method	105
5-2	Two different configurations of Li Frenkel pair.....	106
5-3	Different structural arrangements of Nb antisite defect pair.....	107
5-4	The comparison of DFE and association energy	108
5-5	The change in DFE of single point defects near Y-wall	111
5-6	Comparison on DEFs of Li Frenkel pair in two different configurations	111
5-7	Formation energies of Antisite _i clusters as a distance from a Y-domain wall. ..	112
5-8	Variation of DFE of point defects near X_I -wall and X_{II} -wall	114
5-9	DFE of Li Frenkel defect pair near X_I -wall and X_{II} -wall	115
5-10	DFE of Nb antisite defect pair near X_I -wall and X_{II} -wall	116
5-11	The variation of DFE of Mg dopant occupying cation sites near Y-wall.....	120
5-12	Possible arrangement for reaction 1	121
5-13	The variation of DFE of defect pair using reaction 1 near Y-wall.....	121
5-14	Possible arrangement of Mg dopants in LiNbO_3 for reaction 2.....	122

5-15	The variation of DFE of defect pair with reaction 2 near Y-wall	123
5-16	Possible arrangement of Mg dopants in LiNbO_3	123
5-17	The variation of DFE of defect pair with reaction 5 near Y-wall	124
6-1	Different shapes of domains in LiNbO_3 and LiTaO_3	127
6-2	Crystal structure of LiTaO_3 for $+P_s$ and $-P_s$ in z-direction.....	129
6-4	The comparison of normalized polarization between simulation and experiment.....	131
6-5	Domain wall energy comparison in LiTaO_3	133
6-6	Domain wall energy comparison between LiNbO_3 and LiTaO_3	134
6-7	The schematic view of two possible shapes of X-walls	136
6-8	Structural arrangement of cations on the Y-wall plane and the X-wall plane at the transition state.	137
7-1	Comparison between hybridized HF calculation and linear scaled DFT calculation.....	144
7-2	The schematics of two layered structure with four terthiophenes (3T) and five layered structure of thiophene oligomers.....	145
7-3	The angle between incident thiophene ring and substrate 3T ring is determined in order to study angle dependency of reaction	146
7-4	Polymerization between two 3Ts and an incident thiophene.....	148
7-5	Crosslinking between two 3Ts.....	149
7-6	Polymerization between a 3T and an incident thiophene.	149
7-7	Broken 3T chain and an incident thiophene.	150
7-8	The distribution of molecular weight for four different trajectories which lead successful reaction with 3Ts in the substrate.	150
7-9	The iso-surface of electron density.....	152
8-1	Schematic illustration of the procedure for choosing the reaction pathway to advance the system to the next state in the standard KMC algorithm.....	156
8-2	Flow chart illustrating the basic steps in the KMC algorithm.....	156

8-3	The schematic view and flow chart of dimer saddle point searching mechanism	158
8-4	The comparison on searching behavior of dimer method	159
8-5	The schematic view of six layered initial structure on (111) Al surface.....	161
8-6	Two possible adsorption sites for an Al adatom.	161
8-7	Four different diffusion processes of an Al adatom on (111) Al surface	162
8-8	The evolution of time for AKMC simulation.....	163

Abstract of Dissertation Presented to the Graduate School
of the University of Florida in Partial Fulfillment of the
Requirements for the Degree of Doctor of Philosophy

STRUCTURE AND DYNAMICS OF INTERFACES IN ORGANIC AND INORGANIC
MATERIALS USING ATOMIC LEVEL SIMULATION

By

Donghwa Lee

August 2010

Chair: Simon R. Phillpot
Major: Materials Science and Engineering

Interfaces in materials play a key role for industrial applications. The structures and dynamics at various interfaces including ferroelectric domain walls, gas-organic interface, organic-semiconductor interface and metal-gas interface are investigated with different atomic levels of simulation approaches.

Ferroelectricity: Due to their unique ferroelectric and nonlinear optical properties, trigonal ferroelectrics such as LiNbO_3 and LiTaO_3 , are of wide interest for their potential applications in optoelectronics and nonlinear optics. The properties of these materials are heavily influenced by the shape of ferroelectric domains and domain walls. Therefore, investigation of the local structure and energetics of the ferroelectric domain walls and their interaction with defects on atomic scales, which is not clearly understood, is extremely important.

The structure and energetics of ferroelectric domain walls in LiNbO_3 are examined using density functional theory (DFT) and molecular dynamics (MD) methods. The energetically favorable structures of 180° domain walls and the activation energy for domain wall motion are determined by atomic level simulations. The variation of

polarization due to the presence of domain walls is also discussed. Defects can be pinned by domain walls. Various defects-domain walls interactions and the effects on domain wall motion are described using atomic level simulation methods. Although the structure of LiTaO_3 is very similar with LiNbO_3 , it has been said experimentally that the shapes of domain walls are different with the presence of particular defects. Using both DFT and a newly developed interatomic potential for LiTaO_3 , the differences in domain wall structure are understood in terms of the difference in energetics of domain walls between two materials.

Polymerization: Surface polymerization by ion-assisted deposition (SPIAD) enables the control of thin film chemistry and morphology on the nanoscale during growth of conductive polymer thin films. This method allows fine tuning of optical band gaps and other optoelectronic properties of a polymer film by controlling the structure and kinetic energy of the depositing ions and neutrals. Thus, a comprehensive understanding of various mechanisms on the atomic level will contribute to optimizing growth conditions during SPIAD.

SPIAD simulations are performed to study polymerization and crosslinking behavior of polythiophene molecules at the gas-organic interfaces using DFT-MD method. The growth processes for polythiophene molecules are studied by depositing thiophene molecules with 25 eV kinetic energy on terthiophene surface. The mechanism and various processes for polymerization and crosslinking of polythiophenes will be discussed. The changes in bond chemistry at the polythiophene molecules and at a PbS nanocrystalline quantum dot (organic-semiconductor interface) after a collision of C_2H^+ molecules with the substrate are also addressed.

Surface diffusion: Surface diffusion is a key concept for understanding catalytic behavior at the surface. We develop a new code implementing adaptive kinetic Monte Carlo (AKMC) method with the dimer transition searching mechanism. The code is developed with a simple Lennard-Jones (LJ) potential. A test of dimer method is performed by using 2-dimensional testing potential. Results of surface diffusion processes of an Al adatom on Al (111) surface using AKMC method are presented.

CHAPTER 1
GENERAL INTRODUCTION

1.1 Imperfections In Solids

Colin Humphreys said “Crystals are like people, it is the defects in them which tend to make them interesting!”. As we can see from thermodynamics, real crystals are never perfect: they always contain defects. Defects can exist in varieties of types inside materials and can have a profound impact on the macroscopic properties of materials. Although some defects act as the origin of beautiful colors in many minerals or the conductivity in ionic conductors, many natural defects degrade the properties of materials and make them difficult for industrial usage. However, as we can control these defects, we can capture the desired properties of materials for specific applications. Therefore, understanding imperfections is an important problem for material scientists and engineers. Defects can be categorized by the dimensionality also; 0-dimension (0-D), 1-dimension (1-D), 2-dimension (2-D) and 3-dimension (3-D). The size range over different classes of defects is shown in figure 1-1.

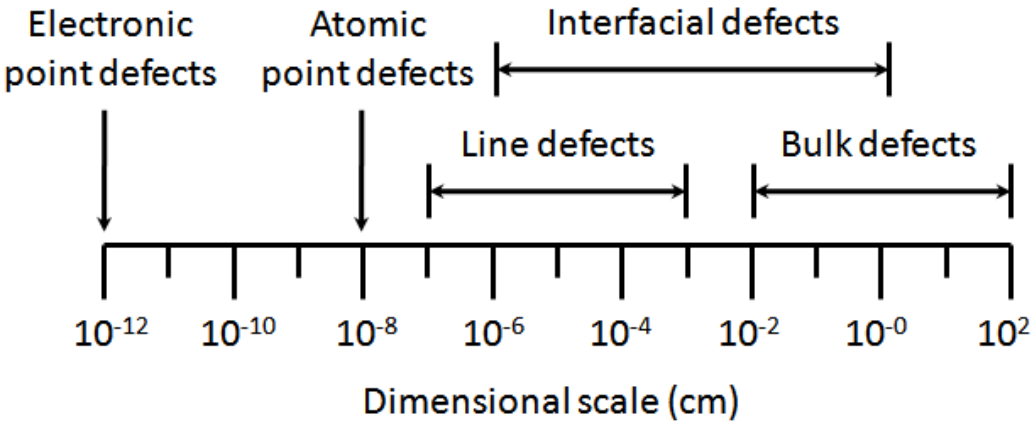


Figure 1-1. Various classes of imperfections over the size range[1]

1.1.1 Point Defects (0-D)

A crystal has a localized defective region of atomic dimensions, the region is termed a point defect. Different types of point defects exist, including vacant lattice sites, and extra or missing atoms or electrons, and foreign atoms.

Vacancies: A vacancy is a lattice position which is vacant because of thermally induced diffusion of atoms. It can be also described to off-stoichiometry. The number of vacancies formed by thermal agitation can be understood as

$$N_V = N_A \times \exp\left(\frac{-Q_V}{KT}\right) \quad (1-1)$$

Where N_A is the total number of atoms in a solid, Q_V is the energy to form a vacancy, K is the Boltzmann constant, and T is the temperature.

Vacancies are important because they can determine the diffusion rate in the matrix.

Interstitials: An interstitial atom occupies a site other than a normal lattice position. An interstitial atom can be either the same type of atom (self interstitial) or foreign atom (impurity).

Impurities: An impurity atom is a non-matrix atom which is not present in pure crystalline materials. Impurities atoms can be found at either vacancy or interstitial sites. Because they are electronically different, they would cause a difference in property, even mothered lattice structure.

While vacancies and self-interstitials are considered as intrinsic point defects, impurities are regarded as extrinsic point defects. Point defects apply strain to neighboring atoms, cause the distortion of structure, and affect the properties of materials.

1.1.2 Line Defects (1-D)

Line defects are defective regions of the crystal along a line. The line does not need to be straight; it can be curved or even form a closed loop. The line defects are often referred to as dislocations; disclinations are another type of line defects, however they are only important in liquid crystals. Because dislocation lines show abrupt changes in the regular ordering of atoms, they cause a change in density and their motion lead to changes in mechanical properties of material. They can be categorized into three different types depending on how the atoms displace along the dislocation line; edge dislocation, screw dislocation and mixed dislocation.

Edge dislocation: When atoms are displaced in a direction perpendicular to the dislocation line, the dislocation is termed an edge dislocation, see figure 1-2(a). Edge dislocations occur with an extra atomic plane.

Screw dislocation: If the atom displacement is parallel to dislocation line, the dislocation is called as a screw dislocation, see figure 1-2(b). Screw dislocations result from shear displacement of atoms.

Mixed dislocation: When atoms are displaced at some angle to the dislocation line, it can have both edge and screw components.

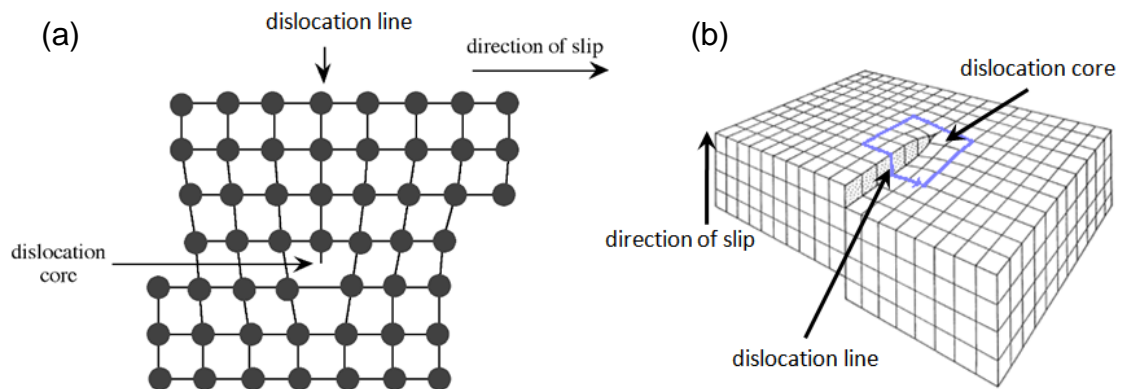


Figure 1-2. Geometrical production of dislocations.[1]

1.1.3 Interfacial or Planar Defects (2-D)

Interfacial or planar defects in solids can be categorized into three different types; interfaces, domain walls and grain boundaries.

Interfaces: Interfaces between solid and gas are called free surfaces. Because the environment of an atom at a surface differs from that of an atom in the bulk, the structure near the surface has a slightly larger lattice parameter than in the interior. The unsatisfied atomic bonds at the surface yield the surface energy, γ . The densest atomic density plane usually shows the lowest surface energy. The surface energy is normally in the range of a few J/m^2 .

Ferroelectric Domain walls: A change in electronic structure, chemical composition or atomic arrangement across the interface leads to interphase boundaries. In particular, the interface, leading a change in the atomic arrangement but no change in the symmetry of the crystal structure, is a ferroelectric domain wall. More details on ferroelectric domain walls are given in chapter 3.

Grain boundaries: Grain boundaries are planar defects which separate regions of different crystallographic orientations. A grain is a region of crystal in which the principal crystallographic directions do not change. Because of the different crystallographical orientation of each grain, the grain boundaries lead to atomic mismatch at the interfaces and create lower density structures. Grain boundaries are typically very reactive, so that point defects are usually segregate there. The interaction between interfaces and point defects affects properties of materials.

1.1.4 Bulk or Volume Defects (3-D)

Bulk defects are generally created during production of materials such as casting, forging, and rolling. Three common types of bulk defects are inclusions, cracks and pores.

Inclusion: An inclusion is an unwanted second-phase particle which is produced during material processing. Inclusions can be found in a variety of shapes and sizes in crystals.

Cracks: A crack is the region where material has fractures or discontinuities. Cracks are normally created by either mechanical or thermal stresses during forging or welding. Since cracks can propagate with the external load, they affect the mechanical properties.

Pores: Pores are generated during the solidification process. The void created by the volume change from liquid to solid remains as pores in a solid. Pores can affect optical, thermal and mechanical properties.

1.2 Interface Science

Interface science is the study of physical and chemical phenomena that occur at the interface of two phases such as domain walls, organic-gas interfaces, organic-semiconductor interfaces and solid-gas interfaces. As advanced materials become increasingly multifunctional, there is a concerted focus on the influence of interfaces. Interfaces not only change mechanical properties of materials, such as elasticity, impact strength, and wear resistance, but also affect electrical and optical properties, such as electrical conductivity, polarizability and refractive index. To tailor the interfacial properties of materials, it is therefore necessary to have a solid fundamental understanding of atomistic phenomena at the interface. For ferroelectric materials, two

oppositely polarized ferroelectrics will have internal interfaces known as ferroelectric domain walls. Therefore, the first system to be addressed in this dissertation is domain wall structures and properties in LiNbO_3 , which is a widely used material for micro-actuators or optical filters. This understanding will help for its potential usage for ferroelectric random access memory (FeRAM) or optical switch. We also perform a study on LiTaO_3 which has very similar structure but different material properties. The difference in material properties of LiNbO_3 and LiTaO_3 are understood by atomic level simulation. Defects-domain wall interactions can change the properties of ferroelectric materials. Thus, the next study in this thesis, I address the interaction between point defects (intrinsic and extrinsic) and domain walls in LiNbO_3 .

The next interfacial study is the deposition kinetics on a gas-polymer interface. The deposition of polymer particles into the conductive polymer chain is performed to understand polymerization and cross-linking process of polythiophene polymers. Because polythiophene is one of the most widely studied conductive polymers for diverse electronic application areas, such as organic light emitting diode and photovoltaic devices, the deposition of thiophene molecules on the terthiophene (3T) substrate is studied. The variation of chemical bonding at the gas-semiconductor interface is also studied in order to understand the electronic conduction mechanism between conductive thiophene polymer chains and nanocrystalline quantum dots.

The third and last area, which this theses address is the diffusion process of adsorbed particle on the FCC (111) surface. For this study, an effective tool for studying surface migration is developed. The diffusion kinetics of an aluminum (Al) adatom on Al (111) surface is studied.

CHAPTER 2 SIMULATION METHODS

2.1 Simulation Methodologies

Various simulation methodologies have been developed to elucidate materials' behaviors over a wide length scale and time scale. Atomic simulation is a powerful method to investigate structure and energetics of materials. On the scale of atoms, two types of simulation methods are widely performed; considering interactions between essentially structureless atoms with empirical potentials (atomistic methods) or considering the interactions between atoms and electrons explicitly (electronic structure method). For the atomistic methods, the interactions between atoms are simplified by using empirical potentials. The atomistic method can be performed quickly without high computational load. However, the choice of empirical potential is critical for the accuracy. The electronic method can improve the accuracy by considering electron-electron interactions. However, the computational demands for calculating electron-electron interactions are extremely high, thus limiting its application to small system sizes for prototype study. Thus, density functional theory (DFT), which regards the electron-electron interactions as interactions between electron and electronic density, is developed. DFT improves the efficiency of electronic methods by reducing significant amount of time and resource required, and makes it possible to perform the electronic structure calculations on several hundred atomic system. In this study, empirical and DFT methods are used to study the structure and energetics of materials.

Molecular dynamics (MD) simulations with DFT rather than empirical methods enables a different level of dynamic studies. Typically, MD simulations are performed in small range of time scales ($\sim 10^{-9} \sim 10^{-12}$ s), because they predict the atomic behavior

from reproducing the vibration of each atom species; the characteristic vibrational period being $\sim 10^{-13}$ s. In this study, MD simulations combined with density functional theory (DFT) are performed in order to study dynamic process in materials, including chemical reactions, polymerization, crosslinking and charge transfer at the interface.

Rare kinetic events happening at longer time scale ($10^{-3} \sim 10^{-6}$ s) can be also explored either with temperature accelerated dynamics (TAD) or with Adaptive Kinetic Monte Carlo (AKMC) methods. Electronic and atomistic scale modeling is used to understand structure, energetics and bonding chemistry of material properties in detail; AKMC and TAD are used to predict the kinetic process and unknown rare events. In this study, the newly implemented AKMC method into empirical potential is used in order to interpret the surface diffusion process of a particle on a metal surface.

2.2 First Principles Calculations

First principles calculations refer to calculations made by considering the interactions of electrons and nucleus in a system by solving Schrödinger's equation[2] within a set of approximations.

The time-dependent Schrödinger equation for a general quantum system can be written as: [3]

$$i\hbar \frac{\partial}{\partial t} \Psi = \hat{H} \Psi \quad (2-1)$$

where \hat{H} is the Hamiltonian operator, Ψ is the wave function and $i\hbar \frac{\partial}{\partial t}$ is the energy operator. For a single particle in a potential V , equation (2-1) can be rewritten as:

$$i\hbar \frac{\partial}{\partial t} \Psi = \frac{-\hbar^2}{2m} \nabla_i^2 \Psi + V(r_i) \Psi \quad (2-2)$$

where m is the mass of the particle. The first term and second term on the right side of the equation (2-2) represent the kinetic energy and potential energy of the system respectively.

For a few specific cases such as a hydrogen atom, equation (2-2) can be solved. However, for more complex systems, it is impossible to obtain the analytic solution for equation (2-2). If we assume the wave function separated from a time dependent eigenfunction, we can change the wave function in equation (2-2) to the time-independent eigenfunction. The Born-Oppenheimer approximation[4] allows the wave function of molecule to be separated into electronic and nucleus components, the equation (2-2) can be expanded to:

$$\left[\frac{-\hbar^2}{2m} \sum_{i=1}^N \nabla_i^2 + \sum_{i=1}^N V(r_i) + \sum_{i=1}^N \sum_{j<i}^N U(r_i, r_j) \right] \psi = E \psi \quad (2-3)$$

where, m is the mass of electron and N is the total number of electrons in the system. The individual terms in the Hamiltonian in equation (2-3) are, in order, the kinetic energy of each electron, the electron-nuclei interactions, and the electronic-electron interactions respectively. We can separate the electrons into two categories: core and valence electrons. The valence electrons represent for the electrons at the outmost shell and the core electrons term the electrons at the inner shell. Intuitively, the core electrons of an atom are only weakly perturbed by chemical reactions, geometry and bonding changes. Thus, several approximations are developed in order to reduce the computational expense by treating them only approximately. The simplest level of approximation is the frozen-core approximation which treats the electron occupancy of core states as fixed. Alternatively, we can use an effective potential, combining opposite

sign charges between core electron and nucleus, a so called pseudopotential. We give more detail on pseudopotentials in Sec. 2-3-4.

The electron-electron interaction is the most challenging and computationally expensive calculation. It requires various assumptions for the solution, since the interaction of each wave function with all other electrons has to be considered. The total wave function ψ can be denoted by a function of the spatial coordinates of the N electrons:

$$\psi = \psi(r_1, r_2, \dots, r_N) \quad (2-4)$$

With the Hartree product, the equation (2-4) can be approximated as a product of individual wave functions[5]:

$$\psi = \psi_1(r)\psi_2(r)\dots\psi_N(r) \quad (2-5)$$

While the Hartree product approximation is fairly convenient, it fails to describe the antisymmetric condition of the wavefunction of fermions. The Hartree-Fock method was developed to overcome this problem. In Hartree-Fock calculations, the one-electron wave functions are approximated by linear combination of atomic orbitals. Commonly, the atomic orbitals are assumed to be composed of a linear combination of Gaussian type orbitals. Various types of sets of Gaussian functions, known as basis sets, have been developed and incorporated in configuration interaction (CI), coupled cluster (CC), Moller-Plesset perturbation theory (MP), and the quadratic configuration interaction (QCI) approaches[6]. Although different basis sets have been suggested, molecular Hartree-Fock calculations are not used in most modern simulations due to the high numerical costs.

An alternate formalism has been developed based on the probability of finding an electron at a particular system coordinate. The electron density at a particular position r in space can be given as:

$$n(r) = 2 \sum_i \psi_i(r) \psi_i^*(r) \quad (2-6)$$

where, the asterisk indicates the complex conjugate of the wave function. The prefactor of 2 in equation (2-6) comes from the electrons of two different spin states which can occupy each orbital. The use of the electron density reduces the many body problems of N electrons with $3N$ spatial coordinates to 3 spatial coordinates. This idea is the foundation of density functional theory (DFT).

2.3 Density Functional Theory (DFT)

Density functional theory (DFT) is a method to investigate the ground state electronic structure using quantum mechanical theory. With this theory, the properties of a many-electron system are determined by the spatially dependent electron density. DFT is among the most popular and versatile methods available in many different area including condensed-matter physics, computational physics, and computational chemistry.

2.3.1 Hohenberg-Kohn Theorems

Although early DFT has conceptual roots in the Thomas-Fermi model, its modern form originates from two different Hohenberg-Kohn theorems[7].

Hohenberg-Kohn Existence theorem: “*the ground-state energy from Schrödinger’s Equation is a unique functional of the electron density, $n(r)$.*” This means that ground state properties of a many-electron system are uniquely determined by an electron density that depends on only 3 spatial coordinates. Also, they noted that the

integrals' density is the number of electrons in the system. The Hamiltonian operator and the electron density are sufficient to determine the energy. Thus, DFT theorem can be extended to excited states as well as ground state.

Hohenberg-Kohn variational theorem: The second Hohenberg-Kohn theorem is that the density obeys a variational principle. The energy, determined from Hamiltonian with any given density, must be equal to or greater than the ground-state energy. So, we can minimize the energy functional by choosing different densities. The energy functional is determined by classical interaction by three different terms: the attraction between the density and the nuclei, the self-repulsion of a classical charge distribution, and the kinetic energy of a continuous charge distribution.

2.3.2 Kohn-Sham Self-Consistent Field Methodology

Based on the Hohenberg-Kohn theorem, the electron density determines the ground state originated from many electron wave function. However, we still need to include the electron-electron interaction term of Schrödinger equation. In 1965, Kohn and Sham[8] suggested a simple model for solving the electron-electron interaction using a Hamiltonian operator which expressed as a hartree product of one-electron operators. The energy functional can be divided into two parts as:

$$E[\{\psi_i\}] = E_{known}[\{\psi_i\}] + E_{xc}[\{\psi_i\}] \quad (2-7)$$

Where,

$$E_{known}[\{\psi_i\}] = \frac{-\hbar^2}{m} \sum_i \int \psi_i^* \nabla^2 \psi_i d^3 r + \int V(r) n(r) d^3 r + \frac{e^2}{2} \iint \frac{n(r)n(r')}{|r-r'|} d^3 r d^3 r' + E_{ion} \quad (2-8)$$

and $E_{xc}[\{\psi_i\}]$ is all of the non-classical corrections to the electron-electron repulsion energy. The terms in equation (2-8) are, from left to right, the kinetic energy of non-

interacting electrons, the Coulomb interaction between the electrons and nuclei, the classical electron-electron repulsion, and the correction to the kinetic energy deriving from the interacting nature of the electrons. $E_{XC}[\{\psi_i\}]$ defines all other interactions not included by equation (2-8), and is referred to as the exchange-correlation energy. In order to solve for $E_{XC}[\{\psi_i\}]$, Kohn-Sham used a set of equations involving only single electrons. Therefore, equation (2-3) can be modified by the Kohn-Sham one-electron operator. The Kohn-Sham equation can be written as:

$$\left[\frac{-\hbar^2}{2m} \nabla^2 + V_{ion}(r) + V_H(r) + V_{XC}(r) \right] \psi_i(r) = \varepsilon_i \psi_i(r) \quad (2-9)$$

where $V_{ion}(r)$ is the electron-ion potential, $V_H(r)$ is the Hartree potential, $V_{XC}(r)$ is the exchange-correlation potential, ε_i is the Kohn-Sham eigenvalue, and ψ_i is the wave function of state i . $V_{ion}(r)$ represents the attraction between a single electron and nuclei and can be expressed as:

$$V_{ion}(r) = \sum_n^{nuclei} \frac{Z}{|r - r'|} \quad (2-10)$$

$V_H(r)$ represents the repulsion of a single electron from electron density and is given by:

$$V_H(r) = e^2 \int \frac{n(r')}{|r - r'|} d^3 r' . \quad (2-11)$$

The exchange-correlation potential is the functional derivative of exchange-correlation energy as the one-electron operator and is given as:

$$V_{XC}(r) = \frac{\delta E_{XC}(r)}{\delta n(r)} . \quad (2-12)$$

where, $E_{xc}(r)$ is exchange-correlation energy.

Even though equation (2-9) looks very similar to equation (2-3), there is one very important difference: equation (2-3) considers the interaction of two wave functions of electrons. However, the Kohn-Sham equation considers a single electron interacting with the electron density. Thus, a set of the interactions between two electron wave functions can be replaced by electrons interacting with the electron density. So, increasing the number of electrons in the system only increases the number of single-particles for equation (2-9). This will improve the computational scales from N^4 to N^3 by. The Kohn-Sham Self-Consistent Field procedure can be summarized as figure 2-1.

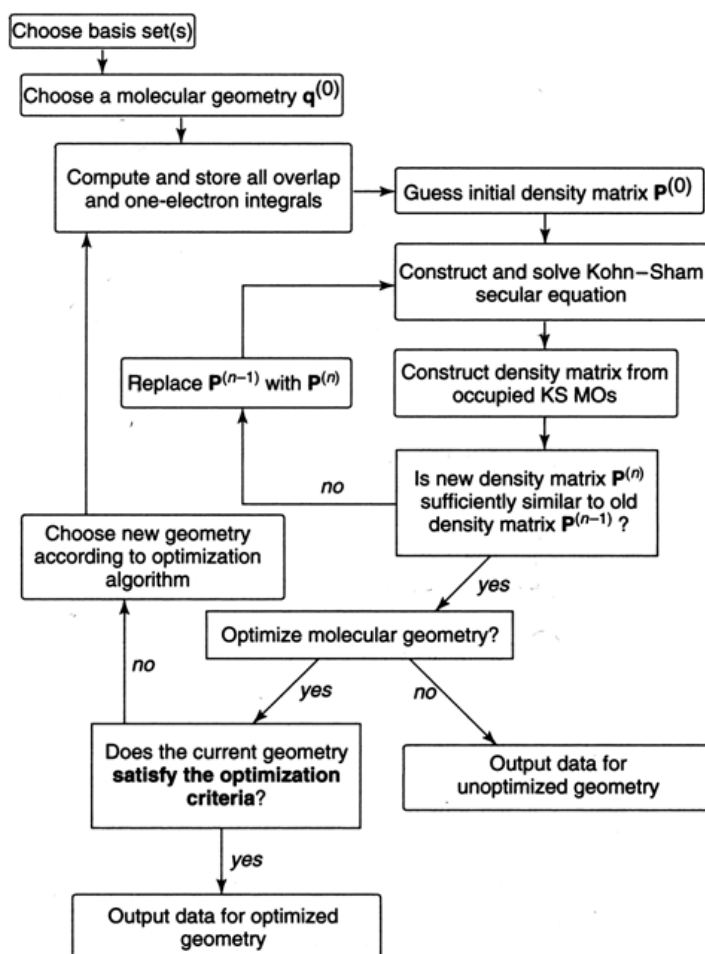


Figure 2-1. Flow chart of the Kohn-Sham SCF procedure.[9]

2.3.3 Exchange-Correlation Functional

The Exchange-correlation term, $V_{XC}(r)$, represents both the difference between the classical and quantum mechanical electron-electron repulsion and the difference in kinetic energy between the fictitious non-interacting system and the real system. However, in most modern functionals, the energies for this portion is replaced by values obtained under specific conditions instead of solving them explicitly. The exchange-correlation energy functional, E_{XC} , can be expressed as an interaction between the electron density and energy density, ε_{XC} .

$$E_{XC}[n(r)] = \int n(r) \varepsilon_{XC} n^*(r) dr \quad (2-13)$$

where, ε_{XC} is a sum of individual exchange and correlation contributions.

Although the exact exchange-correlation functional varies, DFT determines $E_{XC}[n(r)]$ by making reasonable approximations. Needless to say, it is important to choose a good exchange-correlation approximation for the system.

One of the most common approximations used in DFT calculation is the local density approximation (LDA). In LDA, the energy density at some position r is computed exclusively from the value of the electron density at that position. LDA is derived from the homogeneous electron gas in which the density has the same value at every position. In a molecular system, the electron density is normally far from homogeneous, so the LDA approach has the limitations. A more sophisticated approximation to improve the exchange-correlation functional is to consider the change in the local density using the gradient of the density. The gradient correction in the density defines the generalized gradient approximation (GGA) [10]. The gradient corrected functional is added to the LDA functional, i.e.,

$$\varepsilon_{XC}^{GGA}[n(r)] = \varepsilon_{XC}^{LDA}[n(r)] + \Delta\varepsilon_{XC} \left[\frac{|\nabla n(r)|}{\rho^{4/3}(r)} \right] \quad (2-14)$$

Although GGA treat the exchange-correlation functional in a more sophisticated manner, GGA does not always provide a more accurate description of all systems[6]. Therefore, choosing the most appropriate exchange-correlation functional for the system is important.

2.3.4 Pseudopotentials

Although we simplified the Schrodinger equation using the Kohn-Sham Theorem, all electrons must be included to solve the equation. Intuitively, we expect the core electrons of an atom to interact with other atoms less strongly. Therefore, we can use a pseudopotential to simplify the calculation. The basic concept of a pseudopotential is to replace the exact potential, created by the attraction between nucleus and core electrons and repulsion between core electrons, with an effective potential. Thus, the pseudopotential reduces the calculation time during self-consistent field method. There are four different requirements for generating pseudopotentials.

- 1) Boundary matching: the angular momentum of all-electron and pseudo-wavefunction must match at the boundary between core and valence electrons
- 2) Smoothness: Pseudo-wavefunction should not have a maximum within the core radius
- 3) Eigenvalue matching: the eigenvalues of pseudo-wavefunction must match the all electron values at the chosen atomic reference state.
- 4) Norm-conservation: The valence electron density at core region should be equal in the pseudopotential and in the all electron cases.

2.3.5 Plane-wave Implementation

Although we have reduced the number of electrons for solving the Schrödinger equation of system by using Kohn-Sham equation and a pseudopotential, the calculation for many-electron systems is still challenging. One of the methods to enable the calculation is the plane-wave approach for the wave function (ψ). A plane wave is a constant frequency wave having constant amplitude normal to the phase velocity vector. For periodic systems, such as a solid, the wave function can be described as a plane wave[11] which has the following form:

$$\psi_{j,k}(\mathbf{r}) = U_j(\mathbf{r}) \cdot e^{i\mathbf{K} \cdot \mathbf{r}} \quad (2-15)$$

where, U_j is a lattice periodic component, $i = \sqrt{-1}$, and K is the plane wave vector. The plane wave vector K is the reciprocal of wavelength and the direction of vector indicate the direction of wave propagation. Expressing the lattice periodic component as a sum of discrete plane-wave basis sets with the reciprocal lattice vectors of the crystal, G , equation (2-15) can be rewritten as:

$$\psi_{j,k}(\mathbf{r}) = \sum_G C_{j,K+G} \cdot e^{i(\mathbf{K}+\mathbf{G}) \cdot \mathbf{r}} \quad (2-16)$$

where $C_{j,K+G}$ is the plane-wave coefficient.

The dimension of the plane-wave basis sets should be infinite for an exact solution. Truncating the basis set is required for computational schemes. The basis sets can be reduced by defining an energy cut-off given by $|\mathbf{K} + \mathbf{G}|^2 / 2 \leq E_{cut}$. In practice, plane-wave basis sets are often used in combination with a pseudopotential, so that the plane waves are only used to describe the valence charge density. The advantage of plane-wave basis sets is that all functions in the basis are mutually orthogonal, so it

does not show a basis-set superposition error. Also, derivatives are computationally less expensive, because plane wave basis sets can use Fast Fourier Transforms (FFT). Another important advantage of a plane-wave basis is convergence to the target wavefunction. However, plane wave basis sets are less suitable for gas-interface calculation because it requires increased number of calculations over the vacuum space.

For a periodic system, the integrals over infinitely extended system are replaced by integrals over the finite first Brillouin zone in reciprocal space. Such integrals are performed by summing the electron density at a finite number of points in the Brillouin zone, called the k-point mesh[12]. The integrations are replaced by the summations of Fourier transform at a finite number of K-points:

$$\int_{BZ} F(\mathbf{K}) d\vec{K} = \frac{1}{\Omega} \sum_j w_j F(\mathbf{K}_j). \quad (2-17)$$

where, $F(\mathbf{K})$ is the Fourier transform of an integral function such as electron density or total energy, Ω is the supercell volume, and w_j is the weighting factor. Choosing the k-point mesh appropriately is crucial for the convergence of the results, requiring convergence tests. Since the wave functions at closely spaced K-points are nearly identical, it turns out that only a few K-points are typically necessary to describe the whole reciprocal space.

2.3.6 Linear Scaling

Because plane wave DFT requires solving the wavefunction of Kohn-sham equation via density fitting, it scales as the cube of the number of atoms (or electrons) of the system[2]. As the system size increases, determining the eigenvalues and eigenvectors will be the major cost. This makes it very difficult to reach system sizes larger than a few hundreds atoms, and is therefore a huge barrier for the study of many

problems in nanoscale materials. In order to overcome this limitation, locality is considered in real space. If we assume that an atom only interact with other particles (electrons and nuclei) within a given radius, then the number of interactions per atom remains constant, regardless of the system size. In other words, the total cost for the calculation will scale linearly with the dimension of the system. One might also think of how the central role of the long-ranged Coulombic potential in the Hamiltonian is disregarded when atoms are separated more than the cutoff distance. This is the result of screening. The Coulombic interactions are effective within quite a short-range in real space, the so-called “near-sightedness principle”[3]. Based on this idea, the linear-scaling of the computational expense for large system[4], can be achieved. The main challenge is to determine the radius for interaction in order to obtain a physically well-motivated basis function.

Typically, the atomic orbitals correspond to a set of functions which decay exponentially with distance from the nuclei. Later, Boys showed that the atomic orbitals could be approximated as linear combinations of Gaussian orbitals[13]. For linear-scaling calculations, Gaussian basis functions lead to huge computational savings because of the ease in the calculation of overlap, and other integrals. The physically motivated shape of atomic orbital may not be the best answer for the basis set since the pseudopotential used modifies the shape of orbital in the nuclear region. Therefore, Pseudo Atomic Orbitals (PAOs) are used for the standard choice of basis set.[18,19] These PAOs can be determined during the generation of pseudopotential as a form for describing the isolated atom. The PAOs decrease rapidly with distance, reaching zero at infinite radius. Locality in real space is imposed to achieve linear-scaling. The tail of

the PAO is modified to reach zero at a given radius by confining the eigenfunctions of the pseudo atomic problems within a spherical boundary at which the potential becomes infinite[20]. The radial confinement is an approximation and can be chosen to achieve an appropriate compromise between high precision and great computational efficiency. While PAOs provide a single basis set, multiple-zeta basis sets needs to be considered for increased variational freedom such as the change in chemical bonding, external fields or other perturbations to electronic structure. The use of multiple-zeta basis sets, multiple Gaussian functions, allow the effective atom size to respond to its environment.

2.3.7 Application to LiNbO₃ Study

For ferroelectric LiNbO₃, the Vienna *Ab Initio* Simulation Package (VASP)[14][15], a plane wave DFT package, is used to the study the properties of domain walls. VASP offers the two most widely used pseudopotentials; ultrasoft-pseudopotentials (USPP)[16] and projector augmented wave (PAW)[17]. For USPP, the norm-conservation is relaxed, and then an augmentation charge density is added. The PAW approach focuses on the augmentation of the wavefunction instead of the density, so all electron properties are captured in the frozen core region. Therefore, PAW methods leads to a better description of the core electrons than USPP in general. PAW requires smaller core-radii and a larger energy cutoff than USPP. A comparison between USPP and PAW method[18] shows that well-constructed USPP and PAW method give almost identical results and are in good agreement with hyper-precise all-electron calculations. However, the PAW method yields more reliable results than the USPP if the system includes the materials having strong electric and magnetic moments. For ferroelectric LiNbO₃ system, the PAW method yield better results. Therefore, PAW basis set is used for investigating the ferroelectricity of LiNbO₃. [19] The projected augmented wave

(PAW)[17] pseudo-potential within the generalized gradient approximation (GGA)[20] is used to evaluate the exchange and correlation interactions. The outmost shells of each ion, $2s^1$ on Li, $4p^6 4d^4 5s^1$ on Nb and $2s^2 2p^4$ on O, are considered as active valence states for the interactions and are treated explicitly; the energy cut-off for the plane waves is 400 eV.[21] A conjugate gradient and quasi-Newton algorithm are used for the ionic relaxation.[22] The force criterion for complete ionic relaxation is $0.0001 \text{ eV}/\text{\AA}$. The residual minimization method direct inversion in the iterative subspace (RMM-DIIS) algorithm[23], which optimizes several individual energy bands at the same time, is used for electronic energy minimization. The pseudopotential and methodologies used here are the same as used previously in studies of intrinsic defects in LiNbO_3 .[24]

2.3.8 Application to Molecular Beam Deposition

For studies involving a gas phase such as molecular beam deposition, plane wave DFT is not computationally efficient enough to carry out the simulation. Instead, linear scaling DFT is a much more powerful method to overcome this limitation. VASP is not suitable because it uses plane wave based pseudopotentials and basis sets. Therefore, we use Spanish Initiative for Electronic Simulations with Thousands of Atoms (SIESTA) software package for this study. Also, B3LYP hybrid method that is based on the mixing of quantum chemical and DFT methods is used for the validation of SIESTA.

When plane wave basis sets are implemented into pseudopotentials for the core region, such as PAW or USPP, the number of calculations can be decreased with the cut-off distance of the pseudopotentials in reciprocal space. However, implementing plane wave basis sets of core electrons into the pseudopotentials of SIESTA do not give much benefit, because SIESTA works with real space localized basis function. Therefore, norm-conserving pseudopotentials are implemented in SIESTA. While the

pseudopotentials in SIESTA reproduce exchange-correlation interactions between nuclei and core electrons by using either LDA or GGA, Gaussian type basis sets are implemented explicitly during the calculation of atomic orbital.

For this study, the nucleus and core electrons of each atom are represented with a Troullier and Martins[25] type norm-conserving pseudopotential through the GGA method. The valence electron Kohn-Sham states are expanded in a linear combination of atomic orbital type basis sets.[26] A double-zeta polarized basis is employed and the valence basis set is localized within a soft confining potential in order to prevent the discontinuities in second derivative of atomic orbital. The basis set parameters for each atom species are optimized to their relative energies and compared to high level quantum mechanical calculations, unrestricted coupled cluster spin contamination corrected with correlation-consistent polarized valence triple zeta basis set (uCCSD(t)/cc-pVTZ).[27-29] The optimized basis set is polarized with an additional *d* orbital on carbon and sulfur and an additional *p* orbital on hydrogen. The soft confinement potential is set to 20 Ry (272 eV) with an inner radius of 0.95 times the outer hard cut-off. A split norm fraction of 0.2 is used in the double-zeta construction of PAO. A mesh cutoff of 150 Ry (2240 eV) is used to determine the fineness of the auxiliary grid basis for the expansion of the density.

2.3.9 Charge analysis Methods

The output of quantum mechanical calculations is the electronic charge density. Atomic charges in molecules or solids are not direct observables in quantum mechanical theory. Because the electronic properties of materials can be fundamentally understood by the charge distribution between components, understanding the variation of charge helps to trace the variation of properties during reaction. There are various

schemes to separate electrons from small portions of the system such as atoms or molecules including Mulliken analysis[30], natural bond orbital analysis[31], Löwdin analysis [32] and Bader analysis[33]. Two different charge analysis schemes are implemented for this study: Mulliken and Bader [34-36] analysis, the two most common schemes in order to partition electrons between atoms or molecules in the system.

Mulliken charge analysis: Mulliken charge analysis is based on the direct population of the orbitals. This scheme can be applied when basis functions of atomic orbital are used in the form of electronic wavefunction of the system. The Mulliken charge on any atom is calculated by the charge associated with the basis functions centered on the particular atom. Even though this method is fast and useful for determining partial charges on atoms, it is sensitive to the choice of basis set. So, Mulliken charge is very dependent on the number of zetas and their cutoffs. Also, the charge assigned to an atom becomes arbitrary for an infinite basis. For plane wave basis functions, which are not associated with any particular atom, Mulliken charge analysis is not applicable. Therefore, Mulliken charge analysis is mainly used in the Gaussian and SIESTA calculation which uses Gaussian type atomic orbital basis set.

Bader charge analysis[33]: The scheme proposed by Bader is based on the electronic charge density instead of the electronic orbitals. For Bader charge, 3D space is divided into subsystems, each of which normally contains one nucleus. Then, the critical points, where the gradient of charge density is zero, are determined by constructing the zero-flux surface. Sets of gradients of electron density are traced in an infinitesimal step until each gradient reaches a maximum at a nucleus. The electron density is integrated within the region between the nucleus and zero flux critical point.

Since this scheme is based on the charge density, it can obtain partial charges and dipole moments of individual atoms in molecules or crystals. Also, Bader analysis is suitable for plane wave basis calculations, because it does not require information on the electronic orbitals. However, Bader analysis has convergence problems in some systems. This scheme is used for determining the charge of plane wave basis set implemented in VASP.

2.3.10 Limitations on DFT

Despite the improvements in DFT, it still has limitations. These limitations arise from two major sources. First, domination of the Coulomb term pushes electrons apart. Second, describing the interaction of degenerate states using the electron density is difficult. These leads to two major limitations on DFT including delocalization error and static correlation error[37].

The delocalization error refers to the tendency of the approximate functional to spread out the electron density. When an electron is delocalized over two centers, DFT predicts a lower energy for overly dispersed fractional charges. This behavior can cause overestimation of the charge distribution during chemical reaction, since the electrons delocalized over more than one center. [38] Thus, DFT predicts highly polarized systems because fractional charges appear at the edges of the molecule. [39] DFT can also predict unphysical charge transfer between the molecule and the metal in molecular electronic device and cause an overestimation of electronic conductance. [40, 41] Thus, the delocalization error explains the underestimation of the band gap for DFT calculation. [37]

The static correlation error, the overestimation of the dissociation energy, arises in situations of degeneracy or near-degeneracy of electron spin states in strongly

correlated systems or in transition metal chemistry. DFT does not accurately describe the interaction between the degenerate spin states and thus gives a large error in describing fractional spin states. The fractional spins cannot be explained by a static correlation function based on constancy of electron correlation. So, this leads to a difficulty in using the electron density to describe degenerate states in transition metals. [37]

As a result, density functional theory is known to be weak at describing intermolecular interactions, especially van der Waals forces (dispersion), charge transfer excitations, transition states, global potential energy surfaces and some other strongly correlated systems such as the band gap in semiconductors. These known problems make DFT unsuitable for the systems which are dominated by dispersion including interaction with noble gas atoms or biomolecules. Although there is still much work to do, diverse corrections[42-44] have been suggested to the functional or the inclusion of additive terms to improve many related predictions.

2.4 Molecular Dynamics (MD) Simulation

2.4.1 Introduction

Electronic-structure calculations generally give the highest available materials fidelity. Unfortunately they are not suitable for the systematic study of system such as domain walls because the computational load for the system sizes required of systems is prohibitively high. Molecular dynamics (MD) is an alternative method for studying molecular behavior. MD simulation is a specialized discipline for predicting the motion of atoms based on statistical mechanics. MD simulation traces the atomic behavior by solving Newton's equation of motion. Newton's second law can be expressed by:

$$\mathbf{F}_i = m_i \mathbf{a}_i \quad (2-18)$$

where, \mathbf{F}_i is the force on an atom i , m_i is mass and \mathbf{a}_i is the acceleration of atom i respectively. The force on atom i can be expressed by the gradient of the interatomic potential energy with respect to position.

$$\mathbf{F}_i = \nabla \cdot V = - \left(i \frac{\partial V}{\partial x_i} + j \frac{\partial V}{\partial y_i} + k \frac{\partial V}{\partial z_i} \right) \quad (2-19)$$

where, V is the potential energy. The potential energy is calculated by different interatomic interactions in the simulation system.

2.4.2 Interatomic Interactions

For ionic systems, the interatomic interactions can be described by two different terms; a long-range and short-range contribution. The details of the interatomic interactions are discussed below.

Long-range interactions: Charged ions interact with another charged ion through Coulombic interactions in a long range. It is described as:

$$V_{ij}^{Coulomb}(r) = \frac{q_i q_j}{4\pi\epsilon_0 r_{ij}} \quad (2-20)$$

where r_{ij} is the distance between the position of two species whose charges are q_i and q_j . Because this equation is proportional to r_{ij}^{-1} , the potential decrease rapidly when the distance between ions increases. Two different ways have been developed to accomplish the convergence of the electrostatic energy and forces within a certain cutoff distance: Ewald summation[45] and direct summation[46]. The Ewald summation method is the traditional approach to solve the electrostatic interaction between ions in an ionic crystal system. However, its complexity and poor compatibility with non charge

neutral system[46] caused limitations for applications. In this study, therefore, the direct summation method of Wolf *et al.* [46] is used for the calculation of the Coulombic interactions.

Ewald sum: The Ewald sum is a method by which the Coulombic interactions at a certain distance, R_c can be truncated without causing a convergence problem. Ewald sum assumes that each point charge is surrounded by a charge distribution of equal magnitude and opposite sign. This imaginary charge is normally considered as Gaussian type distribution. The total sum of these charge can be divided into two different terms: screening interaction between the neighboring charges and charge distribution of the lattice. The screening interaction between charges can be summed in real space, while the long-range charge distribution term is calculated in Fourier space, so call reciprocal space. The real space summation can be easily achieved. However, the summation of long-range charge distribution in reciprocal space is less intuitive and requires an assumption that the system is infinitely periodic. A cut-off distance, R_c is used to improve the simulation efficiency without significant loss of accuracy. Normally, a cut-off of 2 or 3 times the lattice parameter is enough to obtain a good description of long-range interactions. However, the computational load in the Ewald summation method increases as N^2 for N ions. Moreover, the method is not physically transparent.

Direct sum: Although the Ewald summation method is more precise, the computational load is considerable and it causes convergence issue with cut-off distance, R_c . Thus, the direct summation was developed by Wolf *et al.*, and is widely used to calculate the long-range Coulombic interatomic interactions. The convergence issue with charge neutrality is resolved by placing neutralizing charges on the surface of

truncation sphere, see figure 2-2. Thus, any net charge contained in a spherically truncated system is compensated at cutoff distance, R_c .

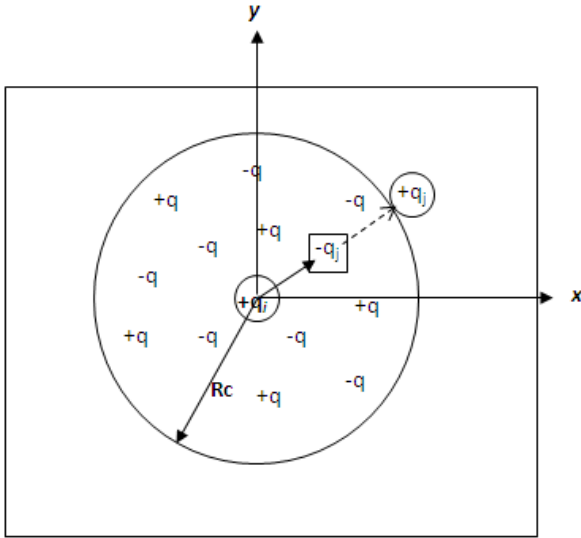


Figure 2-2. 2D Schematic of the charge neutralization scheme used in the direct sum method. For any atom i , interacting with atom j , an equal and opposite charge is placed at the perimeter of the circular cut-off to make the system charge neutral. (Reproduced from reference [46])

The energy for the direct sum can be correctly calculated by subtracting charge-neutralization term from Coulombic sum between interatomic charges under cutoff distance, R_c . The direct sum can be represented as:

$$E_{Coul}(R_c) = \sum_{\substack{j \neq i \\ r_{ij} < R_c}}^N \frac{q_i q_j}{r_{ij}} - \frac{q_i \Delta q_i(R_c)}{R_c} \quad (2-21)$$

where, $\Delta q_i(R_c)$ is the net charge within the cutoff sphere of ion i . The calculated energy oscillates significantly, in a slightly damped manner. Thus, damping the Coulombic potential can be used to quickly damp out the oscillations with increasing R_c .

The direct summation method has successfully predicted the long range Coulombic energy for disordered or non-charge neutral systems such as interfaces or

defects as well as bulk perfect crystal. Therefore, the direct summation method is mainly used to calculate the long range interatomic interactions in this study.

Short-range interactions: The short range interatomic interaction describes the repulsion between ions at a short distance. There are many different models for describing short range interatomic interactions including Buckingham[47], Lennard-Jones[48], Morse[49], Inverse Gaussian[50], Tang-Toennes[51] and Rydberg[52]. In this study, the Buckingham interatomic potential, whose ability to describe ionic crystals is well-established, is used. The functional form for Buckingham potential is:

$$V_{Buck}(r_{ij}) = A_{ij} \exp\left(-r_{ij}/\rho_{ij}\right) - C_{ij}/r_{ij}^6 \quad (2-22)$$

where r_{ij} is the distance between two different ion species, i and j and A_{ij} , ρ_{ij} and C_{ij} are potential parameters. The exponential term represents the increase in repulsive energy with the decrease in the distance between atoms i and j . The second term expresses the Van der Waals attractive contribution due to the dipole interactions.

2.4.3 Shell Model for Describing Polarizability of Electrons

In addition to the interatomic interaction potential, a shell model, which describes each ion as a core consisting of the nucleus and inner electrons and a shell of valence electron, is used for capturing the electronic polarizability of the ions. The core and shell carry partial charges, the sum of which is close to the full ionic charge of each atom species. The positions of the cores and shells are determined in a fully dynamic manner, with fictional masses of 10% of the mass of the individual ions assigned to the shells. The core and shell of each ion interact with the cores and shells of other ions via long range Coulombic interactions. The short-range Buckingham interactions describe the

shell-shell interactions between the ions. The core and shell of each ion are connected by a harmonic spring:

$$V(\omega) = \frac{1}{2}k_2 \omega^2 \quad (2-23)$$

where ω is core-shell displacement and k_2 is the harmonic spring constants.

2.4.4 Three-body Interactions

Another term which is considered for this study is a three-body interaction potential. The three-body potential represents the repulsion between bond pairs. Thus, the harmonic form is normally chosen in order to penalize the deviation from the expected angle for the coordination environment. The functional form for harmonic three-body interaction is described:

$$V_{ijk} = \frac{1}{2}k_2(\theta - \theta_0)^2 \quad (2-24)$$

where k_2 is the three-body harmonic constant and θ is the angle between three ionic species and θ_0 is the expected angle for the coordinate system.

2.4.5 Potential for LiNbO₃ study

The interatomic potential used for LiNbO₃ system was developed by Jackson and coworkers.[53] Three different interatomic interactions, Li-O, Nb-O and O-O are included in the Buckingham potentials. The interatomic interactions are cut off using a shifted force method at a distance of 10.2Å, which corresponds to twice the lattice parameter along [1000]. The core-shell model is used for oxygen ions with the shell charge. Full details are given in Table 2-1.

Table 2-1. The potential parameters for LiNbO₃.

LiNbO ₃				
Interaction	A (eV)	ρ (Å)	C (eV/Å ⁶)	
Li-O	950.0		0.2610	0.00
Nb(Ta)-O	1425.0		0.3650	0.00
O-O	22764.0		0.1490	27.88
LiNbO ₃				
Shell parameter	Shell charge, Y	Spring constant, K ₂ (eV/Å ²)		
O ²⁻	-2.9	70		
LiNbO ₃				
Three-body parameter	Force constant, k _θ (eV/rad)	Equilibrium angle, Θ ₀ (deg)		
O-Nb(Ta)-O	0.5776	90		

2.4.6 Integration Algorithms

The force of an each atom can be obtained from the interatomic potentials using equation (2-19). The velocity and position of atoms at a time t, can be traced by the atomic force. The evolution of the atoms is achieved by integrating the position, velocity and accelerations of the atoms for small increments of time (δt). There are various integration algorithms available including Verlet [54], leap-frog [55], Beeman's[56], and Predictor-Corrector [57] and symplectic integrators [58]. Each method has its advantages and disadvantages with regards to accuracy and computational load depending on the condition of system. In this study, the Verlet algorithm [54] and a 5th-order Gear predictor-corrector method [59] are used.

Verlet algorithm: The verlet algorithm is an integration scheme which offers very good stability and time-reversibility for MD studies. It reduces the level of errors using the position of previous steps instead of velocity. The position at the next time step is predicted by the difference in position at the previous and current time steps. This can be derived from two Taylor expansions of the position vector at two different times.

$$\begin{aligned}
\bar{x}(t + \delta t) &= \bar{x}(t) + \bar{v}(t) \times \delta t + \frac{1}{2} \delta t^2 \bar{a}(t) + \frac{1}{6} \delta t^3 \bar{b}(t) + \frac{1}{24} \delta t^4 \bar{c}(t) + \frac{1}{120} \delta t^5 \bar{d}(t) \\
\bar{x}(t - \delta t) &= \bar{x}(t) - \bar{v}(t) \times \delta t + \frac{1}{2} \delta t^2 \bar{a}(t) - \frac{1}{6} \delta t^3 \bar{b}(t) + \frac{1}{24} \delta t^4 \bar{c}(t) - \frac{1}{120} \delta t^5 \bar{d}(t)
\end{aligned}
\tag{2-25}$$

Where \bar{x} is the position, \bar{v} is the velocity, \bar{a} is the acceleration and \bar{b} , \bar{c} and \bar{d} are third, fourth and fifth derivatives of the position. The higher term of Taylor expansion can be neglected for small time step, adding two Taylor expansions of equation (2-25) gives:

$$\bar{x}(t + \delta t) = 2\bar{x}(t) - \bar{x}(t - \delta t) + \delta t^2 \bar{a}(t) + \delta t^4 \bar{a}(t)
\tag{2-26}$$

Equation (2-26) can be rearranged as:

$$\bar{a}(t) = \frac{\partial^2 \bar{x}(t)}{\partial t^2} = \frac{\bar{x}(t + \delta t) - 2\bar{x}(t) + \bar{x}(t - \delta t)}{\delta t^2}
\tag{2-27}$$

Therefore, the position at next time step is calculated by positions at previous and current step and the acceleration from the interatomic potential. This algorithm is implemented by SIESTA during deposition study.

Predictor-Corrector algorithm: Another algorithm used for this study is the predictor-corrector algorithm. This method uses a Taylor expansion series to predict the positions, velocities, accelerations, and higher order derivatives of position at time $t + \delta t$. Different order of predictor-corrector algorithm can be used. The fifth order Gear predictor-corrector integration method is implemented in our in-house MD code. The method estimates the position of next step in two steps. In first step, the Taylor expansion of positions at time $t + \delta t$ is determined to the fifth order term derivative term. Then, the higher order derivatives of it are also listed in a similar manner, see equation (2-28).

$$\begin{aligned}
\vec{r}^p(t + \delta t) &= \vec{r}(t) + \delta t \vec{v}(t) + \frac{1}{2} \delta t^2 \vec{a}(t) + \frac{1}{6} \delta t^3 \vec{b}(t) + \frac{1}{24} \delta t^4 \vec{c}(t) + \frac{1}{120} \delta t^5 \vec{d}(t) \\
\vec{v}^p(t + \delta t) &= \vec{v}(t) + \delta t \vec{a}(t) + \frac{1}{2} \delta t^2 \vec{b}(t) + \frac{1}{6} \delta t^3 \vec{c}(t) + \frac{1}{24} \delta t^4 \vec{d}(t) \\
\vec{a}^p(t + \delta t) &= \vec{a}(t) + \delta t \vec{b}(t) + \frac{1}{2} \delta t^2 \vec{c}(t) + \frac{1}{6} \delta t^3 \vec{d}(t) \\
\vec{b}^p(t + \delta t) &= \vec{b}(t) + \delta t \vec{c}(t) + \frac{1}{2} \delta t^2 \vec{d}(t) \\
\vec{c}^p(t + \delta t) &= \vec{c}(t) + \delta t \vec{d}(t) \\
\vec{d}^p(t + \delta t) &= \vec{d}(t)
\end{aligned} \tag{2-28}$$

where \vec{r} , \vec{v} , and \vec{a} are the position, velocity and acceleration of each atom at time $t + \delta t$, respectively. \vec{b} , \vec{c} and \vec{d} are third, fourth and fifth derivatives of the position at the incremented time. The superscript 'p' represents that they are the 'predicted' values.

The position, velocity, acceleration and higher order derivatives at time $t + \delta t$ can be predicted using interatomic potentials. In the second step, the predicted acceleration values are corrected. The correct accelerations are calculated by the forces on the atoms. Using this force, the correct accelerations ($\vec{a}^c(t + \delta t)$) can be obtained.

Therefore, the error between the predicted acceleration $\vec{a}^p(t + \delta t)$ and the correct acceleration $\vec{a}^c(t + \delta t)$ can be given as:

$$\Delta \vec{a}(t + \delta t) = \vec{a}^c(t + \delta t) - \vec{a}^p(t + \delta t) \tag{2-29}$$

The predicted position, velocity and acceleration can be corrected using the error.

$$\begin{aligned}
\vec{r}^c(t + \delta t) &= \vec{r}^p(t + \delta t) + c_0 \Delta \vec{a}(t + \delta t) \\
\vec{v}^c(t + \delta t) &= \vec{v}^p(t + \delta t) + c_1 \Delta \vec{a}(t + \delta t) \\
\vec{a}^c(t + \delta t) &= \vec{a}^p(t + \delta t) + c_2 \Delta \vec{a}(t + \delta t) \\
\vec{b}^c(t + \delta t) &= \vec{b}^p(t + \delta t) + c_3 \Delta \vec{a}(t + \delta t) \\
\vec{c}^c(t + \delta t) &= \vec{c}^p(t + \delta t) + c_4 \Delta \vec{a}(t + \delta t) \\
\vec{d}^c(t + \delta t) &= \vec{d}^p(t + \delta t) + c_5 \Delta \vec{a}(t + \delta t)
\end{aligned} \tag{2-30}$$

where, c_0 , c_1 , c_2 , c_3 , c_4 and c_5 are empirically determined numerical constants, respectively. The values for a fifth order predictor-corrector are $c_0 = 3/16$, $c_1 = 251/360$, $c_2 = 1$, $c_3 = 11/18$, $c_4 = 1/6$, and $c_5 = 1/60$ [57, 59]. These corrected values are used to predict the positions and other higher order derivatives at the next step.

The time step (δt) is one of the most crucial factor for sampling the simulation trajectory. The average phonon period for a typical atomic vibration is about 200 fs. A typical time step for capturing correct atomic vibration is 1 fs. For this study, however, the time step 0.05 fs is used to capture internal vibrations of ions between core and shell.

2.4.7 Geometry Optimization

Figure 2-3 shows the potential energy surface of an arbitrary system. For the potential energy surface, point A represents the global minima and point B represents a local maxima or transition state and point C represent the local minima. The task for geometry optimization is to find the global minima for the given structure. Although the optimized geometry is desired, the structure can be easily trapped by local minima of potential energy. There are various methods[60] available to find the local minimum including the bisection, golden search, steepest descent, conjugate gradient and Newton-Raphson method. In this study, steepest descent, conjugate gradient and Newton-Raphson method are mainly used to find out optimized geometry structure.

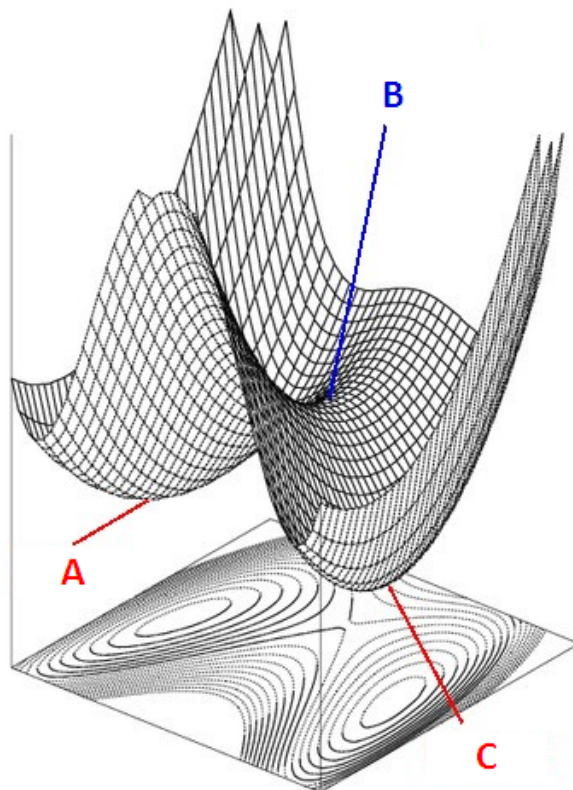


Figure 2-3. Illustration of potential energy surface of a arbitrary function. Picture taken with permission from http://www.chm.bris.ac.uk/pt/harvey/msci_pract/pics/pot_surface.jpeg

The steepest descent is a first-order method which uses the first derivative of a function. The first derivative goes to zero at either a minima or maxima. Figure 2-4 shows a schematic view of steepest descent optimization method. the optimization scheme moves to a minimum along the negative gradient in the steepest direction. If the energy of system increases, line search among the last three steps will be performed to determine where to go for the next step. Steepest descent has the advantage of relaxing a poor initial geometry quickly and is very useful for preliminary optimization. However, it is very slow to achieve optimization because it can oscillate around the minimum energy path.

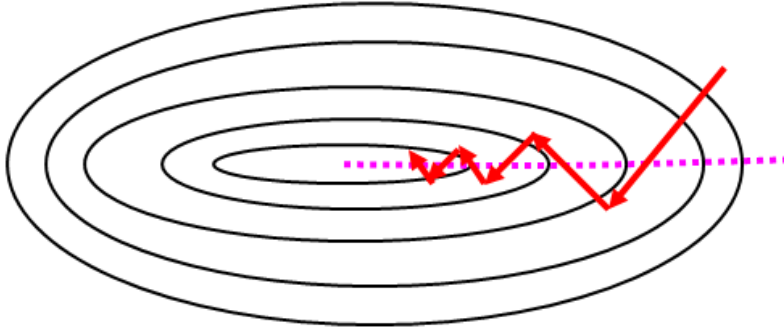


Figure 2-4. Schematic of steepest descent method.

Further improvement to steepest descents resulted in the conjugate-gradient method. The conjugate-gradient method follows a modified direction, determined by gradients at the current and previous searching directions instead of following the current gradient direction. The conjugate gradient method shows much better convergence than the steepest descent method. However, it has a higher computational load for each step because it needs to store the trajectory of previous step and also use the second derivatives. The conjugate gradient method can be expressed as:

$$d_i = -g_i + \beta_i d_{i-1} \quad (2-31)$$

where β_i is determined by gradients at the current and last few points and d_i is the search direction at step i .

The Newton-Raphson method is a second-order method in which a function at a given point is expressed as Taylor expansion. The displacement directions for the next step follow the eigenvectors of the current Hessian. The step size is determined by the eigenvector. The functional form can be express as:

$$(x - x_0) = -g / H = -H^{-1} g \quad (2-32)$$

and

$$\Delta x_i' = f_i / \varepsilon_i \quad (2-33)$$

where H is the Hessian, f_i is the projection of gradient along the i -th eigenvector whose eigenvalue is ε_i . This method converges very efficiently when the initial point is close to a minimum point. A trust radius and a shift parameter λ can be set to control step size. These will prevent the system from moving out of the potential energy surface by taking too large step size. The Hessian is computationally very expensive. So, approximated Hessians, updated by energy and gradient can be also used. However, this method is not practical for optimizing large simulation system. Also, it can be easily trapped by local minima if the initial point is far away from the global minimum. Due to the different properties of each method, a combination of different optimization methods is implemented in this study.

2.4.8 Thermodynamic Conditions (Ensembles)

The ensemble describes the specific thermodynamic conditions which can replicate the environmental condition. The environmental condition of the system can be described by three different thermodynamic state variables: pressure (P), volume (V) and temperature (T). The most common experimental condition is constant pressure and temperature. For simulation systems with fixed number of atoms, the experimental condition can be normally reproduced by the isothermal-isobaric (NPT) ensemble, in which P and T are fixed. Other ensembles are also available for simulation study depending on the thermodynamic conditions. When the system is under constant volume instead, the system is in the canonical (NVT) ensemble. Similarly, for constant pressure and enthalpy, the condition for the system is isobaric-isoenthalpic (NPH) ensemble. In this study, the most of MD simulations are performed under NPT ensemble because it corresponds to the most experimental condition. There are various

algorithms to maintain the constant pressure and temperature. In this study, the constant pressure of the system is obtained by Parrinello and Rahman method [61, 62]. This method originates from an extended Lagrangian method [63] which considers a set of pistons attached to the system. The variation of the force on the pistons is compensated by the variation of simulation volume to maintain a constant pressure. This method was extended by Parrinello and Rahman in order to allow it to change the shape and size of simulation cell. A thermostat is used to obtain the constant temperature of the system. There are also different thermostats including velocity rescaling [59], Nosé-Hoover [64, 65] Berendsen [66] and generalized Langevin [67, 68]. Velocity rescaling is the most intuitive and simplest form of thermostat. The velocities of the atoms are rescaled to match the desired temperature. This can be given by:

$$v_s = v_i \times \sqrt{\frac{T_d}{T_i}} \quad (2-34)$$

where v_s is the rescaled velocity, v_i is the initial velocity, T_d is target temperature and T_i is the initial temperature. In this study, the velocity rescaling method is used in the MD studies.

CHAPTER 3 STRUCTURAL ANALYSIS

In this chapter, the crystal structures of the materials under investigation are introduced. In this thesis, the primary focus is on elucidating interfacial phenomenon of the trigonal ferroelectrics, LiNbO₃ and LiTaO₃ and the conductive polymer, polythiophene. For better understanding of interfaces, the crystallography of trigonal ferroelectrics and polythiophene are introduced in details.

3.1 Trigonal Ferroelectrics

3.1.1 Introduction on LiNbO₃

LiNbO₃ has a high spontaneous polarization, 70 μC/cm², and high Curie temperature, ~1480 K[69, 70]. Recent successes using the vapor-transport equilibration (VTE) method[71] have enabled the growth of stoichiometric LiNbO₃; however, congruent LiNbO₃ is Li deficient[72, 73]. Although various defect models including pseudo-Schottky defects, Schottky defects, and Frenkel defects have been suggested[74], only a Nb antisite, compensated by four Li ion vacancies ($Nb_{Li}^{''''} + 4V_{Li}'$ or Antisite_I) [74-76] and five Nb antisites compensated by four Nb vacancies ($5Nb_{Li}^{''''} + 4V_{Nb}^{''''}$ or Antisite_{II})[76] were able to successfully explain the stoichiometry of congruent LiNbO₃. Atomistic modeling by Donnerberg *et al.*[77] showed that the compensation by Nb vacancies is energetically less favorable than the compensation by Li vacancies. Recent DFT calculations[24] showed that Antisite_I cluster and Li Frenkel pair are the most energetically favorable defect pairs in LiNbO₃ under Li deficient (congruent) and Li rich (stoichiometric) conditions respectively. An analysis of Antisite_I clusters determined that several arrangements of Li vacancies around a Nb antisite are nearly energetically equivalent.[78] The ability of calculations with empirical potentials to describe point

defect properties was demonstrated by Araujo and co-workers[79]. Moreover, two different types of domain walls, parallel and perpendicular to the c-glide plane in LiNbO_3 were suggested by Gopalan *et al.*[80] The structure and energetics of them are characterized here[19].

Before it is possible to understand the domain wall structure, it is necessary to understand the crystallography of trigonal ferroelectrics in some detail. In this section, LiNbO_3 is only considered. The structure of LiTaO_3 is identical.

3.1.2 Crystallography of LiNbO_3

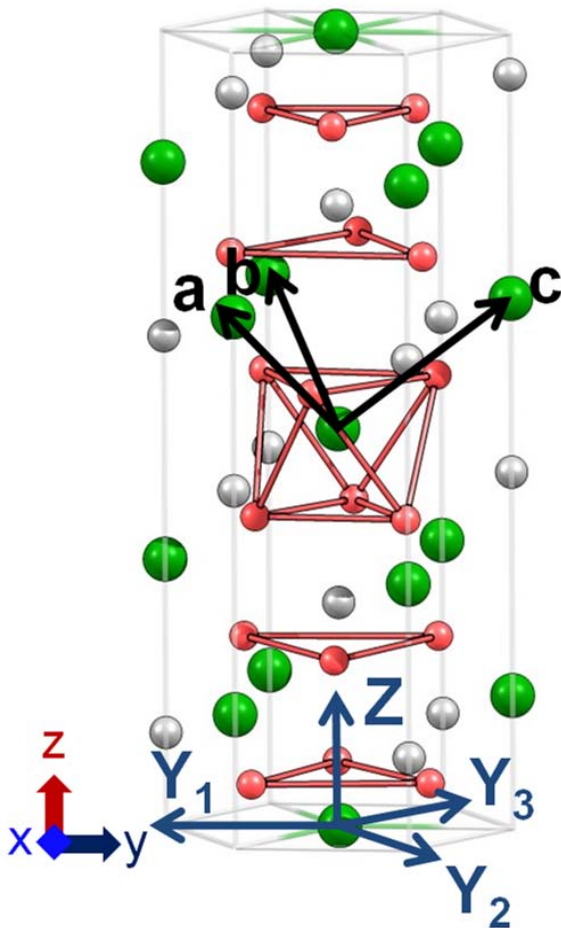


Figure 3-1. Crystallographic direction of rhombohedral axes (middle) and hexagonal axes (bottom) in a unit-cell of LiNbO_3 . The Cartesian axes are given at the bottom left of the figure.

To understand the crystallography and properties of LiNbO_3 , it is necessary to use three distinct coordinate systems: rhombohedral, hexagonal, and Cartesian coordinates, see figure 3-1. The Cartesian coordinates are denoted as x, y, z ; the rhombohedral coordinates are denoted as a, b, c ; the hexagonal coordinates are denoted as Y_1, Y_2, Y_3, Z . The rhombohedral coordinates can be represented as $a = \sqrt{3}/2x - 1/2y + 1/3z$, $b = -\sqrt{3}/2x - 1/2y + 1/3z$ and $c = y + 1/3z$. The hexagonal coordinates can be represented as $Y_1 = -y, Y_2 = \sqrt{3}/2x + 1/2y, Y_3 = -\sqrt{3}/2x + 1/2, Z = z$.

In the paraelectric $R3c$ (#167) state, the Li and Nb ions occupy 6a and 6b Wyckoff positions respectively, while the oxygen ions occupy 18e Wyckoff positions, see Table 3-1. While the 6a and 6b site positions are fully defined by the crystallographic tables[81], the positions of the 18e oxygen sites are in addition characterized by a positional parameter X_O , which defines the displacements of each oxygen ion along its associated hexagonal axis, the precise value of X_O being different in different $R3c$ systems. Neutron powder diffraction studies have determined the positional parameter for LiNbO_3 to be $X_O=0.0591-0.0607$ [82]. Previous DFT studies yielded $X_O=0.036$ [83] and 0.049 [84] in the local density approximation (LDA) calculations with Perdew-Wang 91 (PW91) and Perdew-Burke-Ernzerhof 96 (PBE) basis sets and $X_O=0.048$ [85] in a generalized gradient approximation (GGA) calculation with PBE basis set. Our DFT study using the GGA pseudopotential with projector augmented-wave (PAW) basis sets gives $X_O=0.039$ which lies within the same range. In agreement with a previous atomic-level simulation with different interatomic potential study[53], our simulations with empirical potentials yield $X_O=0.034$, which is somewhat smaller than the experimental values, but very similar to the DFT values.

Table 3-1. Wyckoff positions for R3c (space group 167) state [86]

Multiplicity	Hexagonal axes Coordinates		
18e (Oxygen)	x_0	0	$\frac{1}{4}$
	0	x_0	$\frac{1}{4}$
	$-x_0$	$-x_0$	$\frac{1}{4}$
	0	$-x_0$	$\frac{1}{2} + \frac{1}{4}$
	$-x_0$	0	$\frac{1}{2} + \frac{1}{4}$
	x_0	x_0	$\frac{1}{2} + \frac{1}{4}$
	$\frac{2}{3} + x_0$	$\frac{1}{3}$	$\frac{1}{3} + \frac{1}{4}$
	$\frac{2}{3} - 0$	$\frac{1}{3} + x_0$	$\frac{1}{3} + \frac{1}{4}$
	$\frac{2}{3} - x_0$	$\frac{1}{3} - x_0$	$\frac{1}{3} + \frac{1}{4}$
	$\frac{2}{3} - 0$	$\frac{1}{3} - x_0$	$\frac{5}{6} + \frac{1}{4}$
	$\frac{2}{3} - x_0$	$\frac{1}{3}$	$\frac{5}{6} + \frac{1}{4}$
	$\frac{2}{3} + x_0$	$\frac{1}{3} + x_0$	$\frac{5}{6} + \frac{1}{4}$
	$\frac{1}{3} + x_0$	$\frac{2}{3}$	$\frac{2}{3} + \frac{1}{4}$
	$\frac{1}{3} - 0$	$\frac{2}{3} + x_0$	$\frac{2}{3} + \frac{1}{4}$
	$\frac{1}{3} - x_0$	$\frac{2}{3} - x_0$	$\frac{2}{3} + \frac{1}{4}$
	$\frac{1}{3} - 0$	$\frac{2}{3} - x_0$	$\frac{1}{6} + \frac{1}{4}$
$\frac{1}{3} - x_0$	$\frac{2}{3}$	$\frac{1}{6} + \frac{1}{4}$	
$\frac{1}{3} + x_0$	$\frac{2}{3} + x_0$	$\frac{1}{6} + \frac{1}{4}$	
6b (Nb,Ta)	0	0	0
	0	0	$\frac{1}{2}$
	$\frac{2}{3}$	$\frac{1}{3}$	$\frac{1}{3}$
	$\frac{2}{3}$	$\frac{1}{3}$	$\frac{5}{6}$
	$\frac{1}{3}$	$\frac{2}{3}$	$\frac{2}{3}$
6a (Li)	$\frac{1}{3}$	$\frac{2}{3}$	$\frac{1}{6}$
	0	0	$0 + \frac{1}{4}$
	0	0	$\frac{1}{2} + \frac{1}{4}$
	$\frac{2}{3}$	$\frac{1}{3}$	$\frac{1}{3} + \frac{1}{4}$
	$\frac{2}{3}$	$\frac{1}{3}$	$\frac{5}{6} + \frac{1}{4}$
	$\frac{1}{3}$	$\frac{2}{3} + \frac{1}{4}$	
	$\frac{1}{3}$	$\frac{1}{6} + \frac{1}{4}$	

The crystallography of the ferroelectric phase is more complicated. On losing inversion symmetry along the Z-direction during the phase transition to the ferroelectric state, the space group drops to *R3c* (#161). The “up” polarization is obtained when the Nb atoms shift up from the octahedra centers and the Li atoms sits above their oxygen

planes, see figure 3-2. Correspondingly, “down” polarization is obtained when the Nb atoms are shifted down and the Li atoms sit below the oxygen planes.

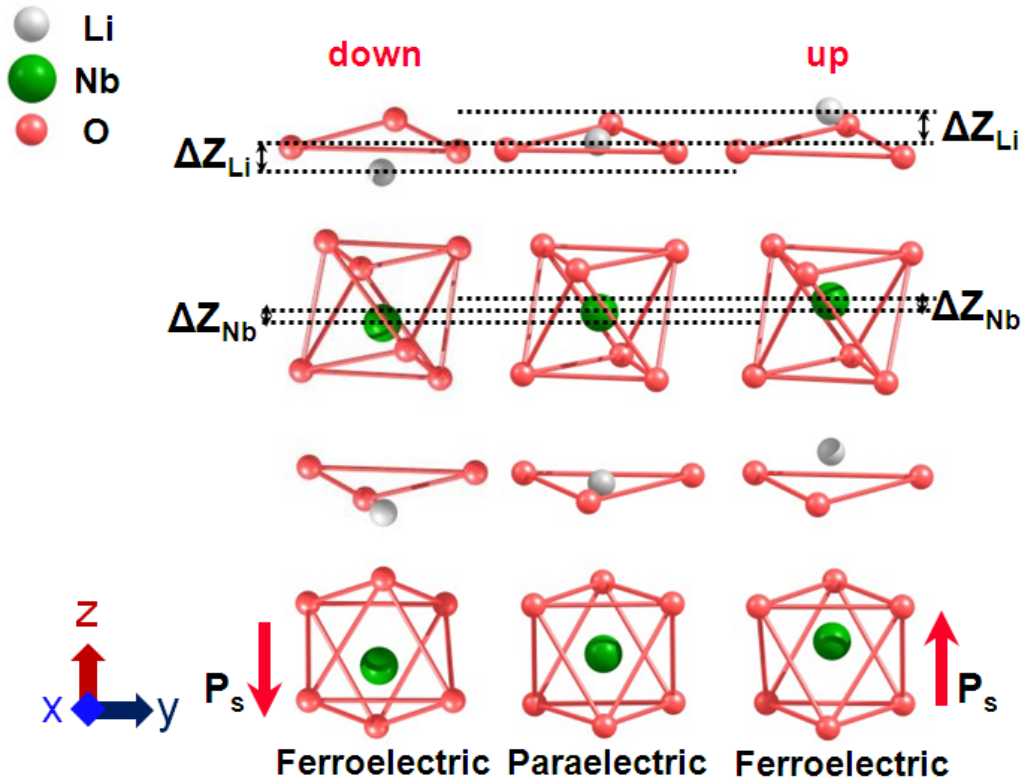


Figure 3-2. Schematic of the paraelectric (center) and ferroelectric phase with up polarization (right) and down polarization (left). The ferroelectric distortions associated with the displacement of the Nb ions (green) from the center of the octahedral cages of oxygen ions (red) is ΔZ_{Nb} . The displacement of Li ions (gray) from the associated planes of oxygen ions is ΔZ_{Li} .

In this structure, the Li and Nb ions both sit at 6a Wyckoff positions; the oxygen ions occupy the 18b positions, see Table 3-2. Positional difference between cations comes from the Z_{Li} and $Z_{Nb(Ta)}$ which determine the position in Z-direction. For LiNbO₃ and LiTaO₃ systems, $Z_{Nb(Ta)}$ is defined as 0 for simplicity of analysis. X-ray diffraction studies[87] yield a positional parameter for Li of $Z_{Li}=0.283$ for up polarization state and $Z_{Li}=0.217$ for down polarization states, which correspond to displacements of $Z=\pm 0.033$ from the positions in the paraelectric phase; the DFT and empirical simulations yield

almost identical values. In characterizing the oxygen displacements, it is important to distinguish between the Cartesian coordinates and the hexagonal coordinates, the latter being more useful for understanding the in-plane displacements. In hexagonal coordinates, the crystallographic positions of the oxygen ions in the ferroelectric state are characterized as $(u, 1/3+v, 1/12-w)$ for up polarization state and $(u-v, 1/3-v, 1/12+w)$ for down polarization[88]. An X-ray study[87, 89] determined $(u, v, w) = (0.0492, 0.0113, 0.0186)$, see Table 3-3. Values obtained from a more detailed crystallographic analysis[82], from DFT[85], and from simulations with the same empirical potential as we are using[53] yielded similar magnitudes. Our DFT and empirical calculations yield results consistent with the published values. The difference in oxygen position between up and down polarization is $(\Delta v, 2\Delta v, 2\Delta w)$. Because the X- and Y-directions are at 120° to each other, the two polarization states actually have the same Cartesian x-coordinate, but different y-coordinate. Because of the three-fold rotation symmetry, the oxygen ions move along three equivalent Y-directions, one of which is aligned to be parallel to the Cartesian y-axis.

Because it is easier to understand the structure in the rhombohedral unit cell, figure 3-3 shows the structure along the rhombohedral [001] direction (corresponding to the $[42\bar{6}1]$ direction in the hexagonal coordinate system). In this direction, and in the [100] and [010] directions, the alternating oxygen octahedra tilt in opposite directions with tilting angle ω . This in-plane displacement tilting can be expressed as $a^-a^-a^-$ with $\omega=24.1^\circ$, using Glazer's notation for perovskite systems.[90]

Table 3-2. Wyckoff positions for R3c (space group 161) state [86]

Multiplicity	Hexagonal axes Coordinates		
18b (Oxygen)	x_0	y_0	z_0
	$-y_0$	$x_0 - y_0$	z_0
	$y_0 - x_0$	$-x_0$	z_0
	$-y_0$	$-x_0$	$1/2 + z_0$
	$y_0 - x_0$	y_0	$1/2 + z_0$
	x_0	$x_0 - y_0$	$1/2 + z_0$
	$2/3 + x_0$	$1/3 + y_0$	$1/3 + z_0$
	$2/3 - y_0$	$1/3 + x_0 - y_0$	$1/3 + z_0$
	$y_0 + 2/3 - x_0$	$1/3 - x_0$	$1/3 + z_0$
	$2/3 - y_0$	$1/3 - x_0$	$5/6 + z_0$
	$y_0 + 2/3 - x_0$	$1/3 + y_0$	$5/6 + z_0$
	$2/3 + x_0$	$1/3 + x_0 - y_0$	$5/6 + z_0$
	$1/3 + x_0$	$2/3 + y_0$	$2/3 + z_0$
	$1/3 - y_0$	$2/3 + x_0 - y_0$	$2/3 + z_0$
	$y_0 + 1/3 - x_0$	$2/3 - x_0$	$2/3 + z_0$
$1/3 - y_0$	$2/3 - x_0$	$1/6 + z_0$	
$y_0 + 1/3 - x_0$	$2/3 + y_0$	$1/6 + z_0$	
$1/3 + x_0$	$2/3 + x_0 - y_0$	$1/6 + z_0$	
6a (Nb,Ta)	0	0	$0 + z_{Nb(Ta)}$
	0	0	$1/2 + z_{Nb(Ta)}$
	$2/3$	$1/3$	$1/3 + z_{Nb(Ta)}$
	$2/3$	$1/3$	$5/6 + z_{Nb(Ta)}$
	$1/3$	$2/3$	$2/3 + z_{Nb(Ta)}$
	$1/3$	$2/3$	$1/6 + z_{Nb(Ta)}$
6a (Li)	0	0	$0 + z_{Li}$
	0	0	$1/2 + z_{Li}$
	$2/3$	$1/3$	$1/3 + z_{Li}$
	$2/3$	$1/3$	$5/6 + z_{Li}$
	$1/3$	$2/3$	$2/3 + z_{Li}$
	$1/3$	$2/3$	$1/6 + z_{Li}$

As a result of this tilting in three spatial directions, there are six distinct oxygen layers along the z-direction[91]. For the “up” polarization state, the three bottom oxygen layers rotate counter-clockwise about the z-axis while the three top oxygen layers rotate clockwise, see figure 3-4(a); this six-oxygen layer pattern repeats. The rotation angle

between the first and second oxygen layers is slightly different from the angle between the second and third oxygen layers. The first oxygen layer is rotated by 7.7° in the clockwise direction along z-direction from the non-displaced center position. Then, the second oxygen layer is rotated 63.6° from first oxygen layer and third oxygen layer shows slightly larger rotation angle, 67.8° from the second bottom layer in the counter-clockwise direction. The three upper oxygen layers rotate in the opposite direction. The first oxygen layer shows rotation angle, 7.7° in the counter-clockwise direction from non-distorted lattice. Then, the second and third oxygen planes are each rotated by 63.6° and 67.8° in the clockwise direction. In the bulk, these anti-phase rotations cancel in both the x- and y-directions, leading to a net zero in-plane polarization. The “down” polarization shows corresponding displacements. Although the rotation angles between each layer are different from those in the “up” polarization state, the cancelation of the clockwise rotation of the upper three oxygen layers and the counter-clockwise rotation of the bottom three oxygen layers again leads to net zero in-plane polarization.

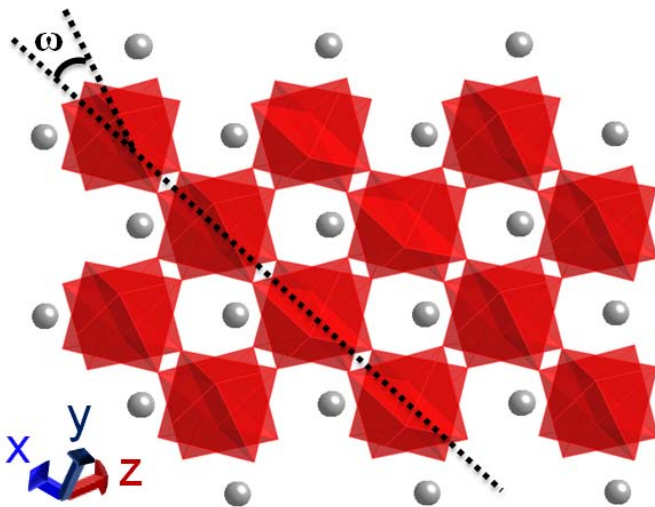


Figure 3-3. [001] projection of the rhombohedral structure. Alternating oxygen octahedra tilt in opposite directions with angle $\omega=24.1^\circ$.

Table 3-3. Comparison of positional parameters of LiNbO₃ between empirical calculations, DFT calculations and experimental data. For the empirical study, the two different values correspond to 0 K (upper) and at 293 K (lower; in the parenthesis). The 293 K values represent the average values from molecular dynamics simulation. It is not able to stabilize the paraelectric phase at 293K using molecular dynamics simulation.

	Lattice parameter		$X_{O,para}$	$Z_{Li,ferro}$	u	V	w
	$a(\text{\AA})$	$c(\text{\AA})$					
Experiment [82, 87, 89]	5.148	13.863	0.0591~0.0607	0.283	0.0492	0.0113	0.0186
LDA(PW)[85]	5.067	13.721	0.036~0.049	0.285	0.0427	0.0125	0.0183
GGA(PBE)[85]	5.200	13.873	0.048	0.282	0.0479	0.0097	0.0199
GGA(PAW) (present)	5.132	13.884	0.039	0.282	0.0388	0.0128	0.0207
Empirical[53]	5.156 (5.187)	13.683 (13.710)	0.034 (0.053)	0.352 (0.288)	0.0525 (0.0563)	0.0310 (0.0294)	-0.0495 (0.0133)
Empirical (present)	5.169 (5.185)	13.685 (13.738)	0.034	0.283 (0.281)	0.0527 (0.0504)	0.0308 (0.0313)	0.0208 (0.0207)

Because the in-plane positions of the oxygen ions differ in the up and down directions, when the polarization is flipped from up to down, the positions of the oxygen ions change along one of the three equivalent hexagonal directions. Thus, the three different sets of 6 oxygen ions can be denoted as O1, O2 and O3 and their corresponding hexagonal axes as Y_1 , Y_2 and Y_3 . The arrows in Figs. 3-4(b) and (c) represent the directions of the displacements of the three types of oxygen ions when the system switches from up to down polarization. The domain walls, parallel to the crystallographic c-glide planes (yz plane) are termed as Y-walls. Similarly, the domain walls, parallel to the crystallographic xz planes and perpendicular to c-glide plane are termed X-walls. As we shall see, this complex crystallography of the single crystal has a profound effect on the structure and properties of the domain walls.

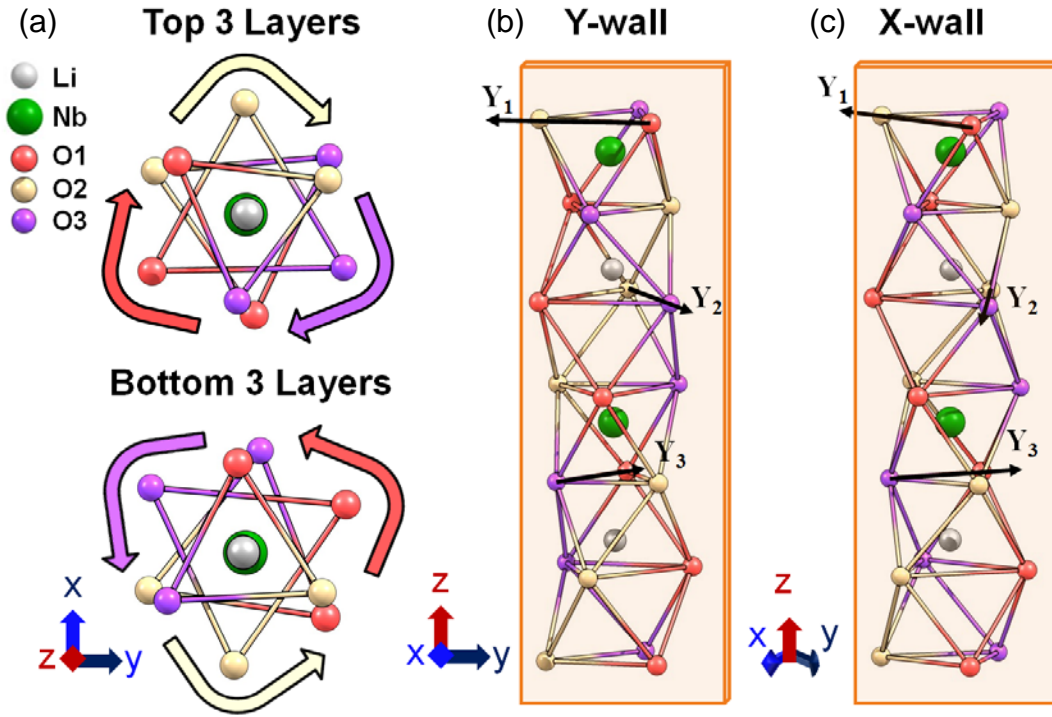


Figure 3-4. Schematic of (a) Y1, Y2 and Y3 axis along with three oxygen ions, O1, O2 and O3. (b) Crystallographic direction of Y1, Y2 and Y3 axes parallel to the Y-wall in the y-z plane. (c) Crystallographic direction of Y1, Y2 and Y3 axes parallel to X-wall i.e., parallel to an x-z plane and at a 30° angle to a y-z plane. The top oxygen layer of (b) and (c) is a duplicate of the bottom oxygen layer.

3.1.3 Temperature Effects on LiNbO_3

For empirical calculations, the ferroelectric polarization of LiNbO_3 can be understood in terms of the electronic polarizations associated with the core-shell interactions, the displacements of Li and Nb ions from the high symmetry positions of the paraelectric phase, and the associated small oxygen displacements. Figure 3-5(a) shows the temperature dependence of the polarization as determined with the Jackson potential. The polarization decreases quite gradually up to 1400K, above which it rapidly drops to zero at 1500-1510K, which we take as an estimate of the Curie temperature for this potential. This value is in good agreement with the experimental Curie temperature

of 1483K.[92] This result is also supported by an analysis of the distribution profile of the displacements of the Nb and Li atoms from the centers of the oxygen octahedra and from the oxygen planes. Well below the Curie temperature, the main effect of the increased temperature is a broadening of the distribution of cation positions about their displaced values with only a small decrease in polarization. At temperatures above 1400K, there is a significant shift of the cations to positions that are symmetric relative to the oxygen sublattice, with an associated significantly decreased polarization.

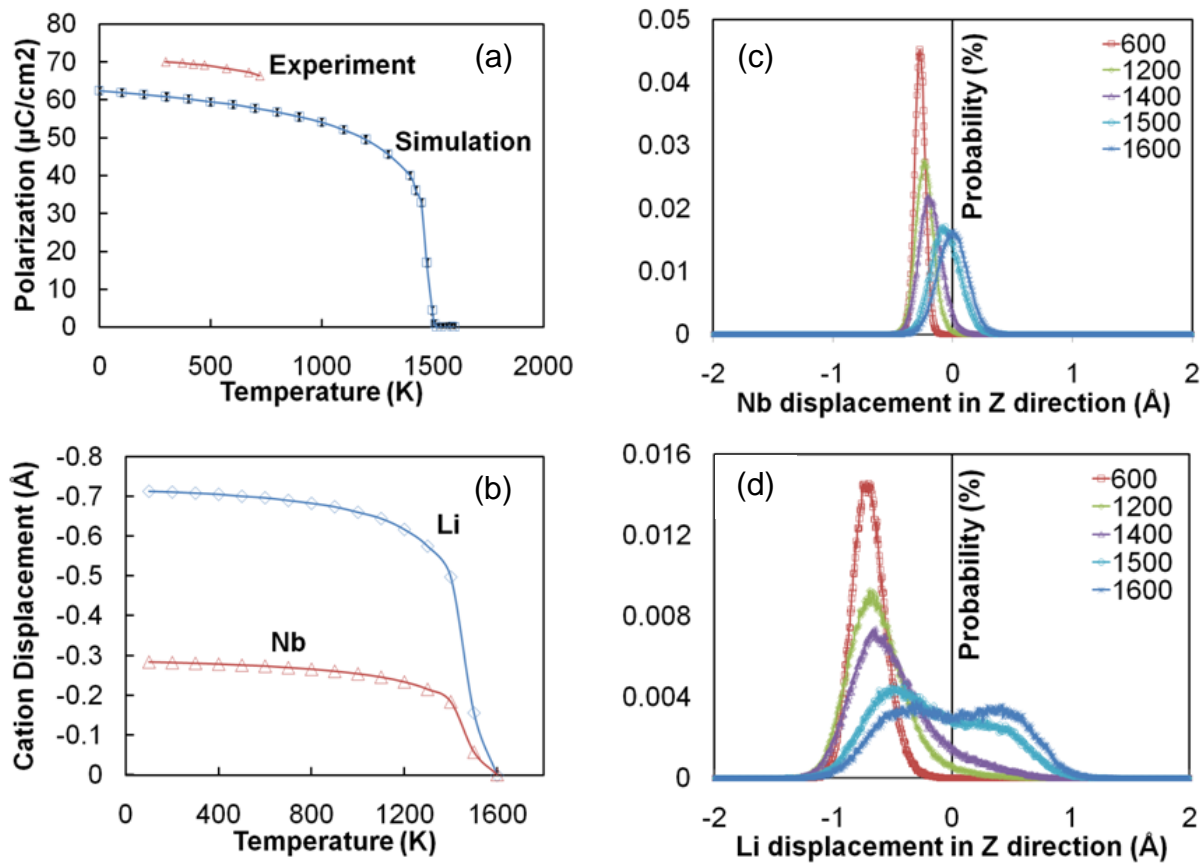


Figure 3-5. (Color online) (a) Temperature dependence of polarization of LiNbO₃ from experiment and MD calculation; (b) Temperature dependence of averaged displacement of Li and Nb ions from an oxygen plane and the center of the oxygen cage; Probability distribution profiles for (c) $\Delta Z_{\text{Nb-O}}$ and (d) $\Delta Z_{\text{Li-O}}$ for various temperatures.

Figure 3-5(b) shows the average displacements of the Li and Nb ions from their crystallographically expected sites, both of which decrease to zero at the Curie temperature. We see that the Nb displays displacive dynamics, figure 3-5(c), while the Li ions show order-disorder behavior, figure 3-5(d), consistent with the results previously obtained with the Tomlinson potential[77]. These results differ from the previous results using the Tomlinson potential[93], which showed that the Nb displacements went to zero well below the Curie temperature; this effect is not seen for this potential.

3.1.4 Domain Walls in LiNbO₃

Ferroelectric materials belong to a class of crystals whose low symmetry supports a spontaneous polarization along one or more crystal axes in the absence of an electric field[94]. This spontaneous polarization consequently appears as an apparent surface charge density with depolarizing field (E_D). The ferroelectric phase will try to minimize its energy associated with the polarization by twinning. This causes the crystal to divide into many oppositely polarized regions called domains. The type of domains formed in the crystal depends on the crystal structure. For LiNbO₃, the longitudinal polarizations, come from two degree of freedom (up and down), make only 180° domains possible. Figure 3-6 shows a schematic representation of the formation of 180° domains. Alternate areas with opposite charges are generated on the surface to minimize E_D , resulting in an overall zero polarization in the crystal. The domain walls will affect the structure and properties of ferroelectric materials.

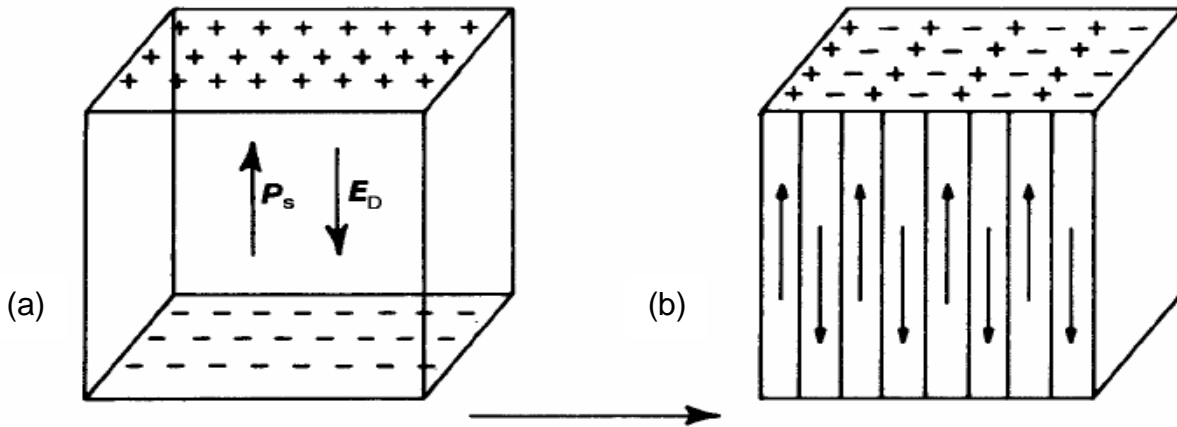


Figure 3-6. Schematic of (a) surface charge associated with spontaneous polarization, (b) formation of 180° domains to minimize electrostatic energy [95]

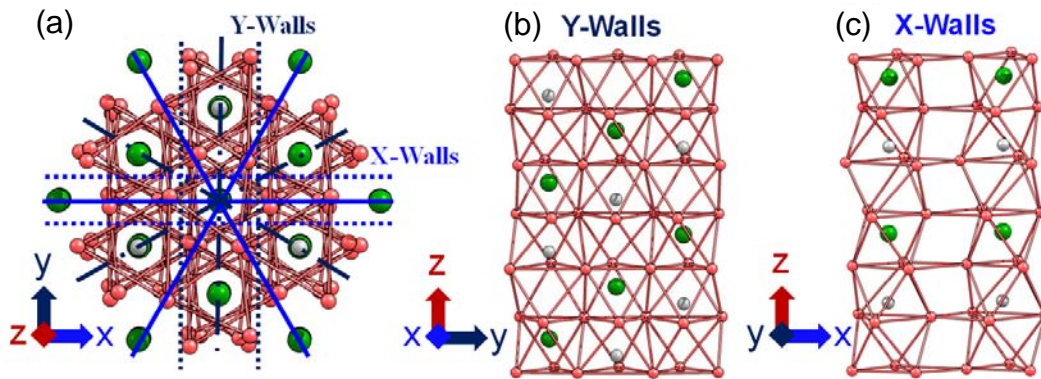


Figure 3-7. (a) Schematic view parallel to the (0001) plane showing two structurally distinct domain wall structures; (b) planar structure of Y-wall on $(11\bar{2}0)$ plane; (c) planar structure of X-wall on $(10\bar{1}0)$ plane.

The domain walls in LiNbO₃ separate regions with polarizations in the $+z$ [0001] and $-z$ [000 $\bar{1}$] directions. Scrymgeour *et al.* [96] determined that two different crystallographic planes can define the domain wall. In figure 3-7(a) the X-walls and Y-wall are projected onto the (0001) plane. The Y-wall lies parallel to c-glide planes, thus containing only cations or anions, but not both. The X-wall lies perpendicular to c-glide planes, and thus contains both cation and anions. Figures 3-7(b) and 3-7(c) show slices

through these domain walls on one side of the wall, parallel to (0110) for the Y-wall and parallel to (1010) for the X-wall.

The two structurally distinct domain wall planes lead to two variants of domain walls. Every Y-wall lies parallel to one of the Y-axes; every X-wall lies parallel to one of the X-axes, symmetrically between two of the Y-axes. For the Y-wall parallel to the Y_1 axis, see figure 3-4(b), we can expect the O1 oxygen ions to be displaced parallel to the wall (i.e., along the Y_1 axis), and the O2 and O3 ions to be displaced along the Y_2 and Y_3 axes at $\mp 120^\circ$ to the domain wall.

Because, the X-walls lie along planes at 30° to the Y-walls, they lie perpendicular to one of the Y-axes (figure 3-4(c)). For the X-wall plane perpendicular to Y_2 axis, as shown in figure 3-4(c), the O2 ions mainly displace parallel to the Y_2 axis, i.e., perpendicular to the domain wall. By contrast the O1 and O3 displace mainly at $\pm 30^\circ$ from the X-wall.

As we will see in Chapter 4, because of their different crystallographies, the two domain walls show different atomic structures and different patterns of polarization in the domain wall region, and thus have different domain wall energies.

3.2 Conductive Polymers

3.2.1 Introduction

All carbon based polymers were generally accepted as insulators for a long time. Plastics, which are a particular type of polymers, were mainly utilized as insulating materials, such as inactive packaging. After electronic conductivity in polymers were discovered about 30 years ago [97], polymers have been incorporated into displays and batteries. However, low stability, poor processibility and high manufacturing costs limits their applications to small scale applications. They are extensively studied for their

potential application to additional electronics devices such as organic solar cells, printing electronic circuits, organic light-emitting diode, actuator, electrochromism, supercapacitors, biosensors, flexible transparent displays, electromagnetic shielding and transparent conductors[98-101]. The new class of polymer known as intrinsically conductive polymer, or electroactive polymers, changes the narrow perspective on polymers. As a new technology, the potential uses of conductive polymers for industry are quite significant.

There are many known conductive polymers including polyacetylene, polyphenylene, polyphenylene sulfide (PPS), p-phenylenevinylene (PPV), polypyrrole, polythiophene, and polyaniline. Table 3-4[102] compares the properties of different conductive polymers. As we can see from the Table 3-4, polythiophene received wide attention for industrial applications due to their electrical properties, low cost, light weight, and high processability. These properties have led polythiophene to be used for electronic and optical devices including light emitting diodes, electrochromic devices, field effect transistors, organic photovoltaics, sensor films, recording materials and rechargeable batteries [103, 104]. However, conventional growth methods lead to thermal and mechanical instabilities in thiophene thin films.[97, 105] Surface polymerization by the ion-assisted deposition (SPIAD) method has been proposed to increase the stability of polymer films by controlling their chemistry and morphology on the nanometer scale[105]. In this thesis, polythiophene is examined to gain an understanding of polymerization and determine the crosslinking mechanisms that dominate during the SPIAD process, which is not commonly used in industry at this time.

Table 3-4. The comparison on conductivity, stability and Processing attributes of representative conducting polymers [102]

Polymer	Conductivity ($\Omega^{-1}\text{cm}^{-1}$)	Stability (doped state)	Processing possibilities
Polyacetylene	$10^3 \sim 10^5$	Poor	Limited
Polyphenylene	1000	Poor	Limited
PPS	100	Poor	Excellent
PPV	1000	Poor	Limited
Polypyrrole	100	Good	Good
Polythiophene	100	Good	Excellent
Polyaniline	10	Good	good

3.2.2 Structure of Polythiophene

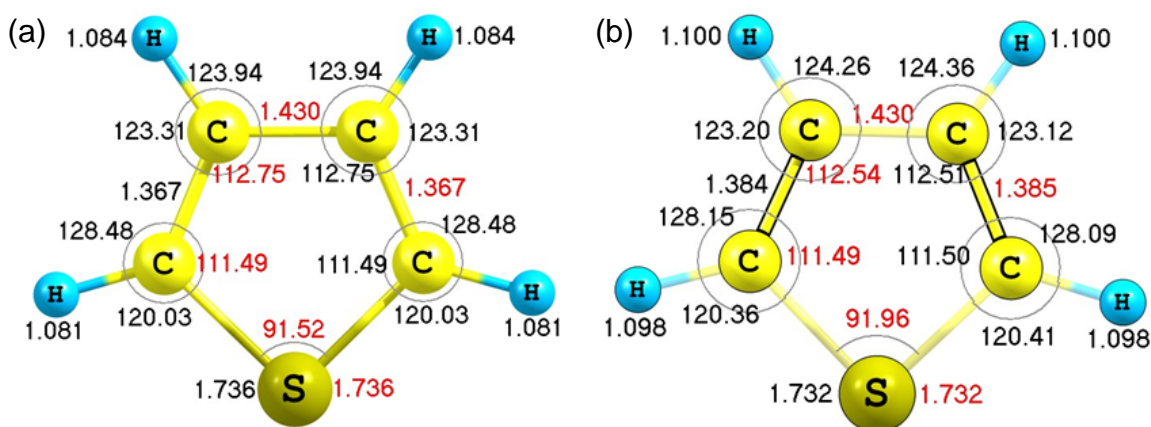


Figure 3-8. The comparison of calculated thiophene structure using (a) Gaussian with B3LYP/6-31G basis set and (b) SIESTA with GGA/PBE and double zeta polarized basis set

Polythiophene is the polymerized form of thiophene, which has the formula unit, $\text{C}_4\text{H}_4\text{S}$. Figure 3-8 compares the thiophene structure calculated using two different calculations. Figure 3-8(a) shows the calculated structure with a hybrid method based on quantum chemical and DFT methods, B3LYP/6-31G, using Gaussian software package. The thiophene structure in figure 3-8(b) is obtained using DFT within the SIESTA package with GGA/PBE pseudopotentials and a double zeta polarized basis set. Normally, quantum chemical method is believed more accurate than normal DFT

method. The two different calculation methods predict very similar structures, with acceptable differences in bond lengths and angles.

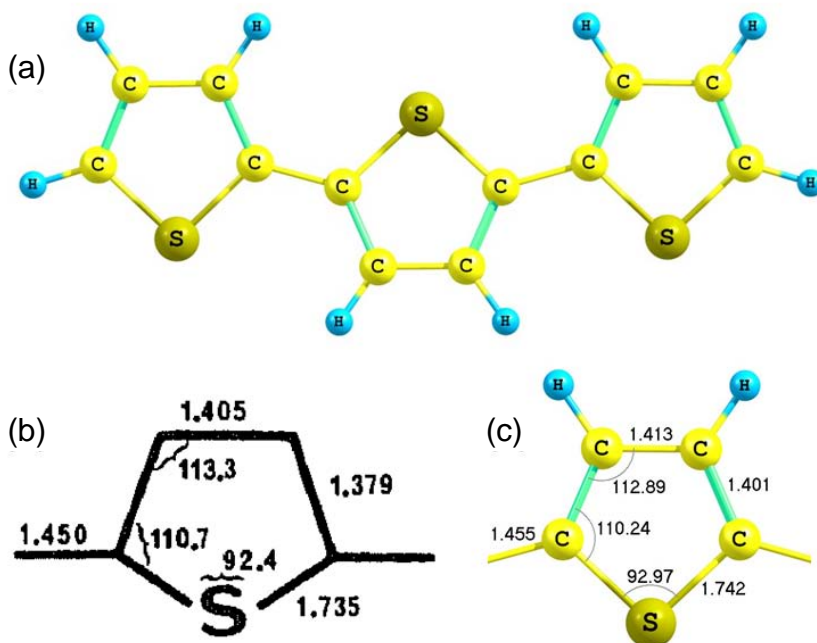


Figure 3-9. The structure of terthiophene; three thiophene rings are arranged in an antiparallel to neighbor.

The conjugated chain of polythiophene plays an important role in the properties of conducting polymer and nonlinear optics. [106] [107] Because the polythiophene displays fluorescence and Raman spectral features similar to terthiophene films [105], terthiophene molecules are examined here. The structure of terthiophene was previously investigated by X-ray and a quantum chemistry study [108]. The structure of polythiophene is determined to show trans position with a continuous antiparallel ordering of thiophene rings, see figure 3-9(a) [108]. Figure 3-9 also shows a comparison of the middle terthiophene ring from (b) an X-ray study and (c) hybrid quantum mechanical calculation with B3LYP/6-31G basis set (c). The two different methods predict similar bond length and angles as the single thiophene structure. The X-ray examination determined the density of terthiophene crystalline as 1.503 g/cm^3 .

The film densities for our simulation study are chosen to be similar to the experimental result.

3.2.3 Conduction Mechanism in Polythiophene

One early explanation of the conducting mechanism in polymers was a half filled valence band created by continuous delocalized π -bonds along the polymer chain [97]. However, polymers favor bond alteration, creating alternative short and long bonds. The energy gap created by bond alternating is about 1.5 eV. This band gap can be controlled by doping with either donors or acceptors. Thus, it is necessary to examine the way that charge is stored along the polymer chain and can be transferred from polymer chain to polymer chain.

Charges can be stored in polymer chains during oxidation or reduction [109] [110]. Different types of oxidizing and reducing dopants are available that do not decrease without lowering its stability. In an oxidation process, positive charge can be localized in a small section of the chain. The localized charge distorts the geometry of the polymer chain, but decreases the ionization energy and increases the electron affinity of the polymer chain. Eventually, the polymer chain becomes electronically conducting by charge delocalization [111].

Figure 3-10 shows the changes in polythiophene chain during oxidation. Initially, polythiophene has a consecutive backbone chain of heterocyclic thiophene, see figure 3-8(a). With oxidizing dopants such as iodine, arsenic pentachloride, iron(III) chloride and nitrosyl (NOPF6), an electron is removed from a p-orbital of the backbone and free radical and spinless positive charge in the polymer chain are created, see figure 3-8(b). The radical and positive charges of the polymer chain are coupled to each other, since the separation of these defects requires a considerable amount of energy. The

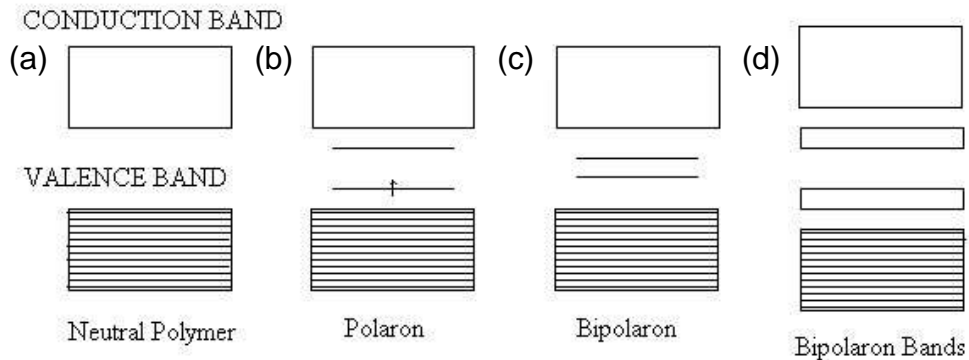


Figure 3-11. The variation of electron band during oxidation. [102]

The nature of charge transfer between polymer chains is not completely understood. However, the main mechanism for charge transport is accepted as a combination thermally activated hopping and tunneling between charged particles such as the polaron and bipolaron.

3.2.4 Growth of Polythiophene

The properties of conducting polymer thin films can vary depending on the growth process. The optimized process can improve the device performance by controlling the charge injection, mobility and recombination efficiency. Thus, development of a processing method which can control film chemistry and morphology at the nanoscale, is a challenge for the application of conducting polymers [112, 113]. Direct thermal deposition and solution-based growth methods are typical growth techniques for conductive polymer thin films. For direct thermal deposition, lower molecular weight oligomers are deposited on the substrate surface. During deposition, the small molecules of gaseous species sublime back to the chamber. For solution-based growth methods, printing, casting or spin coating techniques are used for the growth of polymer. This method causes inadequate or uncontrolled ordering of polymers since the self-

assembly of molecules is the only way to decide the morphology of polymer. Therefore, both growth methods lead to difficulties in controlling the film thickness and morphology.

Surface polymerization by ion-assisted deposition (SPIAD) [105, 114-117], which deposits hyper-thermal polyatomic ions and thermal neutrals in vacuum simultaneously, has been developed to avoid thermal and mechanical instability from conventional growth technology by controlling surface morphology. Both mass-selected and non-mass-selected ions can be used for SPIAD. Selective chemical bonds with self-assembled monolayers are achieved by mass-selected organic cations [118, 119]. Non-mass-selected ion deposition is suitable for prototype manufacturing processes for new conducting polymers [120, 121]. The SPIAD method allows more control over film properties including ion energy, ion structure, ion kinetic energy, charge state, the ion/neutral ratio, and substrate temperature [122]. SPIAD method cannot be only used for optimizing morphology, film thickness, but also fine tuning of film optical band gaps and other optoelectronic properties by modifying the chemical and morphological structure of the film [105, 115, 123]. For example, SPIAD films of polythiophene and polyphenyl display narrower band gaps with reduced barriers for hole injection compared with their evaporated film counterparts [114, 117]. The polythiophene films produced by SPIAD also display fluorescence in the UV and visual region. This property makes polythiophene a candidate for organic photovoltaic device applications. Previous SPIAD studies reported mechanisms for the ion-induced surface polymerization reactions are pronounced at the specific ion/neutral ratios and ion energies [105, 115]. However, SPIAD failed to form a single oligomer state by generating a distribution of species [114, 115]. Also, different experimental results are achieved by using atomic vs.

polyatomic ions. Polyatomic ions behaved both as catalysts and reagents by energetically inducing polymerization and forming adducts with the neutral reagent, respectively [113]. Thus, the utilization of SPIAD for more sophisticated applications requires comprehensive understanding of various mechanisms contributing to the overall film formation. Managing the polymerization process during growth of polythiophene makes it possible to control the optical properties of polythiophene for applications in nonlinear optics and photovoltaic devices.

CHAPTER 4 DOMAIN WALLS IN FERROELECTRIC LITHIUM NIOBATE

4.1 Introduction

Ferroelectric materials have potential use in diverse applications such as non-volatile Ferroelectric Random Access Memory (FRAM)[124], electro-optic modulators[125] and frequency converters[126]. Ferroelectric LiNbO_3 has an $R3c$ structure, has excellent piezo- and pyro-electricity properties, is photo-refractive, and displays nonlinear optical properties[69, 127]. Thus, lithium niobate (LiNbO_3) has many applications in optoelectronics[128], nonlinear optics[129] and micro-electromechanical devices[130]. As we discussed in Sec. 3.1.1, the high-temperature paraelectric trigonal ($R3c$) structure[92] becomes ferroelectric at the Curie temperature by losing its inversion symmetry along the c axis, resulting in space group $R3c$. Since all of the ion displacements associated with the ferroelectricity are parallel to the c -axis (i.e., along $[0001]$), the paraelectric and ferroelectric phases look identical in the top view, figure 4-1.

Gopalan *et al.*[80] identified two crystallographically different 180° domain walls between domains of opposite polarization. As discussed in Sec. 3.1.2, an X-wall lies parallel to a mixed anion-cation plane, while a Y-wall lies parallel to alternating planes of cations only and anions only. Gopalan *et al.* derived a relationship between the domain wall width and energy based on Ginzburg-Landau-Devonshire theory [96]. However, the detailed atomic structure and energetics of these domain walls have not been determined. The objective of this chapter is, therefore, to characterize the structure and energetics of these domain walls. The approach we will take is atomic-level simulation

with empirical potentials, validated against electronic-structure calculations at the level of density functional theory.

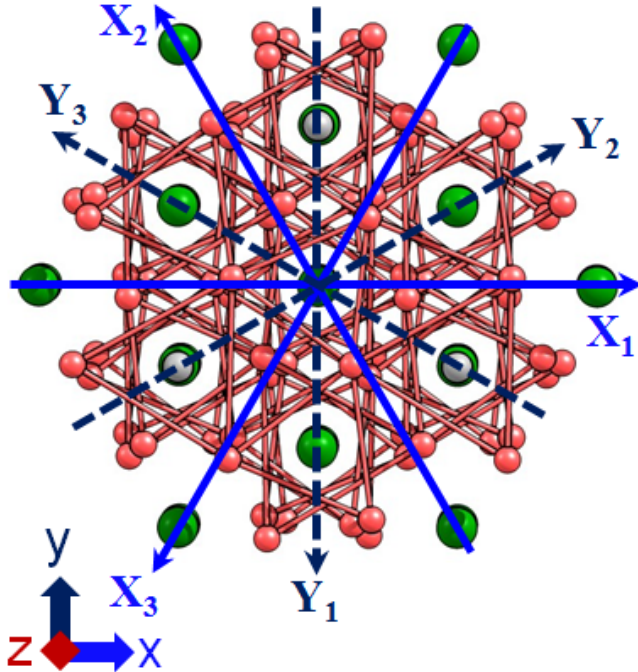


Figure 4-1. Structure of LiNbO_3 (a) Edge view of polarization down (left), paraelectric (center) and polarization up (right) states (b) Planar view of (0001) plane. Three equivalent hexagonal axes are drawn X_1, X_2, X_3 and Y_1, Y_2, Y_3 , with X_1 and Y_1 parallel to the Cartesian x and y axes.

4.2 Domain Wall Preparation

To study these domain walls, we initially prepare two single crystals of the same size: one with polarization up, the other with polarization down. We join these two structures and apply periodic boundary conditions, thereby forming two domains, separated from each other by two crystallographically identical (X or Y) 180° domain walls. We determine the zero-temperature equilibrium structure of each system by allowing all atoms to move to zero-force positions, thereby minimizing the total energy of the system. The system size for DFT calculation is eight unit cells with 240 atoms and 1440 electrons. For empirical study, we increase the system size into $36 \times 4 \times 3$ unit cells

including 12960 atoms in order to prevent interactions between domain walls. The simulations are performed under constant pressure conditions for both empirical and DFT calculations in order to capture the change in a volume as well as atomistic displacements. Both methods show less than 1% change in lattice parameters and volume from bulk ferroelectric values.

4.3 Domain Wall Energy

Although the X-walls and Y-walls are defined to be parallel to the (10 $\bar{1}$ 0) and (11 $\bar{2}$ 0) planes respectively, the actual position of the walls is not determined crystallographically but from minimization of the total energy of the system. The solid and dotted lines in figure 4-2(a) denote planes of high symmetry upon which the domain walls might be expected to lie. For the X-walls, the two high symmetry positions are along the ion planes and between the ion planes. For the Y-walls, the three high-symmetry positions are at the cation plane, at the anion plane, and between two anion planes.

Both the empirical (E) and DFT (DFT) calculations show that the equilibrium positions of the Y-wall lies halfway between the anion planes. The calculations yield a Y-wall energy of $E_Y^{\text{DFT}}=160 \text{ mJ/m}^2$; and $E_Y^{\text{E}}=230 \text{ mJ/m}^2$. That is, the domain-wall energy is defined by the difference in energies of a system with domain walls and a single crystal with the same number of ions, divided by the total area of domain wall in the system. The two methods also agree that the equilibrium position of the X-wall lies equidistant between two ion planes, rather than at an ion plane. The X-wall displays two different variants (X_I and X_{II}) with very similar energies ($E_{X_I}^{\text{E}}=260$ and $E_{X_{II}}^{\text{E}}=255 \text{ mJ/m}^2$), but different polarization profiles; the structural differences between these two variants,

and their origin will be discussed below. The DFT calculations show the same two different structural variants. However, it is not possible to extract individual domain walls energies from DFT, but only the averaged energy value: $\frac{1}{2}(E_{X_I}^{\text{DFT}} + E_{X_{II}}^{\text{DFT}}) = 200 \text{ mJ/m}^2$. Although, as is to be expected, the DFT and empirical values do not precisely agree, both methods do predict the Y-walls to have a lower energy than the X-walls. This conclusion is also consistent with the conclusions of Scrymgeour *et al.*[96] based on calculations using Ginzburg-Landau-Devonshire theory.

It is also possible to estimate the energy barriers for the motion of the domain walls by determining the energy of likely transition states. In particular, we can force the domain wall to be at a specific plane by setting the positions of the ions in the plane to be the average of the two opposite polarization states. For the Y-wall, it seems logical that the cation plane should be the transition state because it is symmetric, lying half-way between two equivalent equilibrium positions. For this highly symmetric state, the empirical simulations yield an energy for the transition state of $E_{\gamma}^{\text{E}^*} = 485 \text{ mJ/m}^2$, see figure 4-2. Assuming that this state is actually the transition state, the empirical calculations thus yield an energy barrier of 255 mJ/m^2 , which is almost identical to the Y-wall energy itself. However, The DFT calculations yield an energy for the transition state of $E_{\gamma}^{\text{DFT}^*} = 310 \text{ mJ/m}^2$, corresponding to an energy barrier of 150 mJ/m^2 , which is only a half of the value obtained from the empirical calculations.

The transition states are slightly different for the two X-wall variants. The energies of the two X-walls when centered at ion planes are calculated to be $E_{X_I}^{\text{E}^*} = 375 \text{ mJ/m}^2$ and $E_{X_{II}}^{\text{E}^*} = 394 \text{ mJ/m}^2$. Thus the estimated energy barrier for X-wall motion is 115 mJ/m^2 for the X_I -wall and 140 mJ/m^2 for the X_{II} wall. The DFT calculations yield an average

transition-state energy of $\frac{1}{2}(E^{\text{DFT}^*_{\text{XI}} + E^{\text{DFT}^*_{\text{XII}}}) = 230 \text{ mJ/m}^2$, corresponding to an average energy barrier of 30 mJ/m^2 . Again, there is a difference in the precise values from the empirical and DFT calculations; however, they both agree that the Y-wall has a higher energy barrier for domain wall motion than the X-walls.

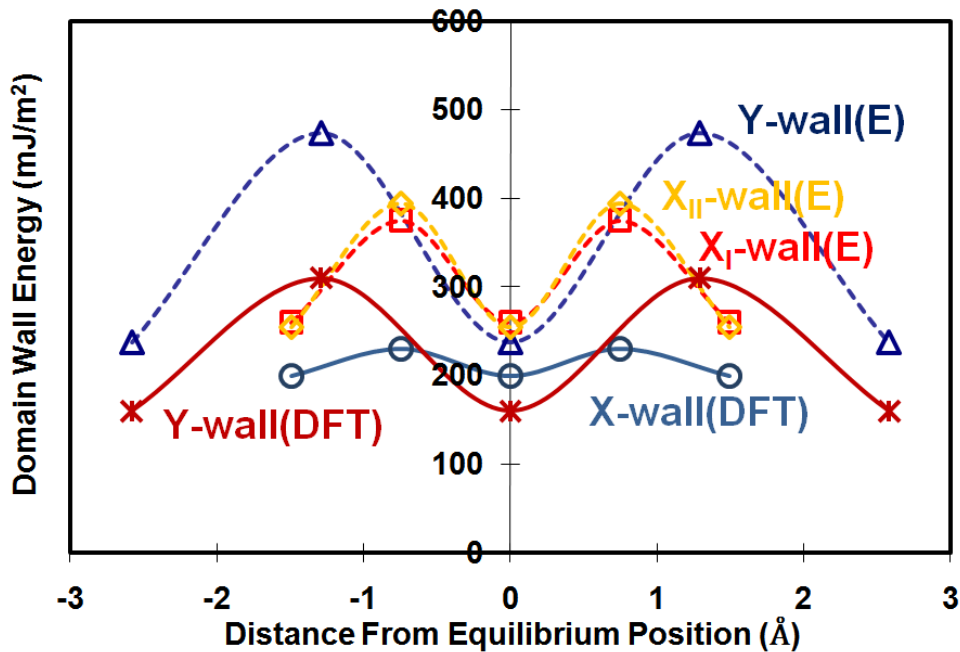


Figure 4-2. Energies of domain walls in equilibrium and in transition states. The equilibrium position is determined as equidistance between two anion planes for Y-wall and center between the cation-anion mixed planes for X-walls. The Y-wall has a lower energy, but higher energy barrier for the wall motion than X-wall. The lines are merely guides to the eye.

4.4 Atomic Displacement around Domain Walls

The domain walls break the crystallographic symmetry of the single crystal. Because of their proximity to two regions of opposite polarization, the atomic structure in the planes close to the domain walls should be a close approximation to the paraelectric structure, converging to the ferroelectric structure at some distance from the domain wall. Moreover, the domain walls produce displacements, not only parallel to the polarization direction (z), but also in the x - y plane, with both components normal to and

parallel to the domain wall. Following the notation of Scrymgeour *et al.* [96], we denote displacements and polarizations normal to the domain wall as “normal” or “n”, and those parallel to the domain wall (but orthogonal to the bulk uniaxial polarization) as “transverse” or “t”. Close to the domain walls, all three components of polarization can be manifested.

4.4.1 Y-walls, Parallel to c-glide Planes

The Y-wall lies between two anion planes separated by only 0.64 Å. The oxygen ion displacements in these planes are therefore large, as shown in figure 4-3. For the Y_1 domain wall, the O2 ions are closest to the domain-wall plane (~ 0.30 Å) and show the largest Z-displacement from their ferroelectric positions, 0.23 Å. Because this displacement is almost as large as the displacement from the paraelectric to ferroelectric positions in bulk, we can understand this as the O2 ions moving back to positions close to their positions in the paraelectric phase. The next closest, O3 ion, is ~ 0.35 Å from the Y-wall and shows a slightly smaller Z-displacement of 0.21 Å. The O1 ion which sits further away yet, 0.65 Å, shows an even smaller Z-displacement. The oxygen ion positions finally recover their bulk ferroelectric positions at a distance of ~ 5.8 Å away, as defined by the displacement from the ferroelectric positions dropping below 10% of its maximum value.

Since at equilibrium the Y-wall lies between two anion planes, the closest cation planes are much further away, 1.3 Å, and thus undergo significantly smaller Z-displacements than the anions. Interestingly, the symmetries of the cations are also broken by the Y-wall. However, in this case the symmetry breaking does not arise from the wall itself, but as a secondary effect caused by the breaking of the symmetry of the O1, O2 and O3 ions. For example, the top Li in figure 3-4(c) is in an oxygen cage of

different orientation than the oxygen cage enclosing the lower Li ion. Therefore, although they are the same distance from the Y-wall, these two distinct Li_I and Li_{II} ions undergo different Z-displacements (0.02\AA and 0.00\AA). Similarly, the distinct Nb_I and Nb_{II} ions also undergo Z-different displacements (0.019\AA and 0.016\AA). The maximum cation displacements of both Nb and Li ion are, unsurprisingly, in the planes closest to the Y-wall. These cation displacements are in the direction opposite to the displacements associated with the ferroelectricity, indicating that the cations are displaced back towards their paraelectric positions. The cations recover their ferroelectric positions $\sim 11.7\text{\AA}$ from the wall, which is twice the distance of that required by the anions.

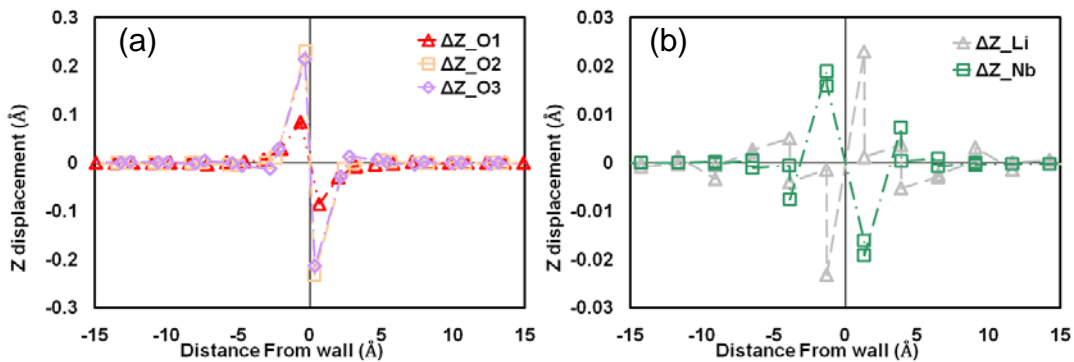


Figure 4-3. Displacement pattern in z-direction of (a) oxygen ions and (b) cations around Y-wall. Note the difference in scales of displacements.

Because the oxygen ions near the Y-wall shift oppositely poled ferroelectric states to approximately paraelectric symmetric position at the domain walls, the oxygen ions on opposite sides of the domain wall displace in opposite transverse directions. If an oxygen ion moves along the positive y-axis along on one side of the wall, the crystallographically equivalent oxygen ion on the opposite side moves along the negative y-axis. For displacements normal to the wall, symmetric oxygen ions on opposite sides displace equally either toward or away from the Y-wall regardless of

ferroelectric state. Figures 4-4(a) and (b) shows the transverse and normal displacements of the oxygen ions in the region around a Y-wall; Figs. 4-4(c) and (d) show the corresponding displacements for the cations. Here, the positive and negative signs of the transverse displacement correspond to movement in the +y- and -y- directions. Figure 4-4(c) shows the transverse displacements of cations at the nearest cation plane of the up-polarized region; the transverse displacements for down polarization side are equal and opposite. For normal displacements, the positive and negative signs denote displacement movement away from and towards the Y-wall respectively.

The transverse displacements of the three different non-symmetric oxygen ions can be analyzed in a similar manner. As figure 4-4(a) shows the O1, O2 and O3 ions on the one side of the wall displace in opposite directions from their counterparts on the other. Because the closest anion to the wall, O2, shows the largest displacement in z direction, it also has the largest transverse displacement, $O2_T \sim 0.066 \text{ \AA}$.

As we can see from figure 4-4(b), the normal displacements of oxygen ions show the same pattern on the two sides of the domain wall. For the Y_1 axis, the O1 ions have the same x positions, but different y positions in the two different ferroelectric states; they thus displace along only in the transverse direction. Specifically, the simulations show that the Y-wall pushes the O1 ion away from the wall; the normal displacement is $O1_N \sim 0.02 \text{ \AA}$ at the nearest oxygen plane.

The normal displacements of the O2 and O3 ions are almost equal and opposite to each other ($O2_N \sim -0.15 \text{ \AA}$ and $O3_N \sim 0.13 \text{ \AA}$) because the Y_2 and Y_3 axes are oriented at -60° and $+60^\circ$ angle to the Y-wall. These displacements are larger than the ferroelectric

displacements, $\pm 0.11\text{\AA}$, resulting in additional normal displacements of oxygen ions which break the paraelectric symmetries of oxygen ions near the Y-wall.

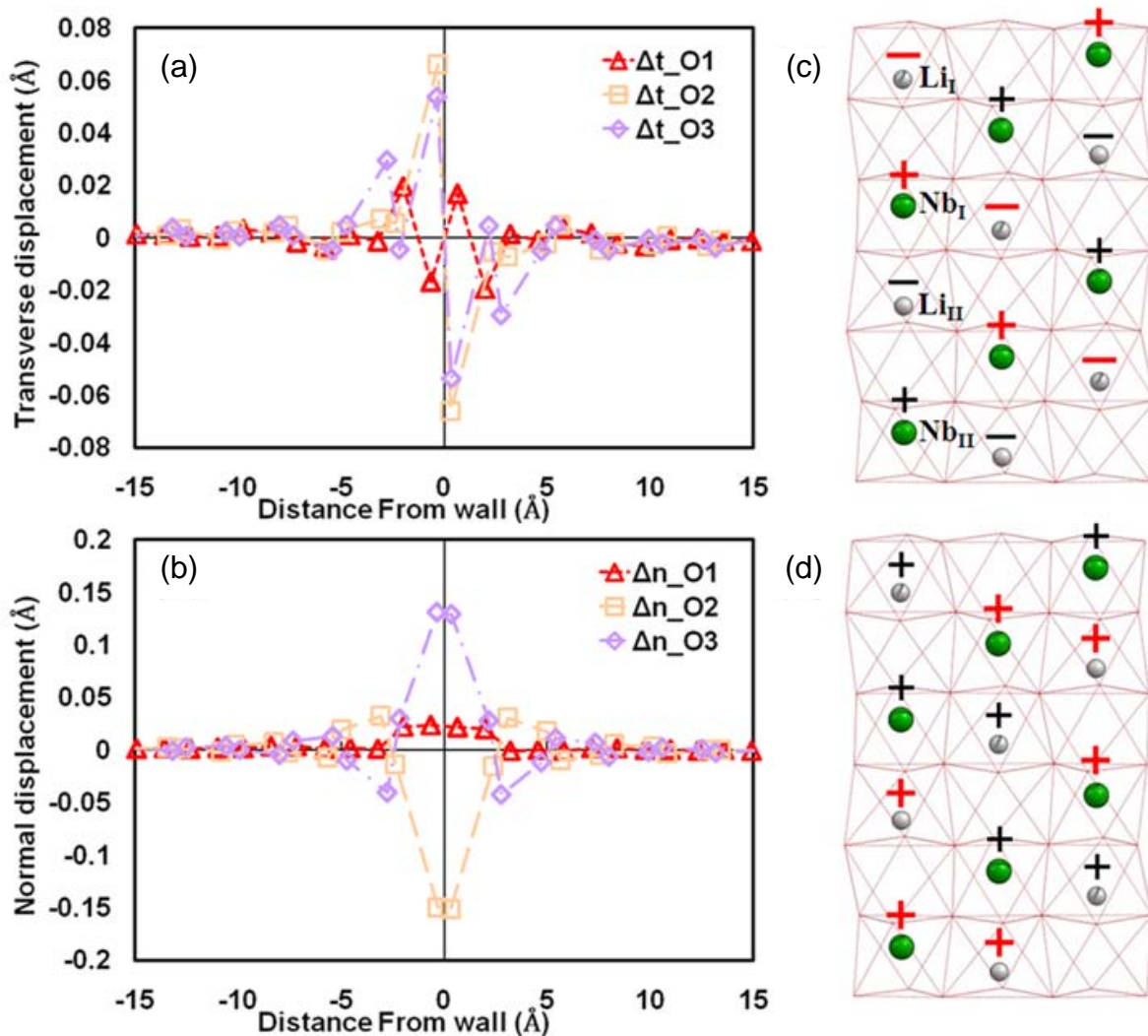


Figure 4-4. Atomic displacements of O1, O2 and O3 ions in (a) transverse, and (b) normal direction directions near a Y-wall. Schematic view of corresponding cation displacements along (c) transverse and (d) normal directions. Relative larger + signs (red) and smaller + signs (black) represent larger and smaller cation displacements. For transverse displacements, the plus and minus sign indicate the positive and negative displacement along Y1 axis. For normal displacement, the plus sign indicates that the cation moves away from the Y-wall, while the minus sign designates that cation displaces towards Y-wall.

The broken symmetry of the oxygen ions also causes the cations to break the uniaxial symmetry around the Y-wall. Figures 4-4(c) and (d) show schematic views of

the transverse and normal cation displacements for the cation plane closest to the Y-wall, at which the displacements are largest. The Li_I and Nb_I show relatively larger transverse displacements than the Li_{II} and Nb_{II} ions. As we can see from figure 4-4(c), the Li and Nb ions displace in opposite transverse direction, although Li_I and Li_{II} ions displace in same transverse directions, as do the two types of Nb ions. Figure 4-4(d) shows that all of the cations near Y-wall are displaced in the normal direction away from Y-wall. Because of their weaker electrostatic interactions with the oxygen ions, the Li ions displace more than the Nb ions. Because of the differences in the symmetries of the displacement pattern along the transverse and normal direction, the normal displacements of cations converge to zero at relatively longer distances from the Y-wall ($\sim 11.67 \text{ \AA}$) than the transverse displacement ($\sim 6.48 \text{ \AA}$).

4.4.2 X-walls, Perpendicular to c-glide Plane

The structure of the X-wall is very different from that of the Y-wall for two reasons. Most importantly, the X-wall lies parallel to planes that contain both anions and cations. More subtly, because it lies at 30° to the Y-wall, the X-wall is normal to one of the Y-directions, and at $\pm 30^\circ$ to the other two. Because of the differing oxygen displacements on the oxygen sublattices, this creates two X-wall variants, depending on whether the other oxygen displacements point into the X-wall or point out of the X-wall. In particular, as figure 4-5(a) shows, when the Y_2 direction is perpendicular to the X-walls, the O2 ions mainly displace in the normal direction into the domain wall, leading to the X_I -wall. An O2 ion sitting near the X_I -wall moves in the $+Y_2$ direction for the up polarization and in the $-Y_2$ direction for the down polarization state. Both of these displacements represent normal displacements toward the X_I -wall. Likewise, figure 4-5(b) shows that when the Y_3 direction is perpendicular to the X-wall, the O3 ions displace along the

normal direction away from the domain wall. This direction is opposite to that for X_I -wall, thus creating a different variant, the X_{II} -wall. The positive displacement of the O3 ion along Y_3 axis near the X_{II} -wall for up polarization and negative displacement for down polarization indicates the movement of O3 ions away from the X_{II} -wall.

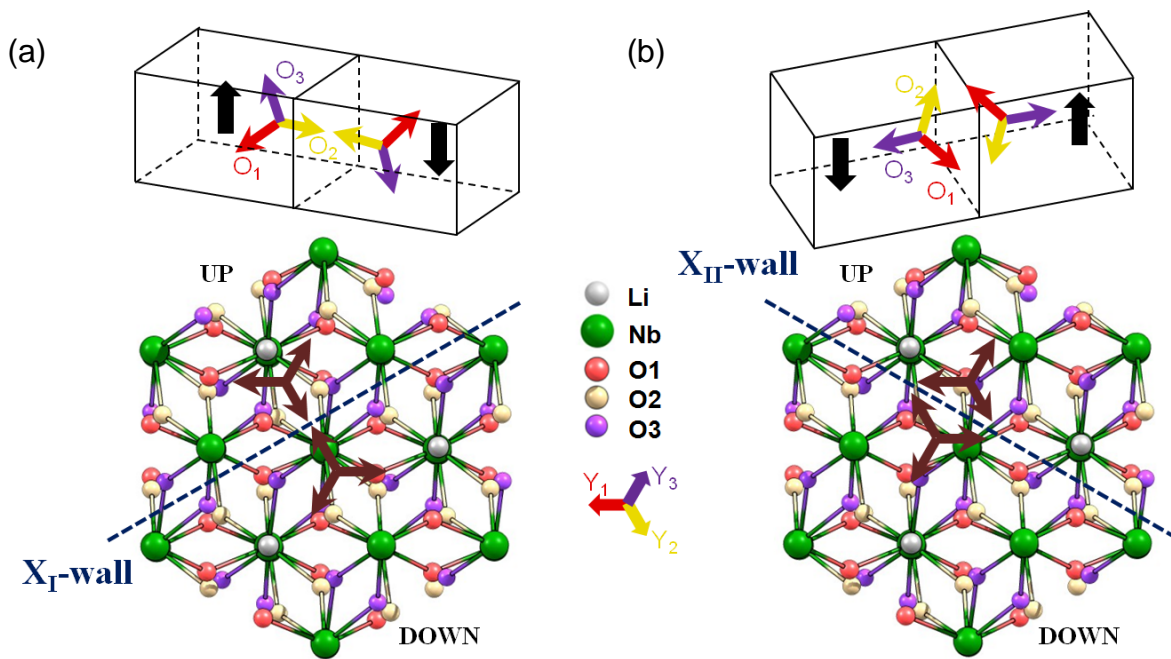


Figure 4-5. Crystallographies of the X_I -wall and X_{II} -wall.

Figures 4-6(a) and (b) show the displacement patterns of the anions and cations in the Z-direction around the X_I -wall. The Z-displacement is largest in the planes closest to the domain wall, decaying to zero at $\sim 5\text{\AA}$ from the wall. The corresponding cation displacements are much smaller, with the cations moving closer to their paraelectric positions. Figures 4-6(c) and (d) show the anion and cation displacements around the X_{II} -wall. The Z-displacements of the oxygen ions are quite similar for the two X-wall variants, except that the maximum Z-displacement of the X_{II} -wall is slightly larger (0.19\AA vs. 0.17\AA). However, comparing Figs. 4-6(b) and (d), there are significant differences in the cation displacements. For the X_I -wall, the maximum Z-displacement of both cations

is observed at the nearest plane. For the X_{II} -wall, the Li and Nb ions move by the same amount in the Z-direction at the closest plane, thereby compensating for the displacement of oxygen positions in the Z-direction. As a result, the Li ion closest to its paraelectric position is at the second nearest plane. In contrast to the Y-walls, there is only one type of Z displacement pattern for Li ion and Nb ion in the X-walls.

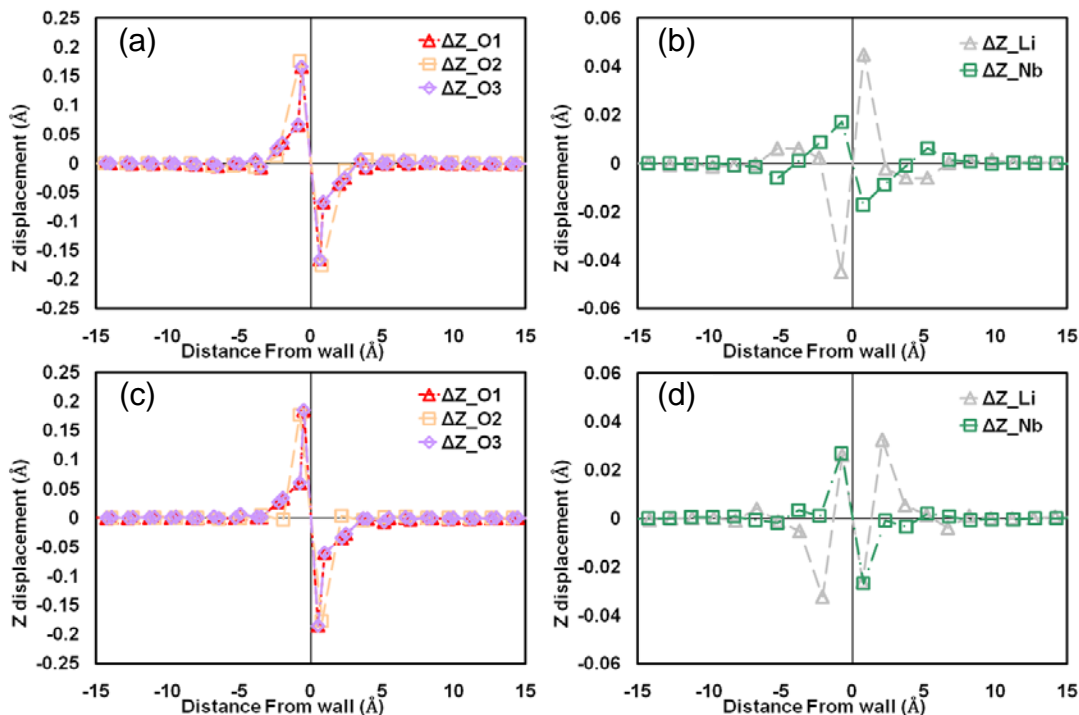


Figure 4-6. The Z-displacements patterns around X_I -wall and X_{II} -wall. (a) The anion displacement pattern around X_I -wall (b) The cation displacement pattern around X_I -wall (c) The anion displacement pattern around X_{II} -wall (d) The cation displacement pattern around X_{II} -wall

The two X-wall variants also create two distinct patterns of normal and transverse ion displacements, see figure 4-7(a). The negative sign in the normal displacement for the O2 ions indicates that they move toward the X_I -wall; the O1 and O3 ions move away from X_I -wall by equal amounts along their internal Y-axes. In a similar manner, figure 4-7(b) shows the displacements of the anions near X_{II} -wall. The maximum normal

displacement ($\sim 0.17 \text{ \AA}$) at the plane closest to the wall disappears $\sim 5 \text{ \AA}$ away from both of X-walls.

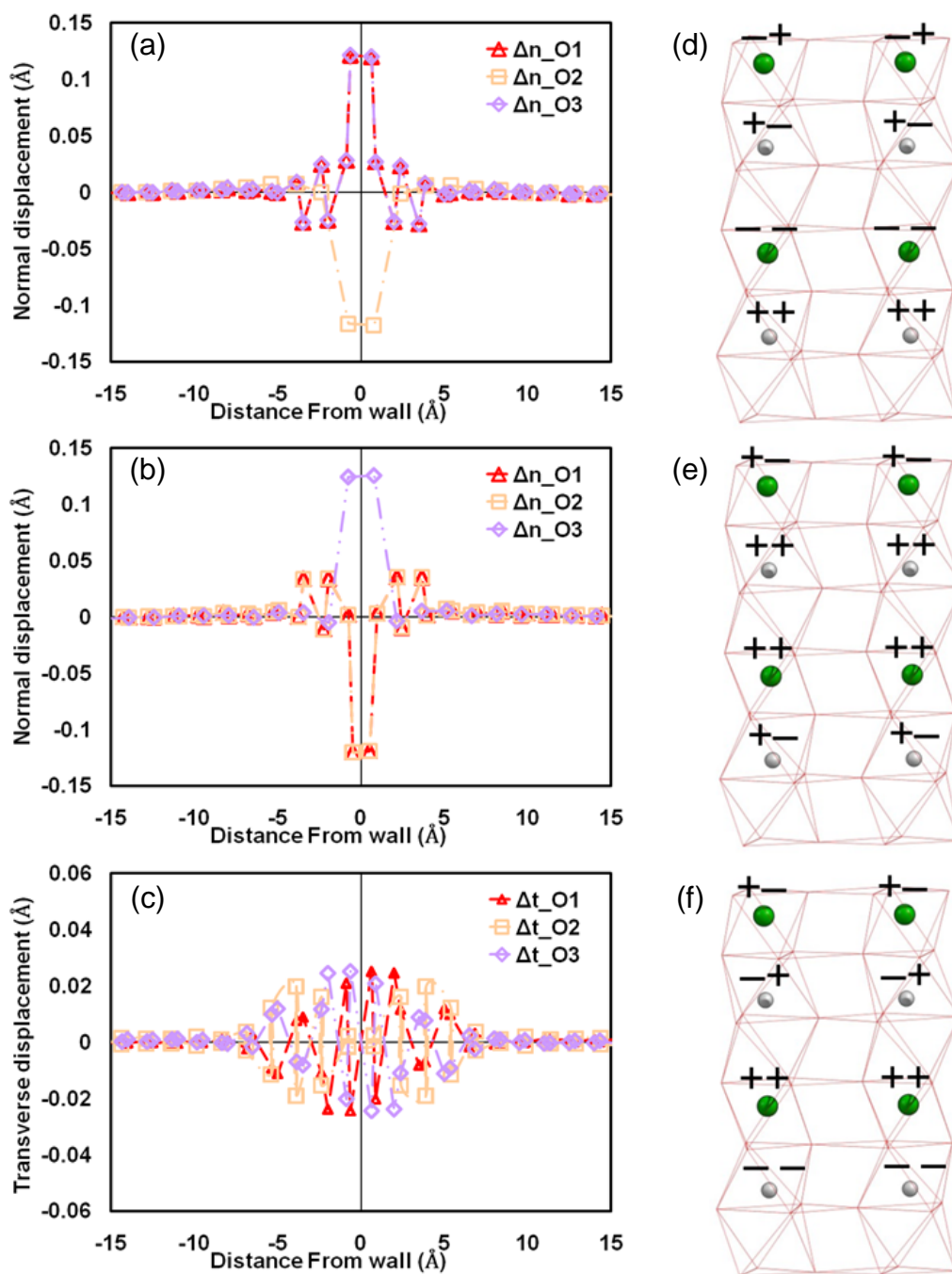


Figure 4-7. Normal displacements of three different oxygen ions near (a) X_I -wall and (b) X_{II} -wall. (c) transverse displacements of three different oxygen ions around X_I -wall. (d) normal and transverse displacement of cations around X_I -wall. Normal displacement of cations around X_{II} -wall at (e) the nearest and (f) the second nearest plane.

Figure 4-7(c) shows the transverse displacement of the anions around the X_I -wall; the displacements for the X_{II} -wall are very similar. All of the transverse displacements of the anions are cancelled by equal and opposite displacement patterns. The displacement of cations around the two X-walls are shown in figure 4-7(d) through (f). Unlike the Y-wall, only one normal displacement pattern for each cation is observed for both X-walls. Figure 4-7(d) shows the cation displacement around the X_I -wall. The first +/- sign for each cation represents the normal displacement, while the second +/- sign designates the transverse displacement of the cations. The Li and Nb ions, which move in opposite normal direction, show the largest displacement at the second nearest plane from X_I -wall. Both Li and Nb ions in the first plane move away from the X_{II} -wall, figure 4-7(e). However, the Li ions in the second plane move into the X_{II} -wall while the Nb ions shift away, figure 4-7(f). The transverse displacement of the cations are very similar to the anion displacement. Unlike the normal and Z displacement pattern of cations, the nonsymmetric cations, Li_I , Li_{II} and Nb_I , Nb_{II} , show opposite displacements in the transverse direction. Therefore, the equal and opposite transverse displacement of each cation along Z-direction are cancelled out.

4.5 Polarization at Domain Walls

The switching of the polarization at a ferroelectric domain wall is generally considered to be relatively abrupt, taking place over only one or two unit cells.[131] However, the relatively long distances (up to $\sim 10\text{\AA}$) over which the atomic displacements return to bulk values suggest that the polarization may be governed by a similar length scale. In this section, we characterize the transition in the uniaxial polarization, and in the components of polarization normal to and transverse to the domain wall. As we shall see, these more complex polarization patterns manifest some

features reminiscent of those present in ferromagnetic domain walls in which the spin state switches from one to another over, typically, many tens of unit cells.[132] However, because of the much greater strength of electrostrictive interactions compared to magnetostrictive interactions, the non-uniaxial components are relatively small and characterized by shorter length scales than their magnetic counterparts.

4.5.1 Y-walls

We have determined the polarization along the direction to the normal Y-wall using both empirical potentials and DFT. As is customary,[133] for the DFT calculation only the ionic contributions to the polarization are considered. For the calculation, we use the Born effective charge developed by Veithen and Ghosez[85] for LiNbO₃ ferroelectric system. As figure 4-8(a) shows, the two methods give very similar profiles in the uniaxial contribution to the polarization. The asymmetric pattern of up and down polarization arises from the shift in the Y-wall from the anion plane to the equilibrium positions; as a result, one of the domains is wider than the other. We note that using the full ionic charge in analyzing the DFT results, rather than the Born effective charges, leads to almost complete overlap with the polarization profiles determined from the empirical potentials. We take the good agreement between the DFT and empirical results as validation for the larger scale calculations using the empirical potentials, which show a change in P_z over a very short distance, see figure 4-8(b).

The non-uniaxial displacements of the ions generate non-uniaxial contributions to the polarization. Figure 4-8 shows (c) the normal and (d) the transverse polarization around the Y-wall. Both are anti-symmetric around the domain wall, with zero polarization contributions at the center of domain wall. The normal and transverse

polarizations show maximum of values of $0.60\mu\text{C}/\text{cm}^2$ and $1.66\mu\text{C}/\text{cm}^2$ at 2.58Å , decaying to zero $\sim 9\text{Å}$ away from the wall.

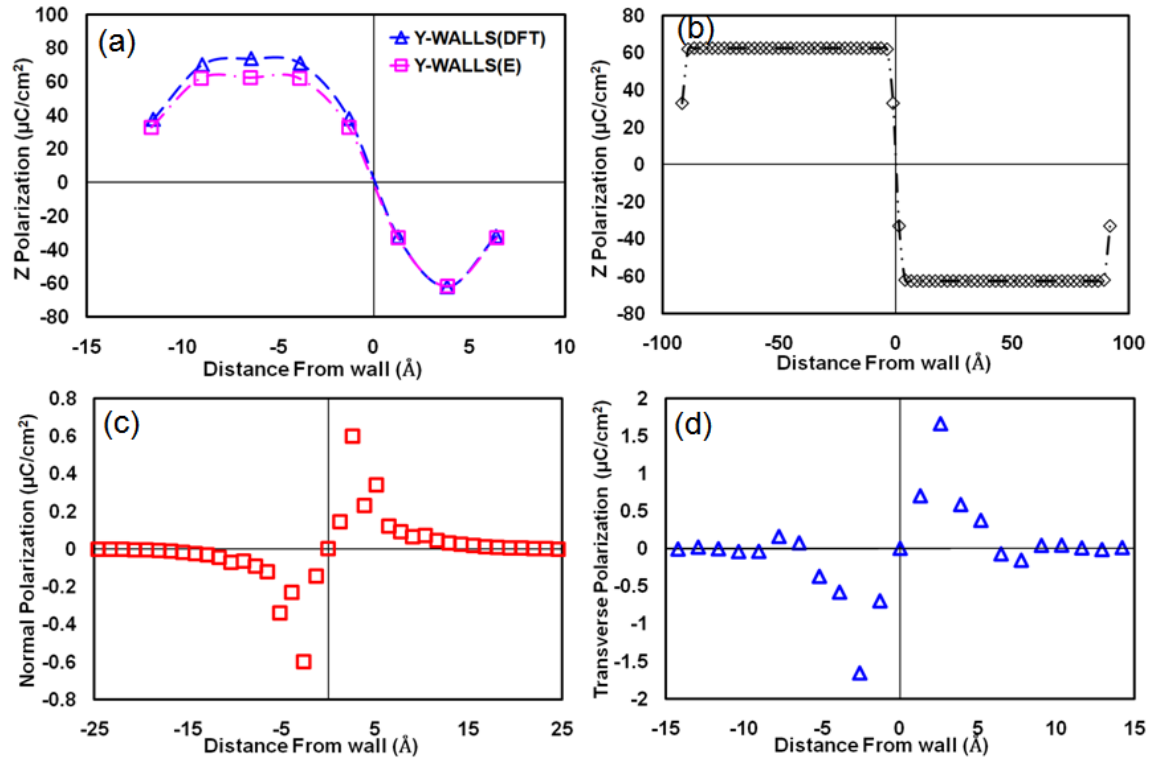


Figure 4-8. (a) Comparison of z directional polarization (P_z) around Y-walls, determined by DFT and empirical simulation methods. (b) Uniaxial polarization profile of larger simulation cell with Y-wall. Variation of in-plane polarization near Y-wall; Normal(c) and transverse. (d) polarization profile at each side of Y-wall show exactly symmetric with opposite sign.

A 180° ferroelectric wall is typically understood as Ising-type, see figure 4-9(a); by contrast a 180° magnetic wall is typically understood as Bloch or Néel-type.[134] The presence of significant polarization components P_n and P_t of up to $\sim 2.66\%$ of P_z gives rise to a Bloch-like and a Néel-like contribution to the predominantly Ising-like Y-wall.[135] The polarization vector, $\mathbf{P}_z + \mathbf{P}_t$ leads to a Bloch-like rotation by angle θ_B in the t - z plane of the domain wall, figure 4-9(b), whereas polarization vector, $\mathbf{P}_z + \mathbf{P}_n$ leads to a Néel-like rotation by angle θ_N in the n - z plane perpendicular to the domain wall, figure 4-9(c). The maximum rotation angles of $\theta_B \sim 1.52^\circ$ and $\theta_N \sim 0.55^\circ$ occur at a distance

$x_n \sim \pm 1.3 \text{ \AA}$ from the Y-wall where the P_n and P_t components are maximum. Thus the Y-wall has a relatively strong Bloch-like rotation behavior and a weak Néel-like rotation behavior.

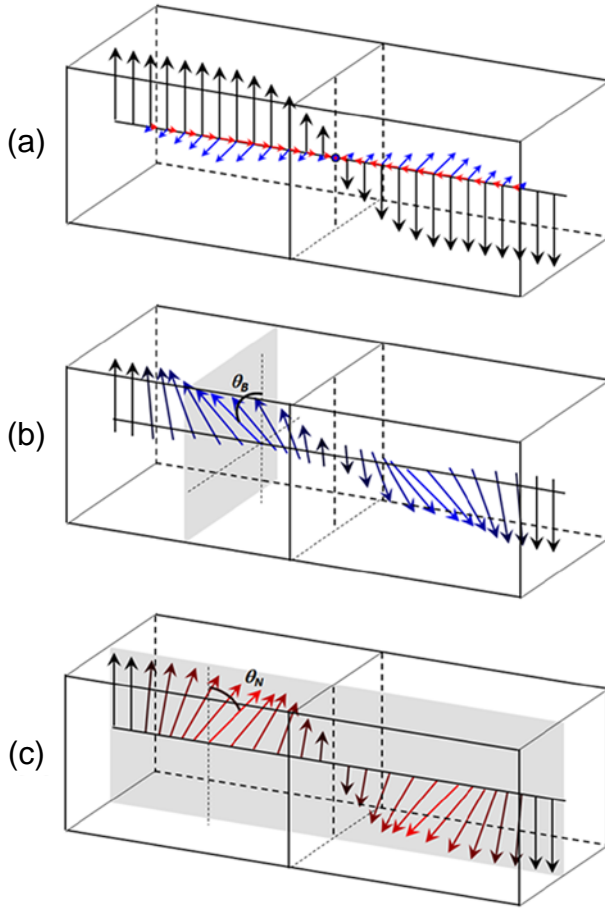


Figure 4-9. Schematic representation of (a) three different polarization, P_z , P_t and P_n ; (b) Bloch-like wall is created by vector sum of P_z and P_t and (c) Néel-like wall is created by vector sum of P_z and P_n . θ_B and θ_N is calculated by maximum rotation angle of P_z at the position where P_z returns to bulk polarization value.

4.5.2 X-walls

As in the case of the Y-wall, the empirical and DFT calculations yield very similar polarization patterns around the X-walls, see figure 4-10(a). To understand the polarization pattern around the X-walls without the limitations of small system sizes, we again performed larger scale simulations with the empirical potentials. For the geometry

used in this study, the X_I -wall lies at center of the system, while the X_{II} -wall lies on the periodic boundary at $\pm 70\text{\AA}$. As we can see from the figure 4-10, both X-walls show very sharp transition regions between polarization states. The bulk polarization of $62.4\mu\text{C}/\text{cm}^2$ is reached at $\sim 6\text{\AA}$ away from X_I -wall and at $\sim 9\text{\AA}$ away from X_{II} -wall.

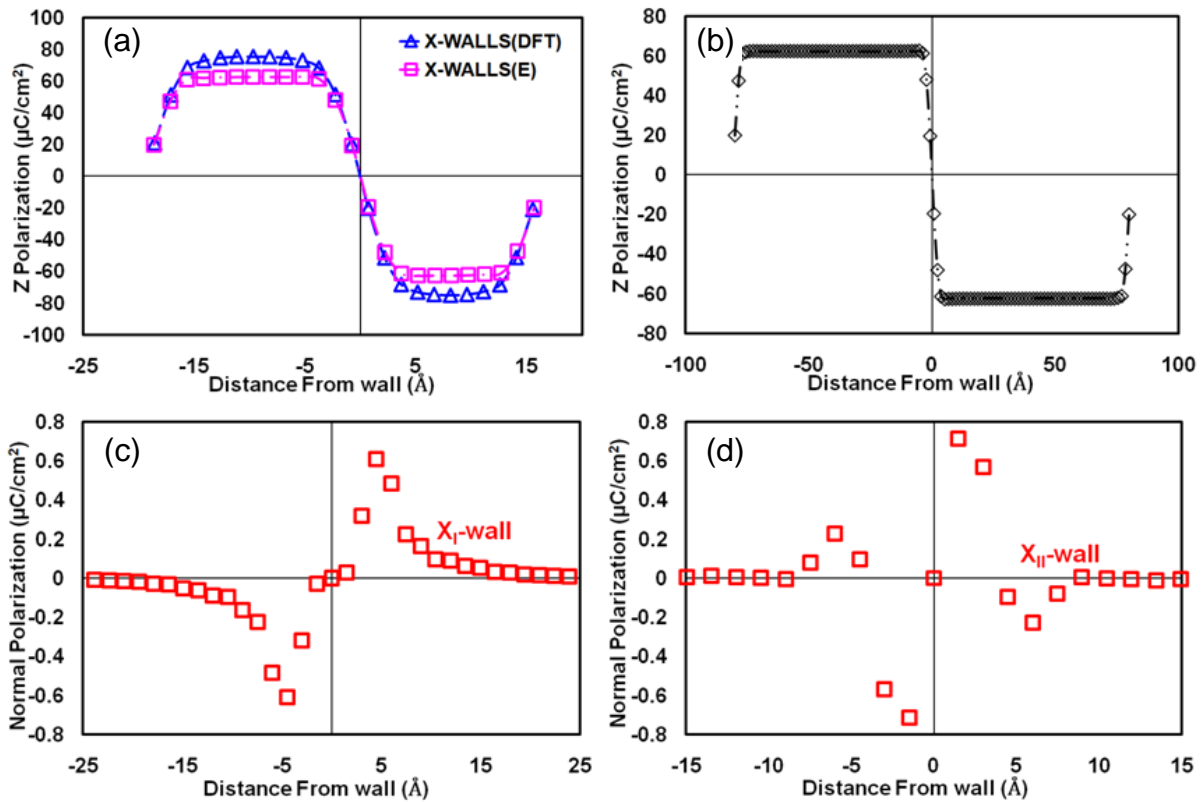


Figure 4-10. (a) Comparison on Z directional polarization around X-walls between DFT and empirical simulation methods. (b) Uniaxial polarization profile of larger simulation cell with X-walls. Two different X-walls are created at the center(X_I -wall) and at the boundary(X_{II} -wall). (c) The variation of in-plane polarization around X-walls; Normal polarization profile near X_I -wall(c) and X_{II} -wall(d).

Because the atomic displacements in the transverse direction are cancelled by equal and opposite movement of each ion, figure 4-7(c), there are no transverse polarizations at the X-walls. Figures 4-10(c) and (d) show the normal polarization profile around the X_I -wall and X_{II} -wall respectively. The different normal polarization patterns near the two X-walls are the result of different displacements of the cations. With the

largest normal displacements at the second nearest plane, the maximum polarization of $0.61\mu\text{C}/\text{cm}^2$ out of X_I -wall is observed at 5.2 \AA away, slowly decreases in a monotonic manner, reaching 10% of its maximum value about $\sim 15\text{ \AA}$ away. The change in normal displacement pattern of cations between the first and second nearest plane to X_{II} -wall generates the maximum outward polarization of $0.71\mu\text{C}/\text{cm}^2$ at 1.49 \AA and leads to oscillatory convergence over a distance of $\sim 9\text{ \AA}$.

Considering the maximum Bloch-like and Néel-like rotation angles near the X-walls, the angles are $\theta_B \sim 0^\circ$ and $\theta_N \sim 0.56^\circ$ for the X_I -wall and $\theta_B \sim 0^\circ$ and $\theta_N \sim 0.65^\circ$ for the X_{II} -wall. Thus, both of X-walls show only Néel-like rotation.

4.6 Domain Wall Width

The Ginzburg-Landau-Devonshire (GLD)[136-138] thermodynamic theory successfully explains the relationship between the variation of the polarization and domain wall width in the transition region for both perovskite materials[137] and for trigonal ferroelectrics such as LiNbO_3 and LiTaO_3 [96]. In the transition region, the total free energy of a ferroelectric material can be understood as arising from four different energy components[139, 140]: a free energy associated with the second order phase transition, a free energy associated with elastic lattice displacement, a free energy derived from structural distortion by non-uniform polarization, and a free energy associated with gradient in the polarization.

Solving the free energy equation for energy minima, Scrymgeour *et al.*[96], showed the relationship between three components of polarizations, P_n , P_t , and P_z as:

$$P_z(x_n) = P_0 \tanh\left(\frac{x_n}{\omega_0}\right) \quad (4-1)$$

and

$$\begin{bmatrix} P_n(x_n) \\ P_t(x_n) \\ P_z(x_n) \end{bmatrix} = \begin{bmatrix} \rho_{n1} & \rho_{n2} & \rho_{n3} \\ \rho_{t1} & \rho_{t2} & \rho_{t3} \\ 1 & 0 & 0 \end{bmatrix} \times \begin{bmatrix} P_z \\ P_z^3 \\ P_z^5 \end{bmatrix} \quad (4-2)$$

where, ρ_{ik} ($i=n,t; k=1,2,3$) are the coefficients of the polynomials.

Our atomic scale simulation study also shows that non-uniaxial polarizations are strongly correlated to the uniaxial polarization. While P_z shows a kink type polarization variation, reaching zero at the center of the wall, P_n and P_t are zero both at the center of the wall and far away from the wall. The simulations discussed above show that in-plane polarizations reach their maximum value at approximately distance from the domain wall at which P_z returns to bulk value. Thus, P_n and P_t returns to zero bulk value at relatively longer distance than P_z . Because, no complete model has been developed for the non-uniaxial polarizations of trigonal systems, we only show the domain wall width along with P_z component in this study. A fit of P_z to a single hyperbolic function, equation (4-2), yields $\omega_o \sim 2.16 \pm 0.05 \text{ \AA}$. Figure 4-11 shows normalized polarization profiles of P_z along x_n around the Y-wall. The solid line is a fit to simulation results for P_z .

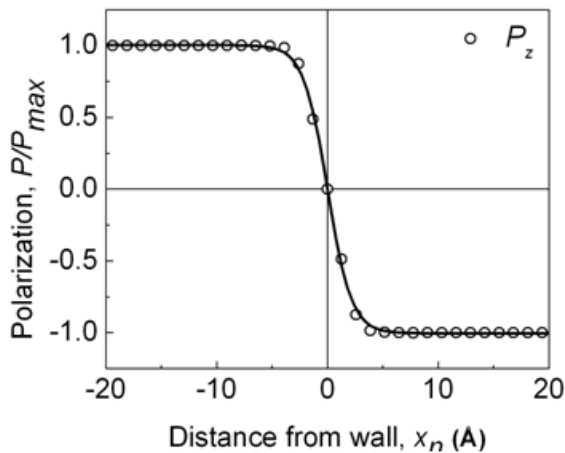


Figure 4-11. A fit of P_z to hyper-tangent function around Y-wall. Equation (4-2) yields the domain wall width $\omega_o \sim 2.16 \pm 0.05 \text{ \AA}$.

The two X-walls yield essentially identical domain wall widths: $\omega_o \sim 2.10 \pm 0.03 \text{ \AA}$ for the X_I -wall and $\omega_o \sim 2.12 \pm 0.03 \text{ \AA}$ for X_{II} -wall, as shown on figure 4-12. The fits of P_z to the hypertangent function lead very similar domain wall width for three different types of domain walls. The absence of analytic results for non-uniaxial contributions to the polarization indicates that there is still scope for further developments in the GLD analysis of these domain walls.

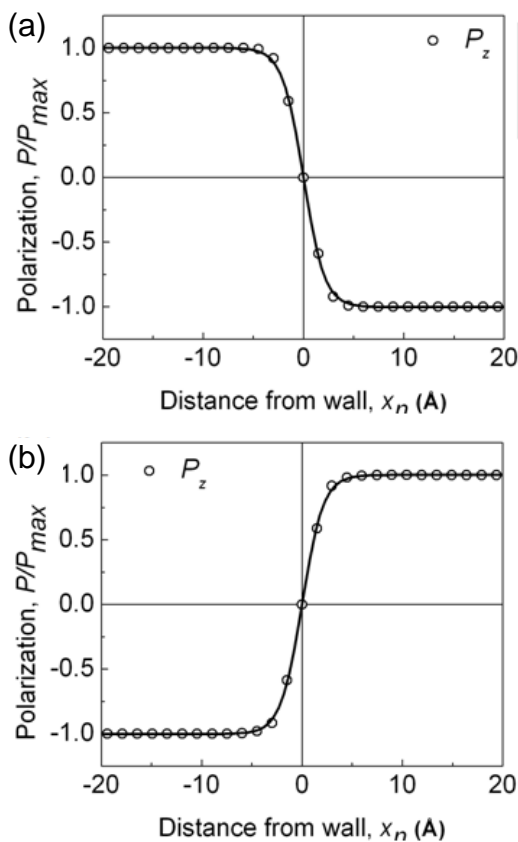


Figure 4-12. Fits of P_z of (a) X_I -wall and (b) X_{II} -wall to Equation (4-2). The fits of P_z yield almost same pattern between Y-wall and two X-walls. Further analysis on in-plane polarization is required for the comparison.

4.7 Threshold Field for Domain Wall Motion

Ishibashi[141] and Suzuki[142] showed that the width of the domain wall controls domain wall motion with the activation energy for wall motion being inversely

proportional to its width. In their analysis, the activation energy for domain wall motion, can be expressed as a free energy difference between equilibrium state and transition state, $\Delta F_{activation}$:

$$\Delta F_{activation} = F_{Transition} - F_{Equilibrium} \approx \alpha_1 P_s^2 w_0 \left(\frac{w_0}{a} \right)^3 \exp\left(-\frac{\pi^2 w_0}{a} \right) e^4 \left(\frac{\pi}{2} \right)^{7/2} \quad (4-3)$$

where α_1 and α_2 are the constant in the GLD polynomial, w_0 is domain wall half width, P_s is spontaneous polarization and a is lattice constant. From this the threshold field for domain wall motion can be determined as the activation energy dividing by $w_0 P_s$ [143].

In the Sec. 4.6, we obtained domain wall widths by fitting the P_z profiles. The lattice parameter for Y-wall shows $a \sim 5.1684 \text{ \AA}$ and spontaneous polarization $P_s \sim 62.4 \mu\text{C}/\text{cm}^2$. The coefficients for the GLD polynomial constants can be determined from the polarization and Curie-Weiss law:

$$P_s = \sqrt{\frac{\alpha_1}{\alpha_2}} \quad \text{and} \quad \alpha_1 = \frac{1}{\epsilon_r - 1} \quad (4-4)$$

Table 4-1. Comparison of constants in equation (4-3)

Parameters	This works	Literature[96]	Units
A	5.1684	5.1474	$\times 10^{-10} \text{ m}$
α_1	5.04	2.012	$\times 10^9 \text{ Nm}^2/\text{C}^2$
α_2	12.95	3.608	$\times 10^9 \text{ Nm}^6/\text{C}^4$
P_s	62.4	75	$\mu\text{C}/\text{cm}^2$

The comparison between the calculated constant values and literature value for the parameters entering equation (4-3) is listed in Table 4-1. Using Table 4-1 and equation (4-3), we obtain the activation energy and threshold field for the different

domain walls. Because the three domain walls have essentially identical widths, equation (4-3) yields almost the same value in activation energy and threshold field. The calculated activation energies are $\Delta F_{acti} \sim 133 \text{ mJ/m}^2$ and $E_{th} \sim 1.0 \times 10^9 \text{ V/m}$ with the GLD parameters calculated, and 77 mJ/m^2 and $E_{th} \sim 5.0 \times 10^8 \text{ V/m}$ with the constants from the literature. These are comparable to the estimates from the atomistic simulations of $\Delta F_{acti}^{MD} \sim 255 \text{ mJ/m}^2$ and $\Delta F_{acti}^{DFT} \sim 150 \text{ mJ/m}^2$ for Y-wall, and $\Delta F_{acti}^{MD} \sim 115 \text{ mJ/m}^2$ for X_I -wall and 140 mJ/m^2 for X_{II} -wall and $\Delta F_{acti}^{DFT} \sim 30 \text{ mJ/m}^2$ for an average value of two X-walls. Because P_z yields essentially the same domain wall width for all three domain walls, the threshold fields are similar. However, the normal and parallel polarization contributions are different in each case, which could have a significant effect on the threshold field. In the absence of a theory of these non-uniaxial polarizations for the trigonal structure, we cannot estimate their effect, however. Thus further development of the model for the non-uniaxial component of polarization is necessary to improve the GLD phenomenological analysis.

4.8 Conclusions and Discussion

The structure and energetics of domain walls in LiNbO_3 has been studied by empirical potentials and verified by DFT. The Y-wall is energetically favored but should be less mobile because the activation energy for migration is higher. The broken symmetries of both cations and anions near the wall lead to non-uniaxial polarizations. This expands the characteristics of ferroelectric domain wall from simple Ising-type to include Bloch-like and Néel-like type components. The fits to the GLD formalism of uniaxial polarization profiles of different domain walls lead to very similar domain wall widths. Although the absolute value of the in-plane polarization is small, less than 3% of

uniaxial polarization, the in-plane polarization has an important role for understanding ferroelectric domain wall behavior in LiNbO_3 . Moreover, since other material systems also appear to show such in-plane wall components, [135] it is possible that mixed Bloch-like and Néel-like character to ferroelectric walls may be ubiquitous. These non-uniaxial polarization components can change the relative electrostatic energies of different wall orientations, and can explain why some wall orientations are seen and others not. [96]

CHAPTER 5 DOMAIN WALL-DEFECT INTERACTIONS IN FERROELECTRIC LITHIUM NIOBATE

5.1 Introduction

This chapter focuses on the interaction between defects and domain walls in LiNbO_3 and their effect on domain dynamics. The effect of the type and charge state of a defect or defect pair on domain wall pinning is determined.

5.2 Methodology and Validation

5.2.1 Empirical Study with Two Different Methods

There are two widely used methods available to describe the defect formation energies (DFEs) of charged defects: the supercell[144] method and the Mott-Littleton (ML) method[145].

Supercell method: The imposition of periodic boundaries in the supercell method intrinsically involves defect-defect interactions, and thus corresponds to a high concentration of defects. Because the supercell method is simply the extension of a bulk calculation, it can be calculated by:

$$\Delta E_f = E^{total}(\text{defective}) - E^{total}(\text{perfect}) \quad (5-1)$$

ML method: The ML method embeds a single defect into an atomistic region which, in turn, is embedded in a dielectric continuum. It thus corresponds to the infinite dilute limit of defects. DFEs are obtained from the ML method by dividing the surroundings into two different regions; region 1 and region 2a, see figure 5-1. Atoms outside of the regions belong to region 2b. The ions in region 1 are assumed to be strongly perturbed by defects and therefore are relaxed in an explicitly atomistic manner. In contrast, the ions in region 2 are assumed to be weakly perturbed and therefore its relaxation is performed in an approximate way.

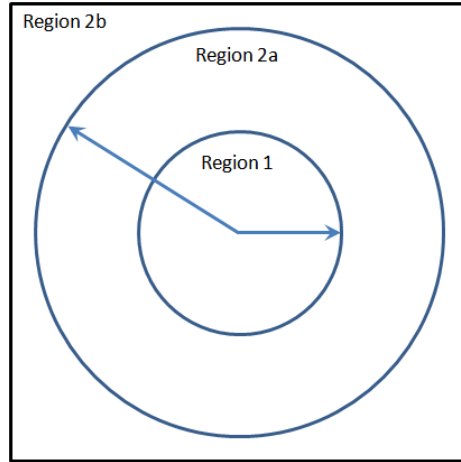


Figure 5-1 Three different regions divided by mott-littleton (ML) method

Normally, both the radius of region 1 and the difference of the radii of regions 1 and 2 should be greater than the short range potential cutoff distance to achieve convergence of ML method. The ML method considers the total energy of the two region system as the sum of contributions of energies of each region and between them:

$$E^{total}(x, \xi) = E_{11}(x) + E_{12}(x, \xi) + E_{22}(\xi) \quad (5-2)$$

where $E_{11}(x)$ represents the energy of region 1 as a function of the Cartesian coordinates, x , $E_{22}(\xi)$ represents the energy of region 2 as a function of the displacements, ξ , and $E_{12}(x, \xi)$ is the energy of interaction between the two regions. For the ML method, the DFE is calculated by the combination of equations (5-1) and (5-2).

Table 5-1 shows the comparison of DFEs of intrinsic defects between supercell and ML methods. One interstitial site, the empty center of oxygen octahedron, is used for formation energy calculation of interstitial defects. As we can see from Table 5-1, two different methods yield small difference in the calculated DFEs. The difference in DFEs between our calculation and literature for ML method results from the difference in the size of region 1 and 2.

Table 5-1. DFEs calculated by various methods. The interstitials are places at the center of an empty oxygen cage.

	Supercell (This study)	Mott-Littleton (This study)	Mott-Littleton[79]
Li_i^\bullet	-7.64	-7.09	-7.08
$Nb_i^{\bullet\bullet\bullet\bullet}$	-107.61	-106.51	-104.12
O_i''	-12.64	-11.41	-9.47
V_{Li}'	9.73	9.85	9.81
V_{Nb}''''	122.40	125.32	127.56
V_O''	18.01	19.26	18.98
$Nb_{Li}^{\bullet\bullet\bullet}$	-102.69	-102.45	-98.37

5.2.2 DFT with Thermodynamic Frame Works

The DFE of a defect or defects, denoted as α , with charge state q is defined as[146]

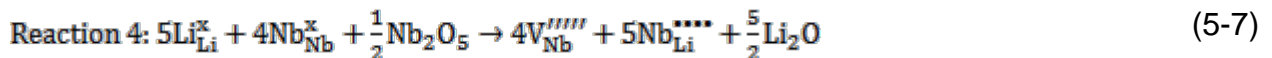
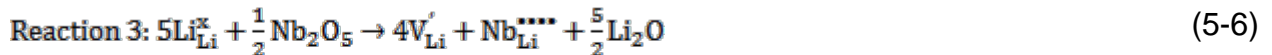
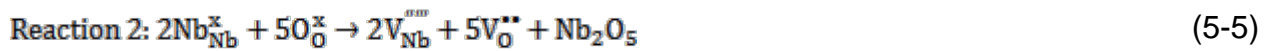
$$\Delta E_f(\alpha, q, T, P) = E^{total}(\alpha, q) - E^{total}(perfect) + \sum_i n_i \mu_i + q(\varepsilon_F + E_v + \Delta V) \quad (5-3)$$

where $E^{total}(\alpha, q)$ is the total energy obtained from DFT calculation of a supercell with the defect(s); $E^{total}(perfect)$ is the total energy of the supercell without any defects. n_i is the number of atoms of species i that have been added to ($n_i > 0$) or removed from ($n_i < 0$) the supercell when the defects are created; μ_i is the chemical potential of element i . T is temperature and P is the oxygen partial pressure. ε_F is the Fermi energy with respect to the valence band maximum in the bulk single crystal. E_v is the valence band maximum of the bulk single crystal system. Therefore, as discussed by Van de Walle and Neugebauer[146], a correction term ΔV , which is the difference in the electrostatic potentials of the defected and un-defected systems, is needed to align the band structures.

Strictly speaking, the free energy rather than the total energy should be used in equation (5-3) for the calculation of the DFEs. The total internal energies of a supercell obtained from DFT calculations correspond to the Helmholtz free energy at zero temperature, neglecting zero-point vibrations.[147] These calculations thus neglect the contributions from the vibrational entropy; fortunately, experimental and theoretical results for entropies of point defects typically fall between 0 to $10k$ (0 to 0.26 eV at 300 K), where k is the Boltzmann constant [146]. As a consequence, we do not expect this neglect of the entropy term to qualitatively change our conclusions. Detailed analyses by He *et al.* [148] and Kohan *et al.* [149] also concluded that entropic effects can be neglected.

5.2.3 Comparison of DFEs of Neutral Defect Complexes

Charge neutrality requires neutral defect complexes be compared. Here we consider four possible simple defect pairs which maintain the stoichiometry of the LiNbO_3 materials: Li Frenkel, Nb Frenkel, O Frenkel pair, and LiNbO_3 Schottky complex. However, stoichiometric defect clusters cannot account for the Li deficiency of congruent LiNbO_3 . Thus, four additional defect complexes which produce non-stoichiometry are also considered: Li_2O pseudo-Schottky, Nb_2O_5 pseudo-schottky, $\text{Nb}_{\text{Li}}^{\bullet\bullet\bullet\bullet} + 4V_{\text{Li}}'$ (Antisite_I) and $5\text{Nb}_{\text{Li}}^{\bullet\bullet\bullet\bullet} + 4V_{\text{Nb}}^{\bullet\bullet\bullet\bullet}$ (Antisite_{II}). The purpose of this comparison is to determine the most energetically favorable defect structures. The defect reactions for these complexes are:



For further calculations, three different oxide states, LiNbO_3 , Li_2O and Nb_2O_5 are considered for the reactions. Nb_2O_5 has several different structures including T- Nb_2O_5 (Pbam) and B- Nb_2O_5 (C2/c) at high-pressure[150] and H- Nb_2O_5 (P2/m) at high temperatures ($T > 1100^\circ\text{C}$) [151], metastable R- Nb_2O_5 (C2/m), P- Nb_2O_5 (I4₁22), N- Nb_2O_5 (C2/m) and M- Nb_2O_5 (I4/mmm). For this study, M- Nb_2O_5 phase is chosen because of its simplicity on crystal structure. Table 5-2 shows structures and the lattice energies of these reference oxides. The small differences between our calculations and previously published results [79] arise from minor differences in the method of calculating the electrostatic energy.

Table 5-2. Lattice energy (eV) per unit formula of oxides for empirical study and DFT

	Space group	Empirical		DFT
		This work	Reference [79]	
Li_2O	Fm$\bar{3}$m	-33.15	-33.16	-14.461
M- Nb_2O_5	I4/mmm	-314.15	-314.37	-60.319
LiNbO_3	R3c	-174.95	-174.57	-39.552

figure 5-2 compares the DFEs of stoichiometric and non-stoichiometric defect complexes. The Li Frenkel and Antisite_i pair are the most energetically favorable for both the Li rich condition and Li deficient conditions. For the empirical potentials, it is possible to determine which are the energetically favorable defect complexes by comparing formation energies. A previous study using the ML method concluded that Li Frenkel and Antisite_i clusters are the most energetically favored among the stoichiometric and non-stoichiometric defects. This is consistent with the DFT result.

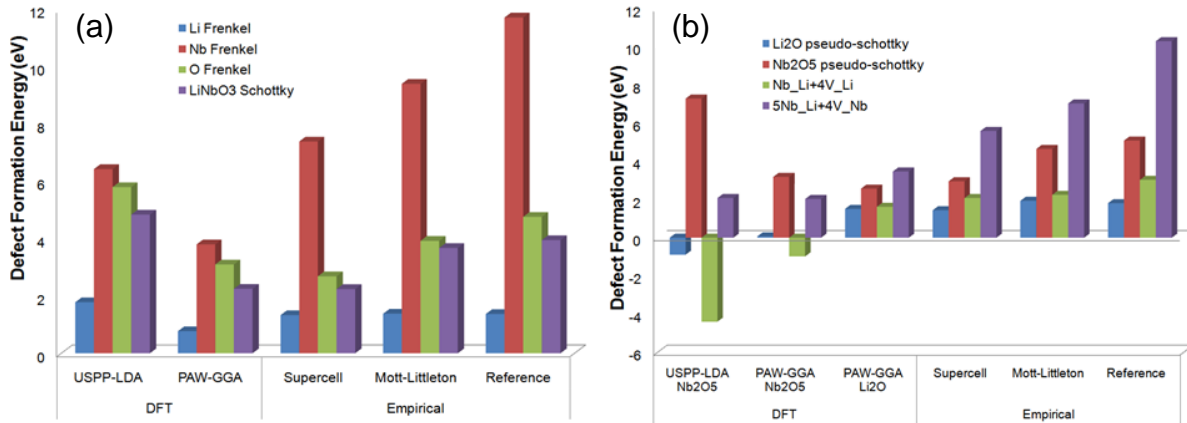


Figure 5-2. DFE comparison of (a) stoichiometric and (b) non-stoichiometric defect pairs in LiNbO_3 using DFT and empirical method. For non-stoichiometric defect pairs, two different reference states, Nb_2O_5 and Li_2O can lead two variants of DFT results. For empirical study, it is not possible to identify different reference state. However, different empirical studies consistently yield same order in DFE with DFT results of Li_2O reference state.

The supercell method also leads to similar results, see figure 5-2. Although the precise DFEs calculated by the supercell and ML methods do not match exactly, both yield the same trends for DFEs. In this study, we will mainly focus on Li Frenkel and Antisite_i defect pairs using the supercell method for DFE calculations.

5.3 Configurations of Two Different Intrinsic Defect Pairs

5.3.1 Li Frenkel Pair ($\text{Li}_i^+ + \text{V}_{Li}^-$)

Figures 5-3(a) and (b) show two possible structural arrangements of Li Frenkel defect pair. The two structures show similar stacking sequences as either two vacancies sit below and two Li ions sit above the center Nb ion (figure 5-3 (a)) or vice versa (figure 5-3 (b)). Thus in both cases the cation stacking sequence is Nb-V-V-Nb-Li-Li rather than Nb-V-Li-Nb-V-Li as in perfect crystal. The differences between the polarization generated by the defect pair (P_d) and the spontaneous polarization (P_s) leads to the difference in energy. The configuration in figure 5-3(a) creates P_d parallel to P_s , Li_{F-Para} while the configuration in figure 5-3(b) generate P_d antiparallel to P_s , Li_{F-Anti} .

We also considered the unbounded state at which each Li_i^\bullet and V_{Li}' defect exists as an individual point defect without an association effect.

The empirical study predicts that the parallel configuration of Li Frenkel (Li_{F-Para}) is energetically more stable state than antiparallel (Li_{F-Anti}) or unbound configuration of the Li Frenkel pair. The association energy is obtained by the difference in energy of arranged defect pairs from non-paired (unbounded) defects. The association energy of the parallel Frenkel pair ($E_{Asso, Li_{F-Para}} \sim -0.24$ eV) is lower than the association energy of the antiparallel ($E_{Asso, Li_{F-Anti}} \sim -0.02$ eV) or unbounded Frenkel pair ($E_{Asso, unbound} \sim 0$ eV). Figure 5-3(b) shows the comparison of calculated association energies of different Li Frenkel configurations using empirical methods.

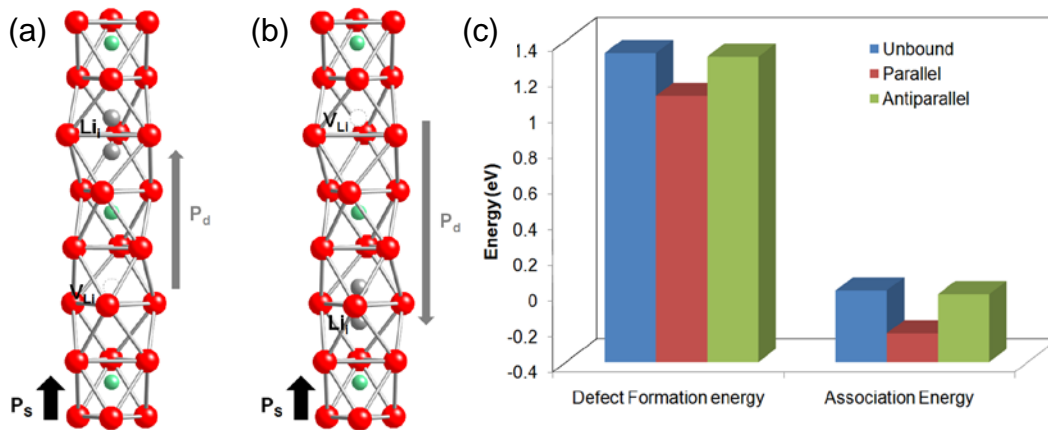


Figure 5-3. Two different configurations of Li Frenkel pair: The polarization created by defect pair (P_d) is (a) parallel and (b) antiparallel to spontaneous polarization (P_s). (c) The comparison on defect formation energies of different Li Frenkel configurations using empirical method. Supercell methods expect parallel configuration is energetically favorable than antiparallel configuration.

5.3.2 Nb antisite Pair($Nb_{Li}^{\bullet\bullet\bullet\bullet} + 4V_{Li}'$)

The Nb antisite cluster ($Nb_{Li}^{\bullet\bullet\bullet\bullet} + 4V_{Li}'$) is another defect pair which can be found under Li poor conditions. The configuration of $Nb_{Li}^{\bullet\bullet\bullet\bullet} + 4V_{Li}'$ defect pair has previously been proposed by Kim *et al.* [152]. They suggested that the lowest energy configuration of the

defect pair will show a tetrahedral shape (Figs. 5-4a and 5-4b), since non uniaxial dipole moments created by defect pair may generate non trivial energy (Figs. 5-4c though 5-4e). They also distinguished two different tetrahedral configurations depending on the direction of tetrahedron from spontaneous polarization (P_s). They concluded that the upside down tetrahedral configuration which yields a dipole moment to the bulk polarization (figure 5-4a) is energetically more favorable than the upside configuration yielding antiparallel dipole moment (figure 5-4b), because a dipole moment of Nb antisite pair is created from tetrahedron top to basal plane.

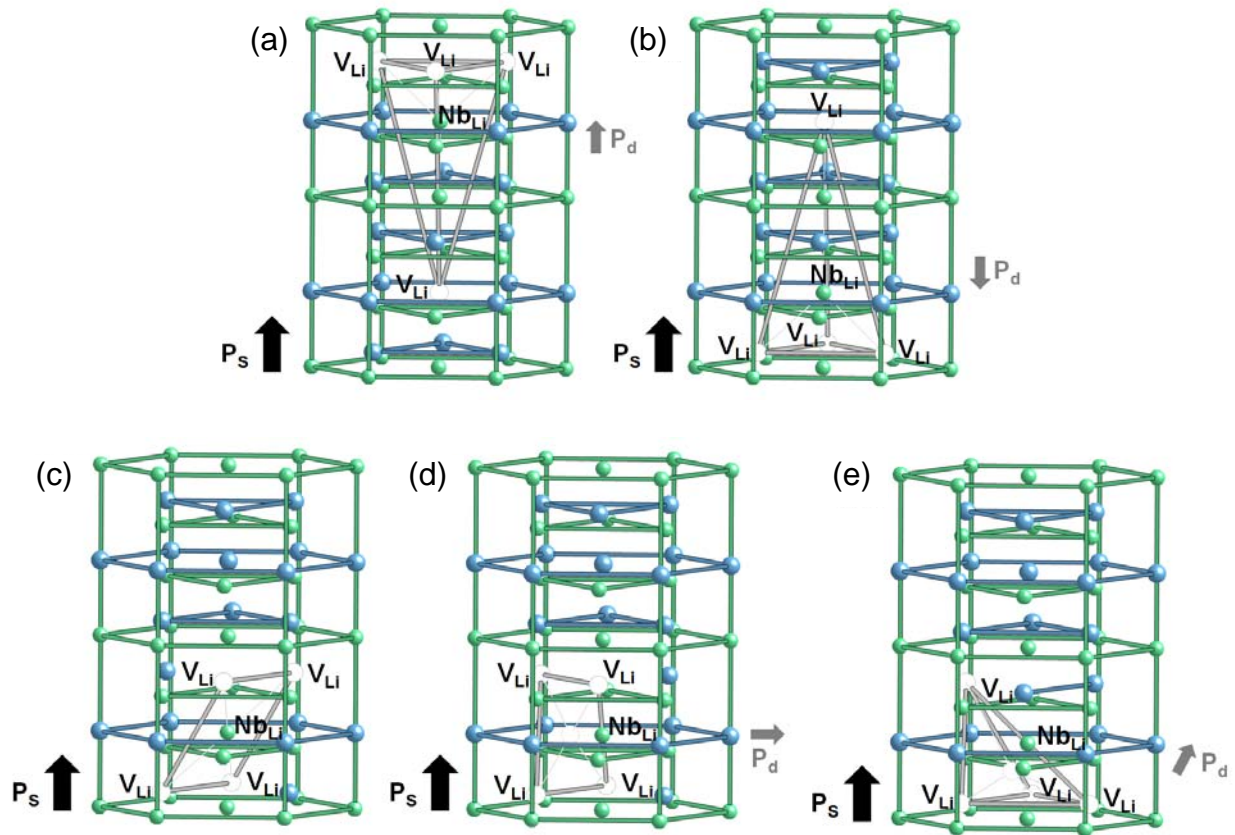


Figure 5-4. Different structural arrangements of Nb antisite defect pair. Net dipole moment of defect pair (P_d) are (a) parallel to bulk polarization (b) antiparallel to bulk polarization (c) none (d) perpendicular to bulk polarization (e) leaned parallel to bulk polarization. The linear lines are the guidance for the centroid of 4 lithium vacancies.

However, a recent DFT study [78] shows that the formation energy of Nb antisite pair can be lower when all four lithium vacancies are sitting at the nearest Li ion site from the antisite (See, Figs. 5-4c through 5-3e). Also, the DFT study shows that the difference in DFEs among different configurations of four Li vacancies is only 0.11 eV, thus different configurations do not lead major difference in defect energetics of Nb antisite pair. Finally, the study concludes that most of the configurations are energetically favorable, so that several arrangements will coexist inside the congruent LiNbO₃ material.

An empirical study with different arrangements of the Nb antisite, shown in figure 5-5, was performed to verify the capability of describing DFE of different configurations of Nb antisite pair. The DFE of the Nb antisite was calculated from:

$$DFE = 4E(V_{Nb}^{''''}) + 5E(Nb_{Li}^{''''}) + \frac{5}{2}E(Li_2O) - \frac{1}{2}E(Nb_2O_5) \quad (5-8)$$

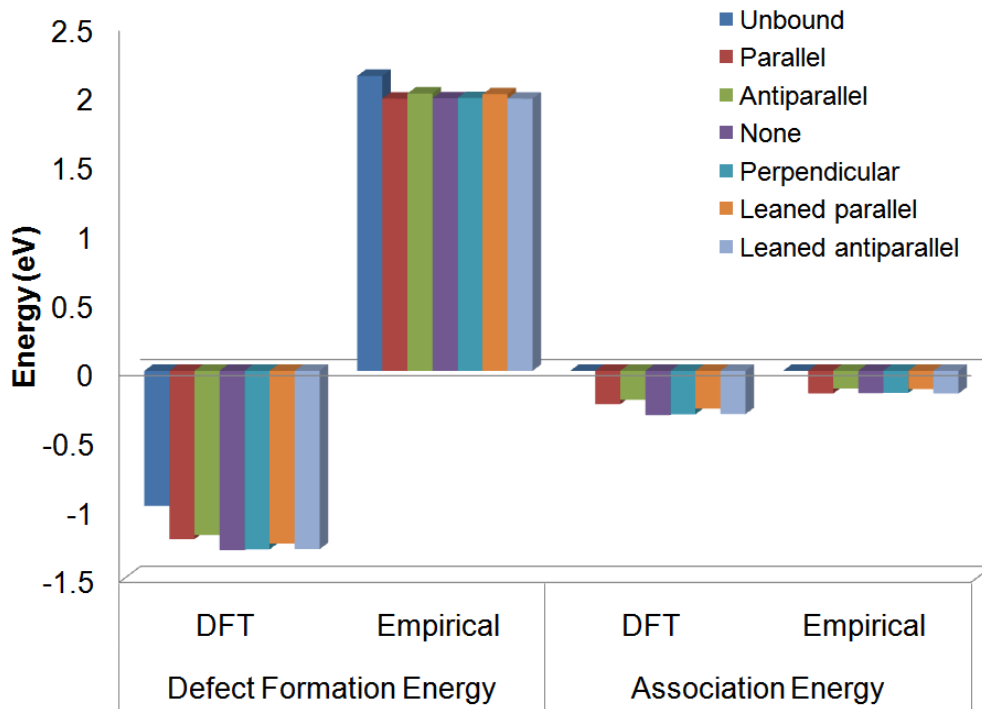


Figure 5-5. The comparison of DFE and association energy of different configurations of Antisite, defect pair using DFT and empirical methods.

The lattice energies of antiferroite Li_2O (-33.15 eV) and tetragonal Nb_2O_5 (-314.15 eV) was determined, see Table 5-2. Figure 5-5 compares the DFEs determined from the DFT and empirical calculations. Consistent with DFT study, the empirical study also didn't show major differences in DFE between different arrangements of Nb antisite pair. Also, Nb antisite pair does not show any preference on the direction of dipole moment with respect to the direction of bulk polarization. The range of association energy between different configurations is from -0.127 eV to -0.165 eV. However, the empirical study predicts positive DFEs for all configurations while DFT predicted negative values. The positive DFEs of empirical study represent that no defect configurations are favorable to form the Nb antisites in nature. This difference originates from the different reference states; DFT consider the reference state as Li deficient condition while the empirical study just predicts them at stoichiometric condition. Since we are considering Nb antisites at congruent condition, we focus on the relative differences in DFEs of empirical study to reduce the error come from the different reference state. Although the DFT and empirical calculations are not directly comparable due to the very different reference states, both methods conclude that most of the configurations are equally likely because of the small differences in formation energy.

5.4 Domain Wall-intrinsic Defect Interactions

We now turn to the main thrust of this study: the interaction of domain walls with intrinsic defects. We consider two domain wall structures: parallel to c-glide plane (*Y-wall*) and perpendicular to c-glide plane (*X-wall*). We place individual defects or defect clusters at various distances from domain wall structures, which have been previously equilibrated at constant volume. The energetics of the defect/domain wall interactions are then determined. The interaction between the defects and the domain wall means

that their energies cannot be uniquely separated from each other. Here we ascribe the change in the energy of the system to a change in the defect formation energy; we could, with equal merit, ascribe this energy change to a change in the domain wall energy.

5.4.1 Y-wall with Individual Point Defects

We have determined the energetics of V_{Li}' , Li_i^\bullet , and Nb_{Li}^{****} as a function of distance from the domain walls. As figure 5-6 (a) shows, the energy of each of these defects decreases as they approach the Y wall. In particular, the energies of the V_{Li}' , Li_i^\bullet , and Nb_{Li}^{****} defects are 0.23 eV, 0.53 eV and 0.66 eV lower at the domain wall than in the bulk. The effect of the *Y-wall* decreases rapidly as the separation increase, essentially disappearing about 6.5Å away. Chapter 4 showed that the Y-domain wall can break the symmetry of cations and leads to two inequivalent cation positions. Therefore, we performed DFE calculation of Li_i^\bullet in both sites I and II, see figure 5-6(b). As figure 5-6(a) shows there is only a small energy difference, 0.01 eV, for the DFE of Li_i^\bullet at the two nonsymmetric positions. Thus, although Sites I and II are structurally distinct, they show very similar energetics.

As fiducial systems to validate the calculations with the empirical potentials, we have also performed a DFT study on a smaller system size. The DFT calculations involve neutral defects; thus these values cannot be compared directly to the values for charged defects from empirical study. The variation of formation energies determined by DFT are $V_{Li}^x = 0.11$ eV, $Li_i^x = 0.12$ eV and $Nb_{Li}^x = 0.14$ eV. Both methods predict that the interaction between a point defect and *Y-wall* can lower DFEs of point defects. A similar effect has previous been seen in a study on interaction between an oxygen vacancy and a domain wall in $PbTiO_3$. [153]

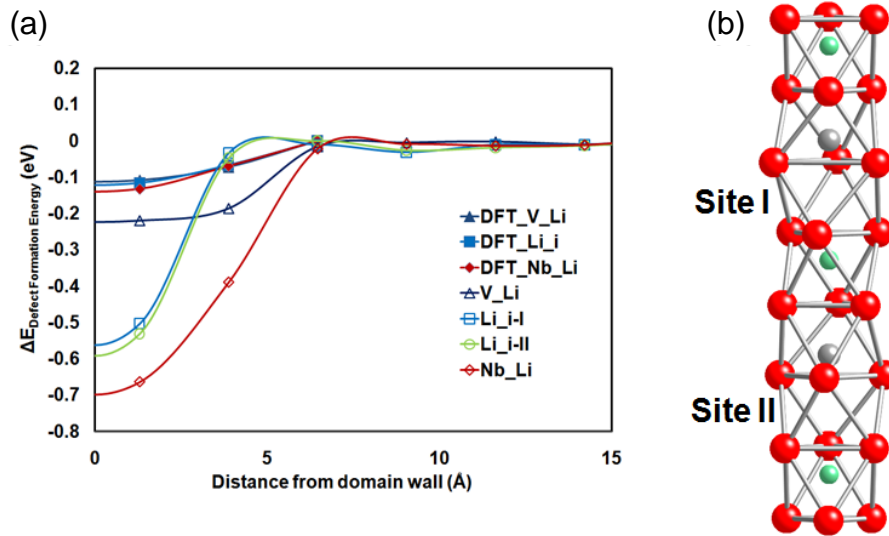


Figure 5-6. The change in DFE of single point defects near Y-wall. (a) The variation in DFE of the most dominant single defects in LNO near Y-wall is plotted as a function of distance from the domain walls. (b) Two different interstitial sites caused by broken symmetry of oxygen near the Y-wall. For Li interstitial defect, two different symmetric sites, site I and site II are considered for the site dependence of DFE near Y-wall. The qualitative agreement between the DFT and atomistic calculations provides confidence to move forward with the determination of the energetics of other defects structures.

5.4.2 Y-wall with Li Frenkel Pair

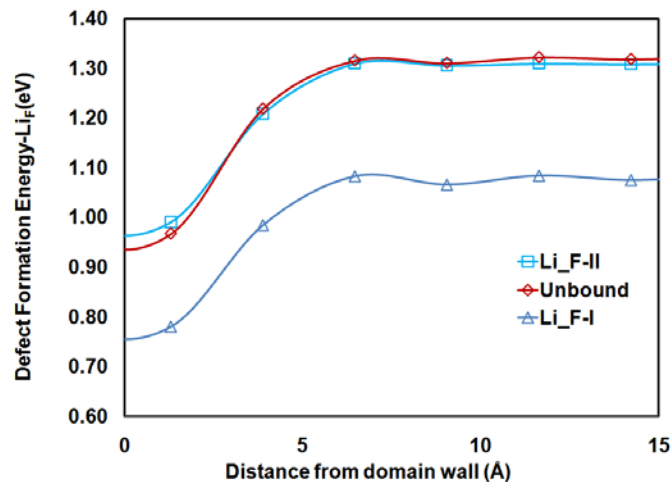


Figure 5-7. Comparison on DEFs of Li Frenkel pair in two different configurations; parallel to bulk polarization (Li_{F-Para}), antiparallel to bulk polarization (Li_{F-Anti}). Unbound state of Li Frenkel pair is also considered for the comparison.

Figure 5-7 shows the variation of the formation energy of two different configurations of Li Frenkel pairs and unpaired state of two defects (unbound) near the *Y-wall* using empirical methods. Two different configurations, P_d parallel to P_s and P_d antiparallel to P_s are considered in order to characterize the effect of structural arrangement of Li Frenkel pairs near *Y-wall*. As we can see from the figure 5-7, the variation of formation energies between unbounded and bounded Li Frenkel pair shows a similar pattern near the *Y-wall* by lowering the formation energy (0.35 eV for Li_{F-Para} , 0.32 eV for Li_{F-Anti} and 0.36 eV for unbound) from the bulk state. The difference in DFEs between Li_{F-Para} and Li_{F-Anti} increases from 0.22 eV in the bulk to 0.25 eV near the *Y-wall*. The interaction between the *Y-wall* and Li Frenkel pair disappears at 6.46Å away from the *Y-wall*.

5.4.3 *Y-wall* with Antisite₁ ($Nb_{Li}^{\bullet\bullet\bullet} + 4V_{Li}'$)

Because the various configurations do not show much difference in energetics near the *Y-wall*, we only consider two tetrahedral arrangements Figs. 5-4(a) and 5-4(b) among the various configurations of the Antisite₁ cluster.

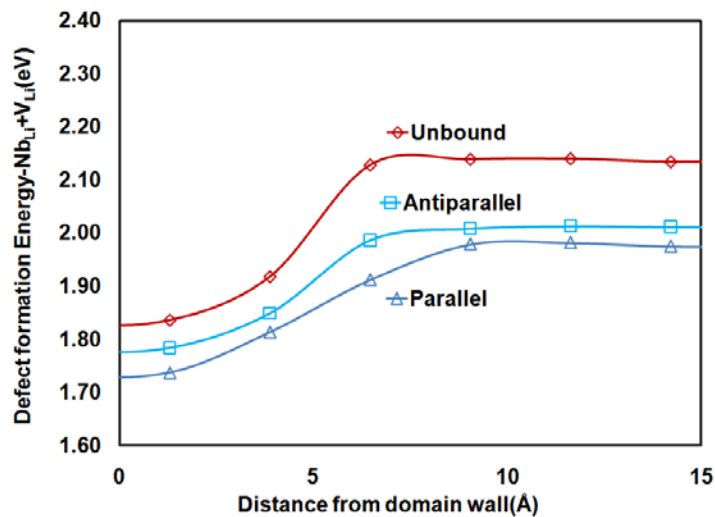


Figure 5-8. Formation energies of Antisite₁ clusters as a distance from a *Y*-domain wall.

In the first, one of the three sides of basal triangle is parallel to *Y-wall*, which creates a uniaxial component of the dipole moment. Figure 5-8 shows the variation of DFE as a function of distance from *Y-wall*. As in the case of the Li Frenkel pair, the Antisite_i cluster has a lower energy at the *Y-wall* by 0.30eV for unbounded and 0.24 eV for parallel and 0.23 eV for antiparallel. This does not change their relative order, with parallel configuration having the lowest energy.

5.4.4 X-walls with Point Defects

Chapter 4 indicates that the *X-walls*, perpendicular to c-glide plane, display two different variants, *X_I-wall* and *X_{II}-wall*, depending on the in-plane polarization states near the domain walls. In this section, therefore, the two *X-wall* variants are considered for the interaction with defect clusters. As in the case of the *Y-wall*, we initially perform the DFE calculations with three point defects near two *X-walls* using DFT and empirical method. Both methods predict DFEs are lowered near both *X_I-wall* and *X_{II}-walls*. However, each *X-wall* show different pattern for interacting with single defects. Again, DFT calculation predicts DFEs of neutral charged defects, so the value cannot be compared directly with DFEs in the empirical study.

When determined with the empirical potential, the largest change in the DFE is observed for the Nb_{Li}^{***} which lowers ~ 1.45 eV for the *X_I-wall* and ~ 0.77 eV for *X_{II}-wall* from the bulk value of -102.69 eV. Li_i^{\bullet} shows smaller changes: ~ 0.71 eV for *X_I-wall* and ~ 0.63 eV for *X_{II}-wall* from the bulk value of -7.64 eV. The smallest domain wall/defect interaction is V_{Li}' as ~ 0.16 eV for both *X_I-wall* and *X_{II}-wall* from the bulk value of 9.73 eV. We also perform DFT study to see the variation in DFEs near the *X-walls*. For DFT study, neutral defects are considered by adding or removing neutral atom for the simplicity of calculation. Thus, the change in DFEs near the *X_I-wall* and *X_{II}-wall* are

smaller than in the empirical study. The largest decrease is for Li_i^x with 0.27 eV for X_I -wall and 0.32 eV for X_{II} -wall from the bulk value of -2.76 eV. V_{Li}^x shows a smaller variation of 0.14 eV for the X_I -wall and 0.18 eV for the X_{II} -wall from the bulk value of 2.14 eV. Nb_{Li}^x shows the lowest variation, 0.11 eV for the X_I -wall and 0.14 eV for the X_{II} -wall from the bulk value of -6.06 eV. In contrast to the empirical study, no significant difference in the variation of DFEs at both the X_I -wall and the X_{II} -wall are observed from the DFT study with neutral defects. Although the DFEs of two different methods cannot be compared directly, the domain wall-defect interactions lead to decrease in the formation energy of defects regardless of their charge state. Also, we can predict that higher charged state of Nb_{Li}^{***} may cause the higher interaction with domain walls. Comparing these values with those from the Y-wall, the X-walls show a stronger interaction with defects.

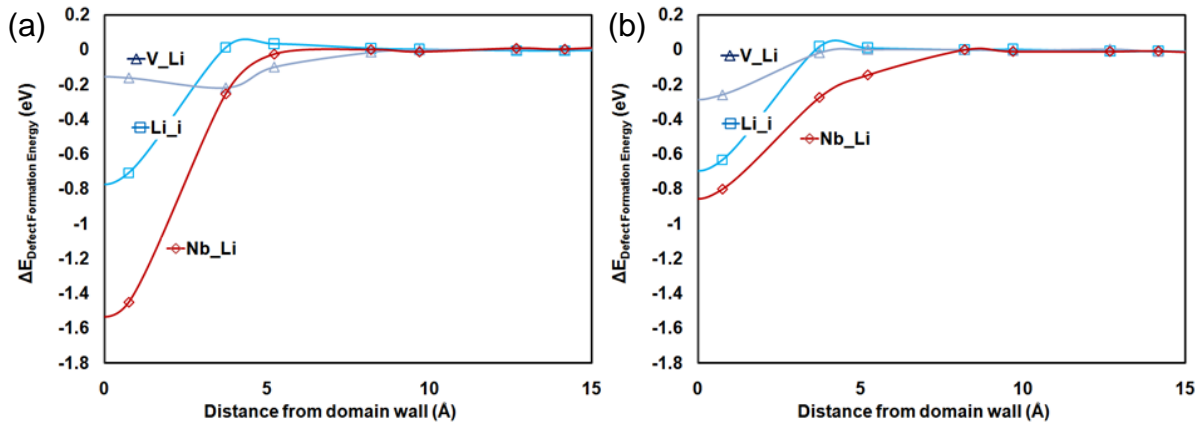


Figure 5-9. Variation of DFE of point defects near (a) X_I -wall (b) X_{II} -wall

5.4.5 X-walls with Li Frenkel Pair

We calculate the DFEs of two different Li Frenkel configurations, parallel and antiparallel near the two X -wall variants. The variations of DFE of Li Frenkel pairs as a function of the distance from X-walls are shown on figure 5-10. The DFE of the X_I -wall

decreases by 0.30 eV for Li_{F-Para} and 0.32 eV of DFE of Li_{F-Anti} . The X_{II} -wall shows a slightly higher interaction, with the DFE of Li_{F-Para} lowered by 0.34 eV and the DFE of Li_{F-Anti} lowered by 0.36 eV. Thus, both of X -walls decrease the formation energies of the Li Frenkels by almost one third from the bulk values. As figure 5-10 shows, the consistent variation between different configurations explains that Li_{F-Para} is always the lowest energy configuration regardless of domain wall-defect interactions.

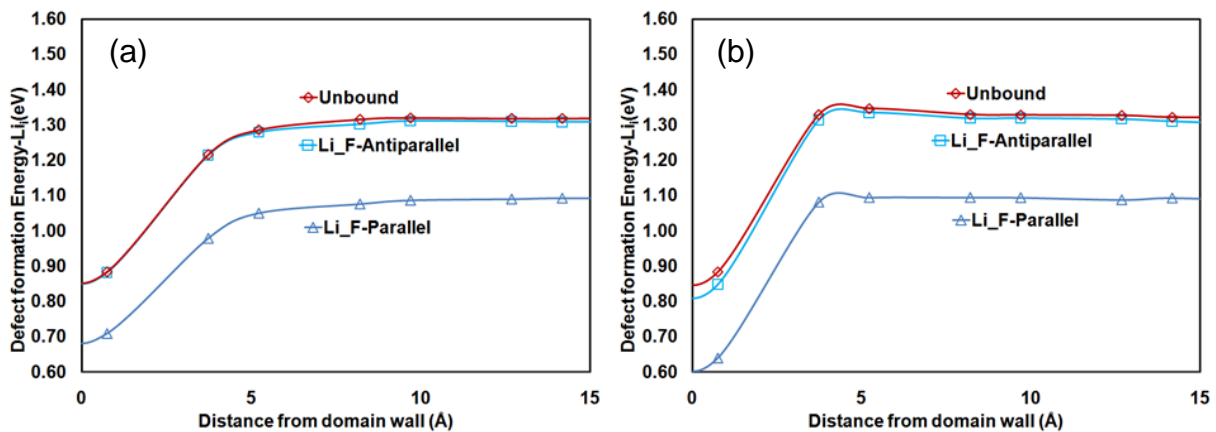


Figure 5-10. DFE of Li Frenkel defect pair near (a) X_I -wall (b) X_{II} -wall

5.4.6 Two X -walls with Antisite_I Pair

The two X -walls also lead to two variants of DFE for the Antisite_I clusters, see Figs. 5-4(a) and 5-4(b). For the parallel state, the DFEs of Antisite_I defects are lowered by 0.36 eV for X_I -wall and by 0.29 eV for X_{II} -wall at the nearest plane, 1.3 Å away from the X -walls. Similarly, the DFE of the antiparallel state are lowered by 0.32 eV for X_I -wall and 0.25 eV for X_{II} -wall. The parallel configuration shows a slightly lower energy (0.07 eV for near X_I -wall and 0.08 eV for X_{II} -wall) than antiparallel configuration at the nearest plane. An interesting phenomenon is observed at 4.5 Å away from the X_{II} -wall. The DFEs between parallel and antiparallel are switched near X_{II} -wall. This result indicates the possible rearrangement of the defect cluster from a frustrated mode to stable

configuration during the domain wall motion, an effect previously discussed by Gopalan *et al.*[80].

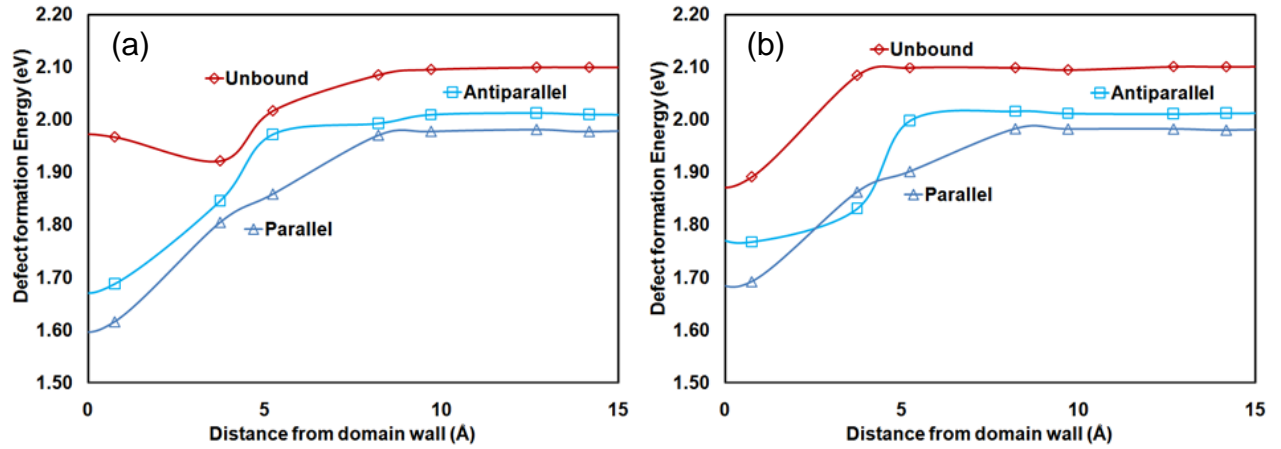
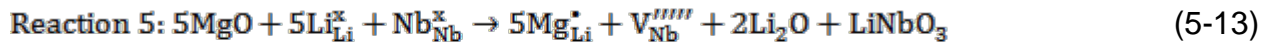
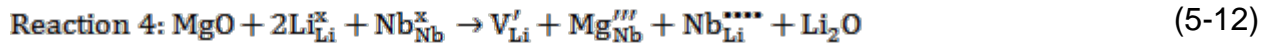
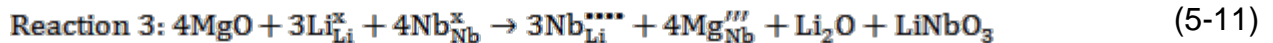
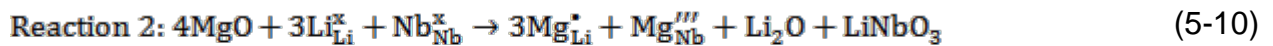


Figure 5-11. DFE of Nb antisite defect pair near (a) X_I -wall (b) X_{II} -wall

5.5 Extrinsic Defect, Mg

5.5.1 Reaction Schemes with Mg Dopants

Donnerberg *et al.*[154] demonstrated that cation sites are energetically more favorable than interstitial sites for dopants. A recent DFT study[155] also considered Er dopants as substitutional forms. A previous experimental study[156] on Mg dopants in LiNbO_3 shows that most of Mg dopants stays as a substitutional form instead of interstitial. Therefore, we consider five different reactions, each of which maintains the charge neutrality of the system.



The energy associated with each reaction is obtained from the formation energy of the products less the formation energies of reactants. Therefore, the formation energy for each reaction can be shown as below:

$$DFE_1 = E(Mg_{Li}^{\bullet}) + E(V_{Li}') + E(Li_2O) - E(MgO) \quad (5-14)$$

$$DFE_2 = 3E(Mg_{Li}^{\bullet}) + E(Mg_{Nb}''') + E(Li_2O) + E(LiNbO_3) - 4E(MgO) \quad (5-15)$$

$$DFE_3 = 3E(Nb_{Li}^{****}) + 4E(Mg_{Nb}''') + E(Li_2O) + E(LiNbO_3) - 4E(MgO) \quad (5-16)$$

$$DFE_4 = E(V_{Li}') + E(Mg_{Nb}''') + E(Nb_{Li}^{****}) + E(Li_2O) - E(MgO) \quad (5-17)$$

$$DFE_5 = 5E(Mg_{Li}^{\bullet}) + E(V_{Nb}''''') + 2E(Li_2O) + E(LiNbO_3) - 5E(MgO) \quad (5-18)$$

Before presenting the results for defect/domain wall interactions, we perform a study to reproduce the results for bulk defects using the potentials. Table 5-3 shows that the lattice energies of LiNbO₃, Li₂O and MgO: the very small difference between the results of our calculations using an in-house code and the published results with GULP arise from minor differences in the method of calculating the electrostatic energy.

Table 5-3. Lattice energy of oxides

	Space group	Lattice energy per unit formula (eV)	
		This work	Reference
MgO	Fm $\bar{3}$ m	-41.03	-41.04
Li ₂ O	Fm $\bar{3}$ m	-33.15	-33.16
LiNbO ₃	R3c	-174.95	-174.57

The previous calculations used the Mott-Littleton approach for calculating the DFEs. Because we focus on defect/domain wall interactions, it is more convenient for us to use a supercell method.

We initially perform the calculation of DFE of a single dopant defect in order to compare our result with previous calculation by Araujo *et al.*. Our lattice energy calculation predicts the formation energy of Mg dopant at different site as -15.47 eV for

Mg_{Li}^{\bullet} and 93.89 eV for Mg_{Nb}''' which is the similar value (-15.36 eV for Mg_{Li}^{\bullet} and 95.18 eV for Mg_{Nb}''') from previous Mott-Littleton calculation. Table 5-4 compares the DFEs of single dopant calculated with the two methods.

Table 5-4. DFE of isolated defects: comparison of bulk DFEs calculated with a supercell method and the Mott-Littleton method.

	Supercell (This study)	Mott-Littleton (This study)	Mott-Littleton[79]	
Mg_{Li}^{\bullet}	-15.47	-15.41	-15.36	
Mg_{Nb}'''	93.89	94.45	95.18	

Table 5-5 compares the formation energies of five different reactions. The differences between published and this study come from the different sizes for each region during the ML method. This study considers a large radius, 12 Å for region 1 and 2a for the convergence of the ML method. As we can see from the Table 5-5, the differences between supercell and ML method decrease with the large radius of each region.

Table 5-5. Energies for five reactions, calculated from the DFEs of isolated defects and the bulk lattice energies in Tables 5-2, 5-3 and 5-4.

	Supercell (This study)	Mott-Littleton (This study)	Mott-Littleton[79]	
Reaction 1	2.17	2.32	2.33	
Reaction 2	0.88	1.06	1.38	
Reaction 3	5.97	6.62	10.51	
Reaction 4	8.96	9.73	14.50	
Reaction 5	1.79	2.43	3.01	

Reactions 3 and 4 show relatively higher formation energy per dopant than other reactions. A previous experimental study suggests that the dominant defect configuration will change from reaction 1 at low concentration of dopant to reaction 1 and 5 at the intermediate dopant level to reaction 2 at the high defect concentration of

Mg dopant. Therefore, we only focus on reactions 1, 2 and 5 for the rest of the calculations.

5.5.2 Domain Wall-Mg Dopant Interactions

Now, we consider the interaction between a single Mg dopant and a Y-wall. To develop a basic understanding of defect-domain wall interactions, we focus on the Y-wall. The variation of formation energy of single Mg dopant occupying a Li site or a Nb site near Y-wall is shown at figure 5-12. The reference states are chosen as the DFE of each dopant at bulk state. As we can see from the empirical study, the formation energy of Mg dopant occupying the Li site increases in the vicinity of Y-wall; thus a single Mg dopant will not be trapped by domain wall at Li site. However, a Mg dopant occupying a Nb site has a lower formation energy near the Y-wall, and will thus be trapped by the domain wall.

Charge neutrality requires that there to be defects with compensating charges. The above results suggest that a low energy configuration would consist of Mg_{Nb}''' at the domain wall, with the Mg_{Li}^\bullet standing off from the domain wall by $\sim 5\text{\AA}$. However, the association effect between two Mg dopants also needs to be considered. If the association energy is larger than the energy caused by domain-wall/defect interaction, Mg_{Li}^\bullet can also sit near the Y-wall. Therefore, we performed the simulation, Mg_{Nb}''' at the domain wall, with Mg_{Li}^\bullet at varying distance in order to check how the association energy affect the configuration of Mg dopants near the domain wall.

The green line of the figure 5-12 shows the variation of DFE of the system in which Mg_{Li}^\bullet only varies its position with Mg_{Nb}''' at the Y-wall. The DFE at the reference state is chosen as the addition of DFE of bulk Mg_{Li}^\bullet and DFE of Mg_{Nb}''' at the Y-wall. Lowest defect formation energy is observed when Mg_{Li}^\bullet sit near the Y-wall. Thus, the association

energy between Mg_{Li}^{\bullet} and Mg_{Nb}''' is larger than the domain wall/Mg dopant interaction energy, -0.05 eV for Mg_{Li}^{\bullet} and 0.15 eV for Mg_{Nb}''' . As a result Mg dopants can be exist at both cation sites near the domain walls.

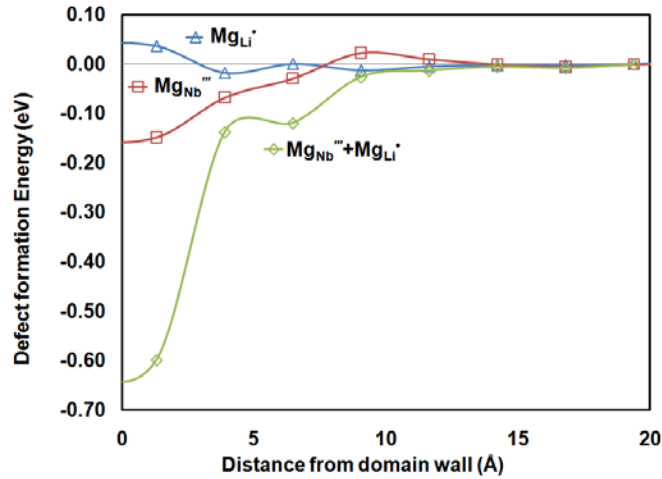


Figure 5-12. The variation of DFE of Mg dopant occupying cation sites near Y-wall. Positively charged Mg in the Li site show increase in DFE near Y-wall which indicate Mg at Li site will not be trapped by domain wall and less effect on domain wall motion and pinning effect. However, negatively charged Mg in the Nb site show the decrease in DFE as other intrinsic defect and defect pair and causing the pinning effect on domain wall motion.

For each reaction, we consider the defect as a different cluster shape in the $LiNbO_3$ system. The investigation of the association effect caused by different configuration of defect clusters shows the stable configuration of each defect pair near and far away from the Y-wall. For comparison, the unbounded state, in which each defect locates far apart as a single defect without any connectivity between components of defect pair, is also considered.

Reaction 1: Two different arrangements of Mg_{Li}^{\bullet} compensated by V_{Li}' can be distinguished depending on the direction between the dipole moment of the defect pair and the bulk polarization (P_s). Figure 5-13(a) shows the dipole moment of defect pair

parallel to bulk P_s ; figure 5-13(b) shows the case of the dipole moment antiparallel to bulk polarization.

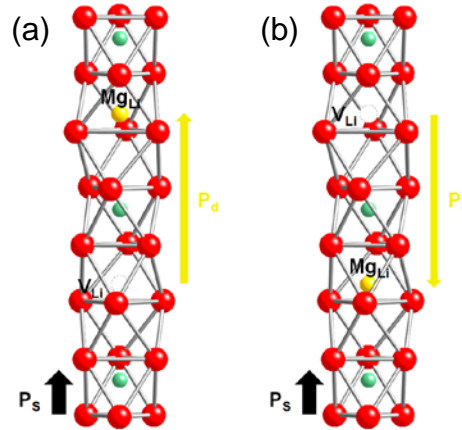


Figure 5-13. Possible arrangement for reaction 1. (a) dipole moment of defect pair parallel to bulk polarization (b) dipole moment of defect pair antiparallel to bulk polarization

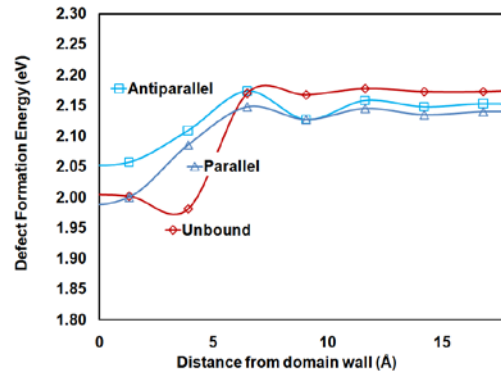


Figure 5-14. The variation of DFE of defect pair using reaction 1 near Y-wall. DFE is considered as formation energy per dopant.

Although single Mg_{Li} shows slightly higher formation energy near the Y-wall, the energy compensation by V_{Li} and association effect between two defects cause the Mg dopant to be trapped at the Li site near the Y-wall. The association energy for two different configurations are 0.03 eV for antiparallel and 0.04 eV for parallel. Thus, the parallel configuration is slightly more stable than antiparallel configuration. Also, the unbound defect state shows the lowest energy configuration around 4.5 Å away from

the Y-wall, which indicate the possibility of the rearrangement of defect pair. The rearrangement of defect configuration from frustrated mode to stable configuration during the domain wall motion has been discussed by Gopalan *et al.* [80]

Reaction 2: The arrangement of defect pair, Mg_{Nb}''' compensated by $3Mg_{Li}^\bullet$, can have multiple different arrangements. As we only consider the nearest Li sites from Mg_{Nb}''' , six possible Mg_{Li}^\bullet sites are shown in figure 5-15(a). Three Li sites among six different sites will be replaced by Mg_{Li}^\bullet while the rest will remain as Li ions. Although we consider the symmetry of the system, this will lead to six distinct configurations. Moreover, the broken symmetry near the domain wall will bring more complexity. In order to simplify the structural configurations, only two configurations: dipole moment parallel or antiparallel to bulk polarization are considered for this study, see figure 5-15(b) and (c).

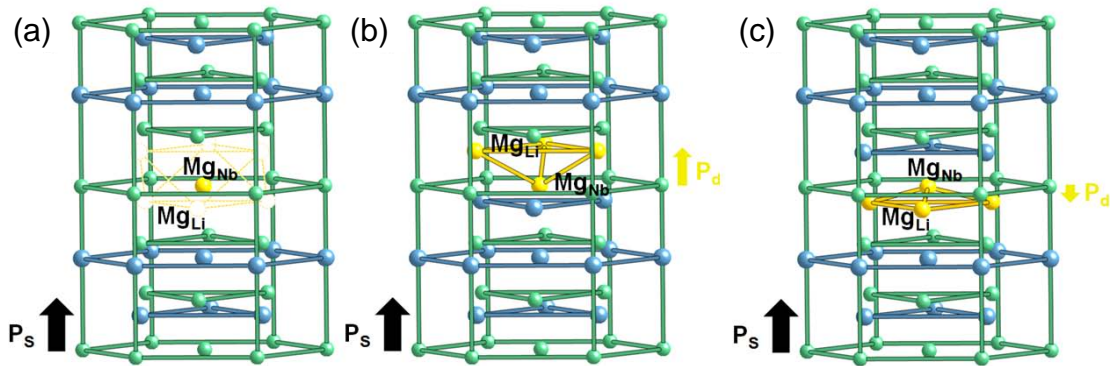


Figure 5-15. Possible arrangement of Mg dopants in LiNbO₃ for reaction 2. (a) the position of Mg_{Nb}''' and six possible nearest Li sites for the arrangement (b) possible arrangement for parallel dipole moment (c) possible arrangement for antiparallel dipole moment to bulk polarization

The variation of formation energy for Reaction 2 near Y-wall is shown on figure 5-16. The DFE per dopant predicts that antiparallel configuration is the most energetically stable arrangement in the bulk state. The association energies of different configurations are 0.27 eV for parallel and 0.42 eV for antiparallel configuration.

However, neither the unbound defect pair nor the antiparallel defect pair shows much interaction with the Y-wall. In particular, the formation energy for antiparallel configuration increases 0.04 eV near the Y-wall. By contrast, parallel configuration lowers by 0.13 eV of its formation energy. However, as we can see from the Fig 5-16, the most energetically favorable position for the defect pair, Mg_{Nb}''' compensated by $3Mg_{Li}^\bullet$, is at the bulk state with antiparallel configuration. Thus, we can predict Y-wall will show less behavior to trap the defect pair, Mg_{Nb}''' compensated by $3Mg_{Li}^\bullet$.

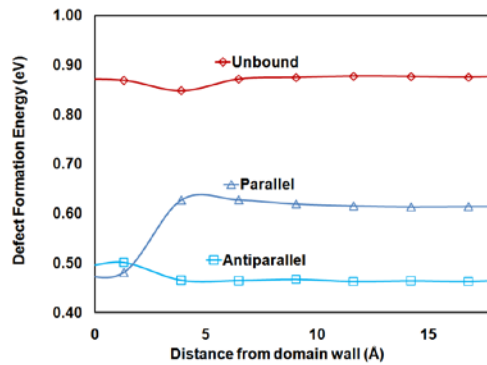


Figure 5-16. The variation of DFE of defect pair with reaction 2 near Y-wall. DFE is considered as formation energy per dopant.

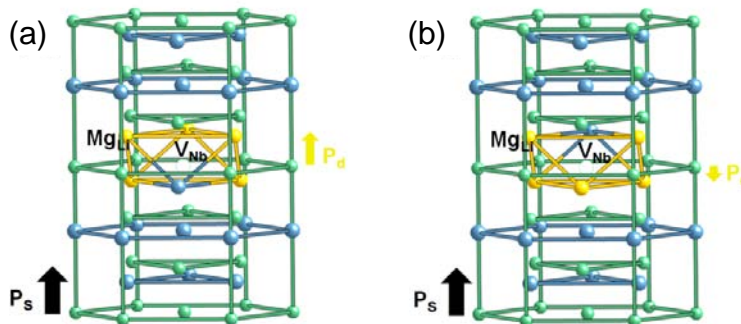


Figure 5-17. Possible arrangement of Mg dopants in $LiNbO_3$ for reaction scheme (5). Five Li sites out of six nearest Li sites from Nb vacancy will be occupied by Mg ion. (a) three Mg_{Li}^\bullet generate parallel dipole moment to bulk polarization and two Mg_{Li}^\bullet create antiparallel dipole moment to bulk polarization (b) two Mg ions at Li site generate antiparallel dipole moment and three Mg ions create parallel dipole moment.

Reaction 5: As we can see from the previous figure 5-15(a), the six nearest Li sites are available from one Nb site. By assuming Mg dopants occupy only the nearest Li sites of $V_{Nb}^{''''}$, two different arrangements of five Mg_{Li}^{\bullet} are possible in the bulk state. The two different arrangements can be understood in terms of their relationship to the bulk polarization: $3Mg_{Li}^{\bullet}$ sit above and $2Mg_{Li}^{\bullet}$ sit below the $V_{Nb}^{''''}$ or vice versa. Thus, for the case, in which the $3Mg_{Li}^{\bullet}$ is above the $V_{Nb}^{''''}$, the overall parallel dipole moments is parallel to the bulk polarization. figure5-17 shows schematic view of two possible configurations of reaction 5.

Figure 5-18 shows the comparison of DFE of different configurations for reaction 5. Although the parallel configuration shows a slightly lower DFE~ 0.06 eV in the bulk region, the interaction with Y-wall almost completely removes the preference on configuration for reaction 5. The association energies, 0.74 eV for parallel and 0.68 eV for antiparallel at bulk region change to 0.61 eV for both parallel and antiparallel in the vicinity of Y-wall.

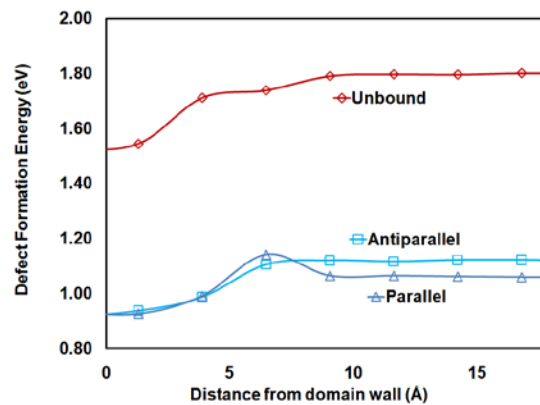


Figure 5-18. The variation of DFE of defect pair with reaction 5 near Y-wall.

5.6 Conclusion

Various point defects and defect pairs interact with domain walls in LiNbO_3 and lower the energy of the defective system. The decrease in the DFE near the domain

wall demonstrates that defects and defect pairs can be easily trapped by domain wall. The trapped defects will generate a local cluster field near the domain wall which can be explained to change the ferroelectric and optical properties. A decrease in energy will make the domain wall more stable state and create a higher energy barrier for domain wall motion because the activation energy for domain wall motion is increased by the migration energy for defect pairs. This is domain wall pinning. In particular, the trapped defects and defect pairs at domain walls will increase the coercive energy and threshold field, which is the pinning effect, making the domain wall motion difficult. A pinning effect affects the ferroelectric and optical properties and causes the ferroelectric degradation known as fatigue. [157] Successful growth of stoichiometric LiNbO₃ can prevent the pinning effect by defects, seen in congruent LiNbO₃, and improve the stability of LiNbO₃. The comparison on the energetics between intrinsic defects and Mg dopants explains the optical stability and low coercive field of Mg-doped LiNbO₃. When we compare these values (-0.05 eV for Mg_{Li}^{\bullet} and 0.15 eV for $Mg_{Nb}^{''''}$) with that of intrinsic defects (0.23 eV for V_{Li}^{\bullet} , 0.57 eV for Li_i^{\bullet} and 0.66 eV for $Nb_{Li}^{''''}$), Mg dopants show much less interaction with the Y-wall and are less trapped by Y-wall. The decrease in the trapped defects near the domain walls improves the optical birefringence and the domain wall motion. Thus, Mg-doped LiNbO₃ yields better optical properties and a reduction in coercive field after doping with Mg.

CHAPTER 6 DOMAIN WALLS IN LITHIUM TANTALATE

6.1 Introduction

LiTaO₃ is a ferroelectric material with trigonal structure, similar to LiNbO₃. It has a high Curie temperature (~940 K) [158] and spontaneous polarization (~50 $\mu\text{C}/\text{cm}^2$) [159]. Because of its unique optical properties, LiTaO₃ is a candidate for non-linear frequency convertors [160], electro-optics [161] and holography [162]. The control of shape of the domain is a key for optical applications. Different domain shapes can focus or defocus light in the plane and convert the input wave length to different wave lengths. Congruent LiTaO₃ shows lithium(Li) deficient composition with $C_{\text{Li}}/[C_{\text{Li}}+C_{\text{Ta}}]\sim 0.485$ [163]. Thus, congruent LiTaO₃ shows a large difference in Curie temperature from stoichiometric LiTaO₃ [164]. This non-stoichiometry of congruent LiTaO₃ can cause drastic changes in optical, electric and elastic properties near domain walls and affect the domain dynamics. [165] Recent studies [166, 167] show that the threshold field for domain reversal can be changed depending on the stoichiometry. Moreover, the crystallographic plane and shape of stable domain walls are changed from Y-wall, parallel to c-glide plane, to X-wall, perpendicular to c-glide plane. Figure 6-1 shows different domain wall structures in LiNbO₃ and LiTaO₃. At stoichiometric conditions, both form hexagonal shape domain wall structures of Y-wall, see figure 6-1(a) and (b). As their compositions are change to Li deficient condition for congruent system, however, they show different domain wall structures, see figure 6-1(c) and (d). LiTaO₃ changes its stable domain wall structure to X-wall with a triangular domain shape, but LiNbO₃ maintains the hexagonal shape domain with Y-walls. Gopalan *et al.* explained the hexagonal domain shapes using anisotropy of piezoelectric effects [165]. The change

of domain wall shape from hexagonal to triangular under different electromechanical coupling [168] have been studied by Shur. However, no systematic understanding of the role of defects for the change of the domain wall shape in congruent LiTaO_3 has developed. In this study, therefore, we focus on understanding the variation of the domain shape from the study of the energetics of the domain walls and intrinsic defects in LiTaO_3 .

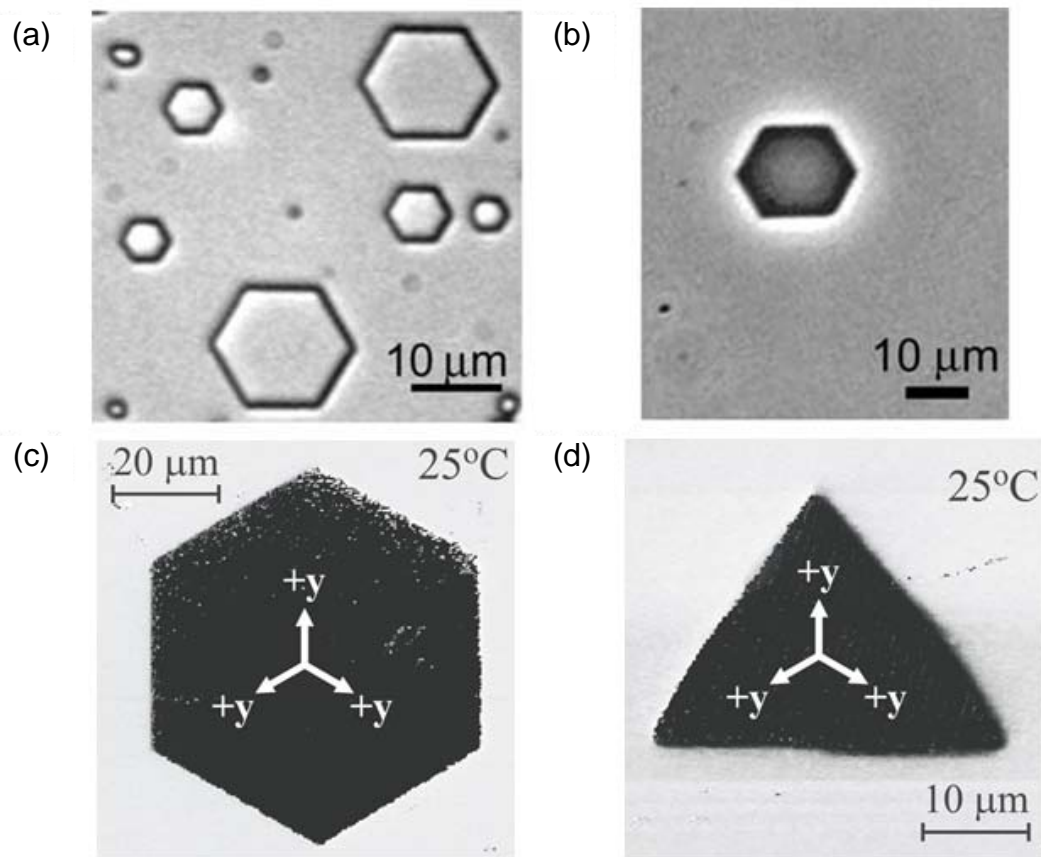


Figure 6-1. Different shapes of domains in LiNbO_3 and LiTaO_3 : (a) stoichiometric LiNbO_3 , (b) stoichiometric LiTaO_3 , [168] (c) congruent LiNbO_3 , (d) congruent LiTaO_3 . [96] Optical images: (a) domain revealed by etching, (b) phase-contrast-microscopy, (c) and (d) piezoelectric force microscopy phase contrast images.

6.2 Potential Development

As discussed for LiNbO₃, for systematic study such of domain walls, we use empirical method because of the size limitation on density functional study (DFT) methods. Since no potential is available for LiTaO₃ system, we developed a new potential by simultaneously fitting to the structure[169] and elastic properties[170] of LiTaO₃. The General utility lattice program (GULP) was used for the fitting. In fitting we retain the Li-O and O-O potential parameters developed by Jackson *et al.*, [53] This allows additional study for composite materials between LiNbO₃ and LiTaO₃. The full details for potential parameters are discussed in Chapter 2. Table 6-1 shows comparison between the potentials of LiNbO₃ and LiTaO₃

Table 6-1. The comparison of potential parameters between LiNbO₃ and LiTaO₃

Interaction	LiNbO ₃			LiTaO ₃		
	A (eV)	ρ (Å)	C (eV/Å ⁶)	A (eV)	ρ (Å)	C (eV/Å ⁶)
Li-O	950.0	0.2610	0.00	950.00	0.2610	0.00
Nb(Ta)-O	1425.0	0.3650	0.00	1131.56	0.3845	0.00
O-O	22764.0	0.1490	27.88	22764.00	0.1490	27.88
Shell parameter	LiNbO ₃		LiTaO ₃			
	Shell charge, γ	Spring constant, K_2 (eV/Å ²)	Shell charge, γ	Spring constant, K_2 (eV/Å ²)		
O2	-2.9	70.0	-2.9	70.0		
Three-body parameter	LiNbO ₃		LiTaO ₃			
	Force constant, k_θ (eV/rad)	Equilibrium angle, Θ_0 (deg)	Force constant, k_θ (eV/rad)	Equilibrium angle, θ_0 (deg)		
O-Nb(Ta)-O	0.5776	90	0.1405	90		

The two body interaction parameters, A, ρ and C between Nb and O are changed for Ta-O. Similarly, the three body interaction parameter, k_θ for O-Nb-O are changed for the O-Ta-O interaction.

6.3 Validation of LiTaO₃ Potential

The six oxygen octahedral cages in LiTaO₃ are continuously stacked with shared close-packed planes as shown in figure 6-2. Similar to LiNbO₃, the octahedral is filled in

the sequence of Li, Ta, vacant, Li, Ta, vacant along the z axis of trigonal structure. As the polarization state switches, the sequence can be change to Li, vacant, Ta, Li, vacant, Ta.

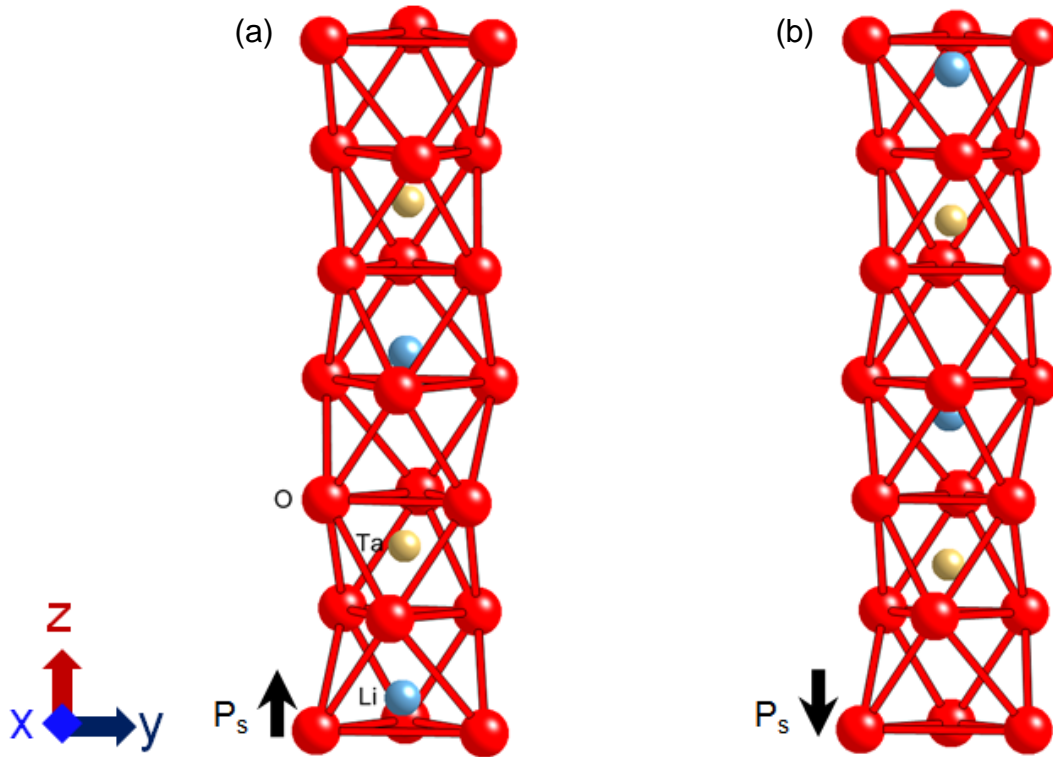


Figure 6-2. Crystal structure of LiTaO₃ for (a) +P_s and (b) -P_s in z-direction.

The trigonal structure with rhombohedral axes can be described by hexagonal lattice parameters $a=5.154$ and $c=13.783$ in the six formula unit hexagonal cell[92, 165]. The structural coordinates were obtained by least squares fitting method of neutron scattering data[169]. The elastic constants were measured by Takanaga and co-workers[170]. We have compared of our simulation results using new LiTaO₃ potential with structural coordinates and elastic constants, see Table 6-2 and figure 6-3. Our new inter-atomic potential reproduces the structural parameters extremely well, the largest error bar only 0.4% for the lattice parameter.

Table 6-2. Comparison of structural parameters and elastic properties of LiTaO₃ between experiments and simulations

Parameters		Simulations	Experiments	% Error
Lattice parameter	a	5.171499	5.154	0.34
	c	13.781961	13.783	-0.008
Fractional atomic coordinate	z (Li)	0.276429	0.279	-0.003
	z (Ta)	0	0	0
	x (O)	0.050146	0.0501	0.00005
	y(O)	0.352944	0.3436	0.009
	z(O)	0.068474	0.0687	-0.0002

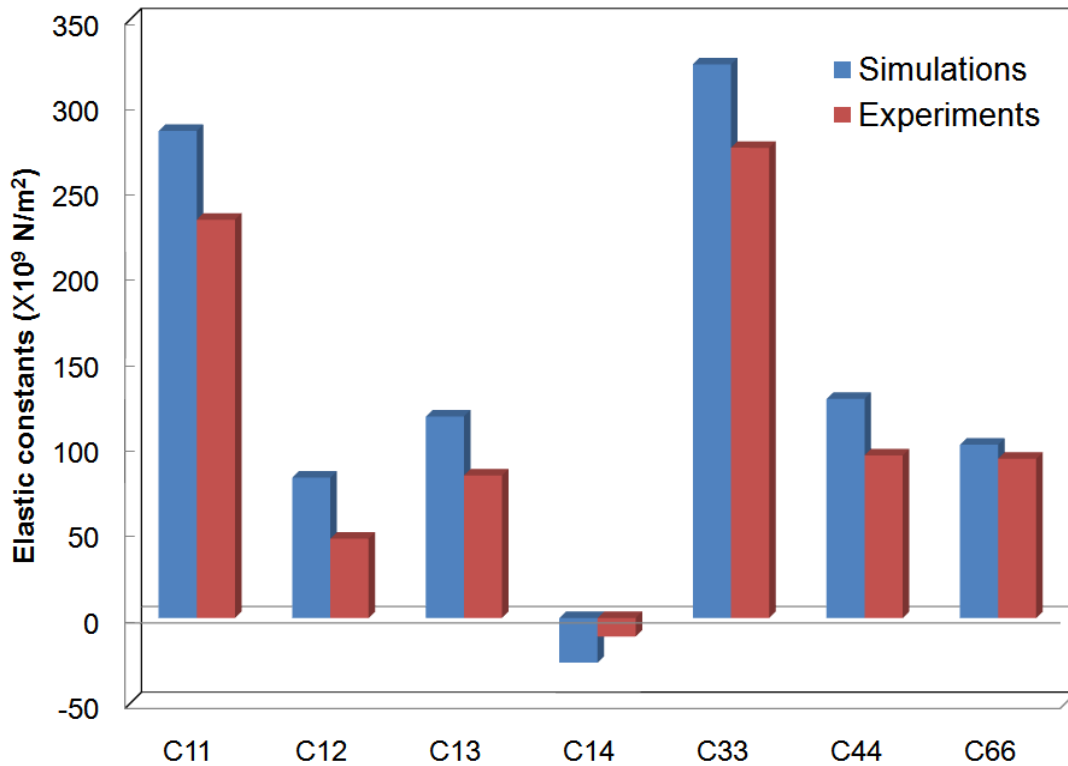


Figure 6-3. Comparison on elastic constants between experiment and simulation.

The elastic constants are important material parameters for mechanical applications. The simulations reproduce elastic properties of LiTaO₃ within acceptable limits. The C₁₁ and C₃₃ are the most important elastic constants for reproducing pure

longitudinal mechanical properties of trigonal materials. The errors from our simulation are only 22.3% for C_{11} and 17.75% for C_{33} . The elastic constants, C_{44} and C_{66} reproduce pure shear mechanical properties. Our simulation study also predicts them well with the 34.64% error for C_{44} and the 8.70% error for C_{66} . The elastic constants, C_{12} , C_{13} and C_{14} are relatively less important for mechanical application.

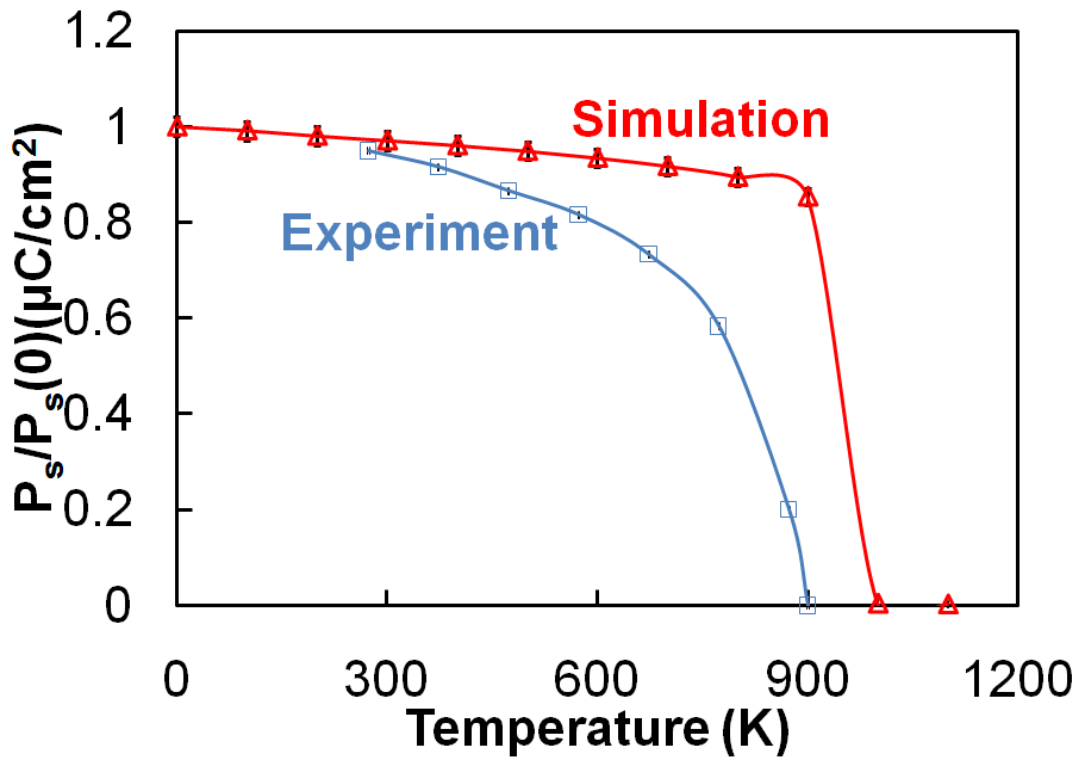


Figure 6-4. The comparison of normalized polarization between simulation and experiment [92].

The temperature dependence of the polarization was also determined using molecular dynamics simulations with the new inter-atomic potential. Figure 6-4 shows the variation of normalized polarization as a function of temperature. Although a difference in polarization profile at high temperature is observed, both experiment [171] and simulation results show gradual changes in polarization at low temperature and a relatively abrupt change of polarization near Curie temperature. Our simulation yield the

Curie temperature as 1000K, which matches quite well with experimental value, of $\sim 974\text{K}$ [163] for stoichiometric LiTaO_3 . Therefore, we have confidence that the new potential will be able to discuss the energetics of domain wall and defects.

6.4 Energetics of Domain Walls in Lithium Tantalate

Similar to LiNbO_3 , LiTaO_3 also has two different domain walls; Y-walls, parallel to c-glide plane and X-walls, perpendicular to c-glide plane. Simulation studies are performed in order to determine the energetics of the two domain walls using both DFT calculations and empirical method with our potential. Both methods consistently show that the Y-wall sits between oxygen planes and X-wall sits between atom planes, see figure 6-5. Because the DFT method is known to be more accurate than the empirical method, the comparison between two methods is a very good way to validate our potential. DFT calculation yields a Y-wall energy of 60 mJ/m^2 when the center of Y-wall is sitting between two anion planes. It is also possible to determine the Y-wall energy at transition state by fixing the wall at the atom plane. For the Y-wall at the cation plane, the maximum domain wall energy of 78 mJ/m^2 is observed. Assuming that this is the maximum in energy, these calculations yield a Peierls barrier to motion of 18 mJ/m^2 [172]. The corresponding analysis using the empirical potential yield an minimum energy of 70 mJ/m^2 and maximum energy of 113 mJ/m^2 with two different locations of the Y-wall. Thus the empirical study with our potential yields a Peierls barrier of 43 mJ/m^2 , which is twice larger value than DFT study. The Peierls barrier is typically large, when the ratio between domain wall width δ and the lattice periodicity d , δ/d , is less than one. We shall see that the domain wall widths are quite narrow, is consistent with the Peierls potential.

The two methods also agree on the equilibrium position of the X-wall. The lowest energy for the X-wall is observed at the center between the ion planes. DFT calculation yields an X-wall energy of 63 mJ/m^2 and empirical method yields 80 mJ/m^2 . We also perform the calculation of energy by fixing the X-wall position to atom plane. The DFT calculation yields a X-wall energy of 75 mJ/m^2 at atom planes, and empirical method yields 97 mJ/m^2 . Thus the DFT method yields a Peierls barrier of 12 mJ/m^2 and empirical study with our potential yields a Peierls barrier of 17 mJ/m^2 .

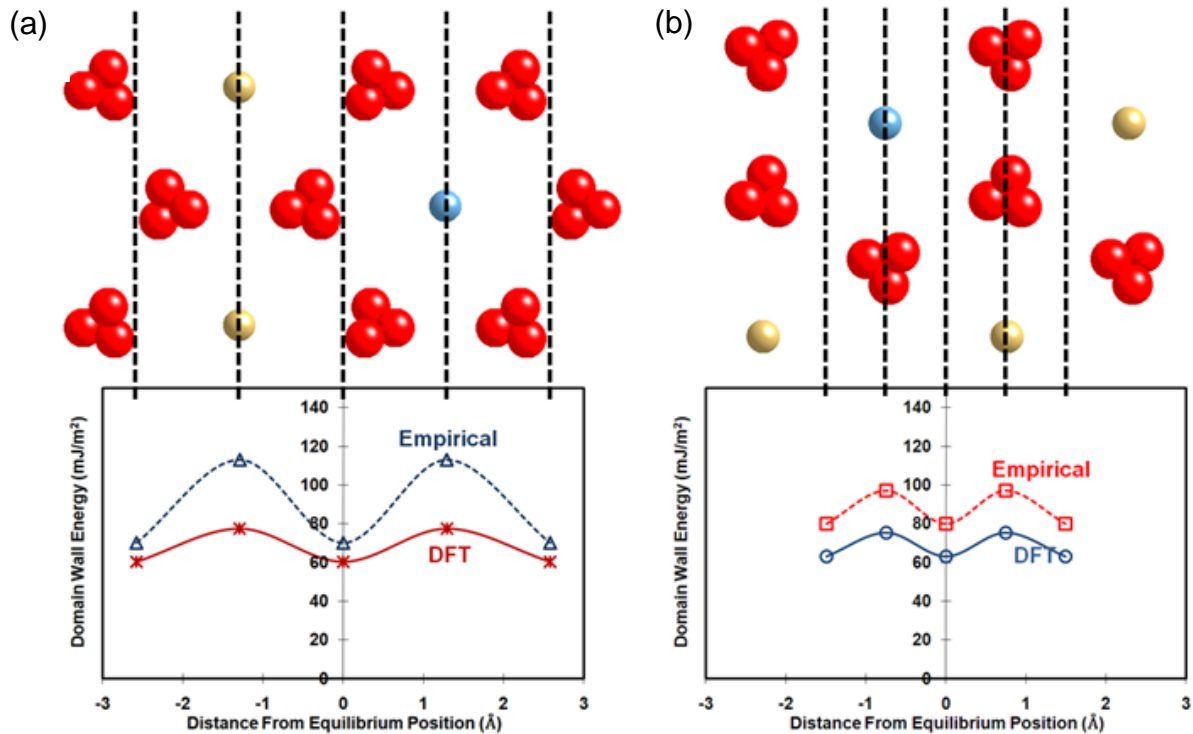


Figure 6-5. Domain wall energy comparison in LiTaO_3 . (a) Y-wall at cation plane and between anion planes (b) X-wall at cation-anion mixed plane and between mixed planes.

Although, as is to be expected, the DFT and empirical values do not precisely agree, both methods do predict the Y-wall shows slightly lower energy than X-wall, 3 mJ/m^2 for DFT method and 10 mJ/m^2 for empirical study. This conclusion is consistent

with the conclusions of Scrymgeour and his coworkers[96] based on calculations using Ginzburg-Landau-Devonshire theory.

The comparison on the energetics between LiNbO_3 and LiTaO_3 will improve our understanding on the properties of the domain walls. Figure 6-6 compares the domain wall energetics between LiNbO_3 and LiTaO_3 . The domain wall energies of LiTaO_3 are only one third of that of LiNbO_3 . Higher domain wall energy of LiNbO_3 can be understood by difference in the ionic radii of a Ta ion and a Nb ion. The smaller ionic radius of the Nb ion allows it to displace a larger distance and leads to a larger lattice mismatch with higher piezoelectric and electrostrictive constants.[173]. Thus, LiNbO_3 shows higher domain wall energies with larger piezoelectric effect. The lower domain wall energy can also explain the relatively lower coercive field for LiTaO_3 (15~17 kV/cm) [164] than that of LiNbO_3 (33.14~40.54 KV/cm) [174].

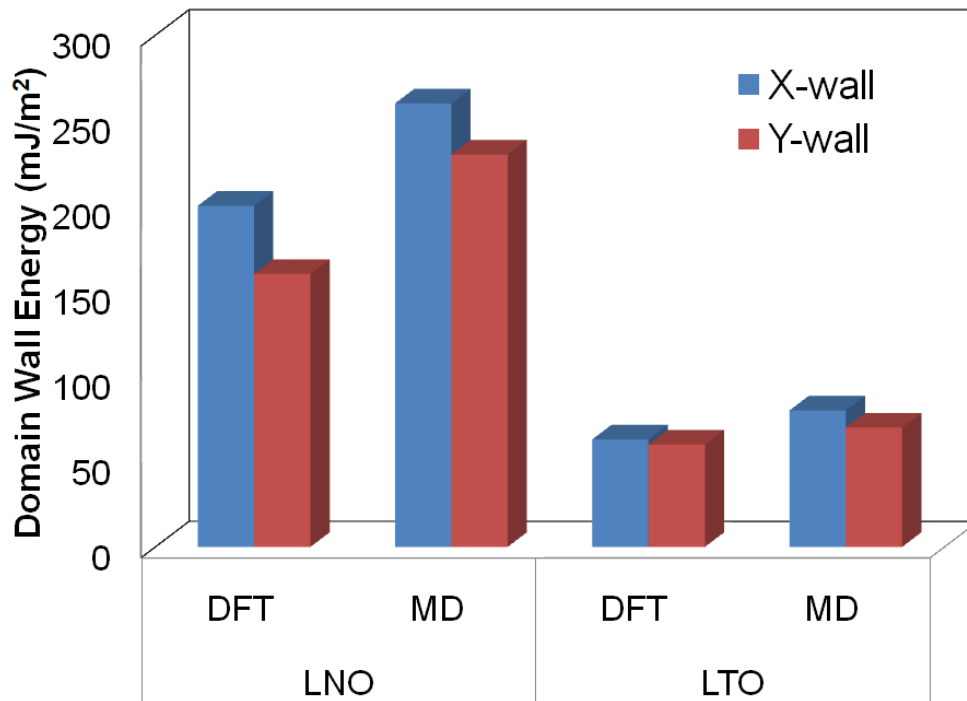


Figure 6-6. Domain wall energy comparison between LiNbO_3 (LNO) and LiTaO_3 (LTO).

As discussed in Sec. 6.1, the domain wall structures between LiTaO_3 and LiNbO_3 are significantly different at Li deficient condition. This can be understood by the difference in domain wall energetics between LiTaO_3 and LiNbO_3 . For LiNbO_3 , significant energy differences between Y-wall and X-wall are observed from both of MD and DFT methods; Y-wall is energetically lower by 40 mJ/m^2 for DFT and 30 mJ/m^2 for empirical study than X-wall. For LiTaO_3 , however, the only minor differences in domain wall energies are expected between Y-wall and X-wall from both methods; the difference is only 3 mJ/m^2 for DFT and 10 mJ/m^2 for empirical study. As we discussed on Chapter 5, the X-wall has a relative higher tendency to lower its energy during interaction with antisite defects than that of Y-wall. As we will discuss on Sec. 6.6, Ta_{Li}^{4+} compensated by four V_{Li}' defects are the major defect pair in congruent LiTaO_3 . With such small differences in domain wall energy of LiTaO_3 , the preferred domain walls are easily switched by defects-domain walls interactions. Thus, the shift of preferred domain wall orientation from Y-wall to X-wall is observed from LiTaO_3 . The change in the shape of domain walls can thus be explained. Figure 6-7 shows two possible shapes of X-walls: triangle and hexagon. The white region represents the “up” polarization and shaded region represents “down” polarization region. The arrow represents the orientation of displacements of three different oxygens near the X-walls. For triangular domain shape with X-walls, all three X-walls, aligned along three edges of the triangle have the same origin of oxygen displacements, see figure 6-7(a). In this particular case, X_I -walls are created along each edge of the triangle. For the opposite case, three X_{II} -walls are expected. For the hexagonal shape, however, additional edges, which are aligned with oppositely orientated X-walls, are expected, see figure 6-7(b). Because the

antisite defect show higher interaction with especially X_I -wall to lower its formation energy, additional three X_{II} -wall edges are less preferred. Therefore, the hexagonal shapes of the domain walls are less likely for congruent LiTaO_3 . Thus, X_I -walls with the triangular shapes are observed for congruent LiTaO_3 . This is also consistent with experimental preference of X_I -wall for congruent LiTaO_3 . [96]

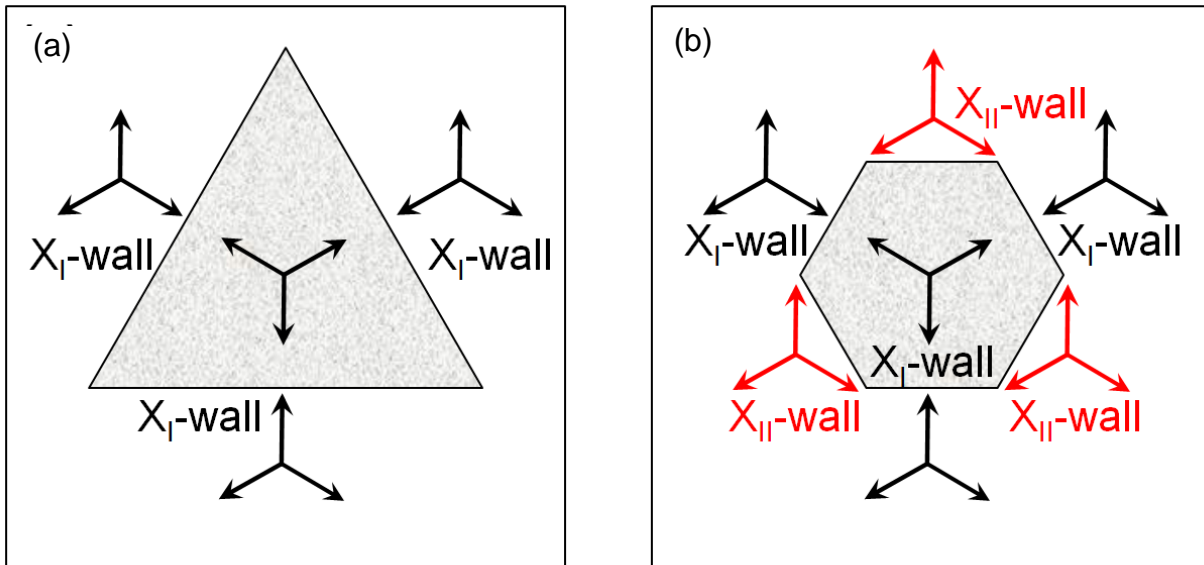


Figure 6-7. The schematic view of two possible shapes of X-walls: (a) triangle and (b) hexagon.

6.5 Domain Wall Structure at Transition State

In Sec. 6-4, we discussed the Peierl potentials and the two structurally distinct positions of domain walls. The Y-wall sits on either the cation plane or between two anion planes. Similarly, the X-wall sits on either cation-anion mixed plane or between mixed planes. In Chapter 4, we discussed the structural change near the domain walls at optimized states. Intuitively, we can expect that the atomic structure at the domain wall plane will be the average of the structures on the opposite sides. In this section, we discuss the structural differences in the Y-wall and X-wall at their transition states.

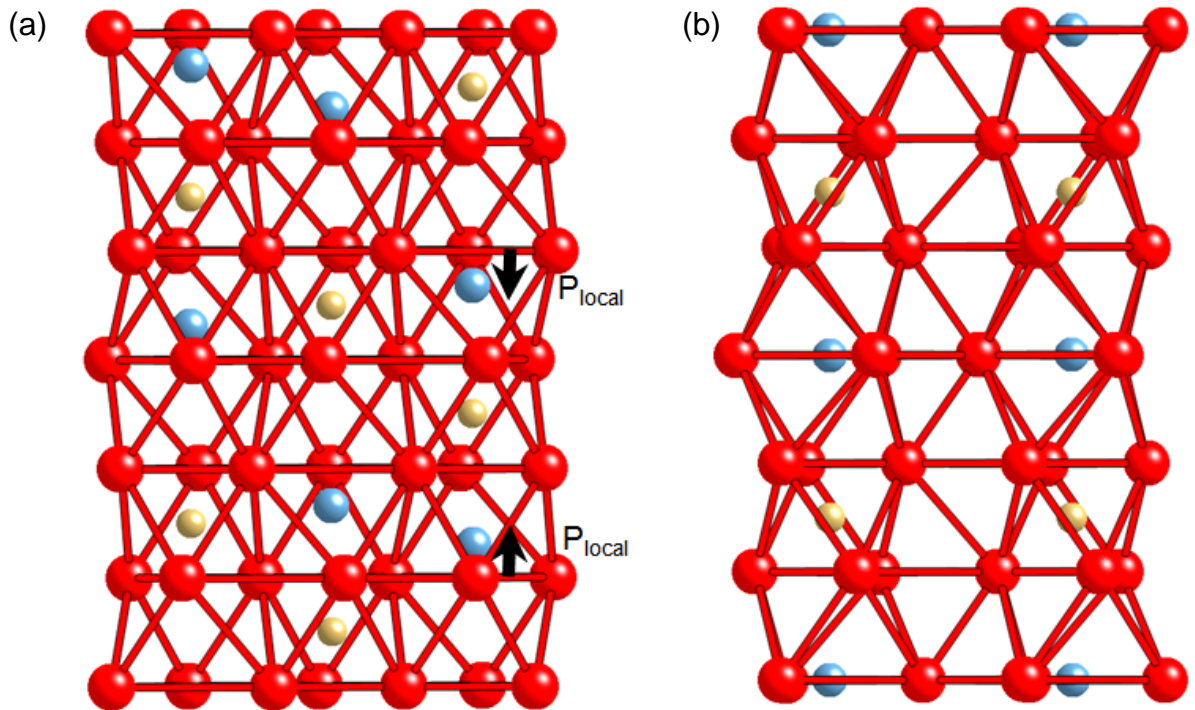


Figure 6-8. Structural arrangement of cations on (a) the Y-wall plane and (b) the X-wall plane at the transition state.

Figure 6-8 shows the domain wall planes of LiTaO_3 at the transition states. For both domain walls, Ta atom sit at the center of the oxygen cage, which is their position in paraelectric state. However, the walls show two different behaviors for the Li atoms on the atom plane. For the Y-wall, the Li atom moves above and below from the oxygen plane in hexagonal Z-direction, to creates a stack of local dipole moment on the domain wall. In other words, the structure of Li atoms on Y-wall plane looks like a mixture of the up and down polarization. However, the local dipole moments are cancelled out by equal and opposite motion of Li atoms, so the Y-wall leads net zero polarization on the domain wall plane. For the X-wall, however, Li atom sits at the exact center of the oxygen planes which can be understood as the paraelectric structural position. The positional change of Li atoms is more continuous through the X-wall. Thus, any of the

local z-directional dipole moments can be observed from the X-wall planes. Although neither domain wall shows a net polarization in domain wall plane, Y-wall plane shows a mixture of the up and down ferroelectric structures while the X-wall has the paraelectric structure. We also observed similar patterns for LiNbO₃.

6.6 Defects in Lithium Tantalate

Defect formation energy (DFE) calculations are also performed using the Mott-Littleton (ML) method with our developed potential. In Table 6-3, the DFEs are reported for possible intrinsic defects in the structure. The interstitial site is chosen at fractional coordinate (0.0, 0.0, 0.13936) which corresponds to the center of the empty oxygen octahedron of the structure. To understand the effect of temperature for DFEs, DFE calculations are performed at two different temperatures (0K and 300K). The simulation results show very similar values with minor difference in DFEs at two different temperatures.

Table 6-3. Intrinsic defect formation energies.

	Formation energy per defect (eV)	
	0K	300K
Li_i^\bullet	-7.48	-7.56
$Ta_i^{\bullet\bullet\bullet\bullet}$	-104.82	-105.50
O_i''	-11.39	-11.75
V_{Li}'	9.50	9.26
$V_{Ta}^{\bullet\bullet\bullet\bullet}$	120.87	120.00
$V_O^{\bullet\bullet}$	19.44	19.28
$Ta_{Li}^{\bullet\bullet\bullet\bullet}$	-100.94	-101.42

We should note that the individual point DFEs do not have any direct significance unless they are combined in charge neutral defect clusters. Therefore, the combination

of those defects to form the Schottky, Frenkel, or pseudo-Schottky defect pairs are considered in Table 6-3. Pseudo-Schottky defect pair consists of two vacancies among three components of LiTaO_3 . Two different oxide states, Li_2O and Ta_2O_5 , are considered as the reference state for non-stoichiometric defect pair, see Table 6-5. As we can see from the Table 6-4, the Li Frenkel pair is the most stable defect pair among different configurations.

Table 6-4. Frenkel, Schottky and pseudo-Schottky defect formation energies (eV/defect) (association effects are not considered between defects)

	Formation energy per defect (eV/defect)	
	0K	300K
Li Frenkel	1.01	0.85
Ta Frenkel	8.02	7.25
O Frenkel	4.02	3.76
Schottky LiTaO_3	4.81	4.36
Pseudo-Schottky Li_2O	1.76	1.64
Pseudo-Schottky Ta_2O_5	3.84	3.52

Table 6-5. Lattice energies of different oxide states

	Space group	Lattice energies (eV)	
		0K	300K
Li_2O	<i>Fm3m</i>	-33.15	-32.89
Ta_2O_5	<i>P6/mmm</i>	-312.07	-311.77
LiTaO_3	<i>R3c</i>	-174.26	-174.02

Similar to LiNbO_3 study, complex defect models are also considered in order to explain the experimentally observed lithium deficiency condition for congruent LiTaO_3 . Three different models which can explain the congruent growth condition of LiTaO_3 are considered; Antisite Ta compensated by Li vacancies, Antisite Ta compensated by Ta

vacancies, and Interstitial Ta compensated by Li vacancies. Table 6-6 shows the energy comparison between different defect models. Our calculation predicts Antisite Ta compensated by four Li vacancies to be the most energetically favorable defect pairs among three different models.

Table 6-6. Energies of possible reactions that lead to Li₂O deficiency

	Formation energy per Li ₂ O unit (eV)	
	0K	300K
$Ta_{Li}^{\bullet\bullet\bullet\bullet} + 4V_{Li}'$	2.05	1.86
$5Ta_{Li}^{\bullet\bullet\bullet\bullet} + 4V_{Ta}^{\bullet\bullet\bullet\bullet}$	5.78	5.17
$Ta_i^{\bullet\bullet\bullet\bullet} + 5V_{Li}'$	2.64	2.41

6.7 Conclusion

A new LiTaO₃ potential is developed and shows very good agreement with study experimental properties on LiTaO₃. Also, the potential gives very good agreement with DFT results on domain wall energetics and defect formation energies. The comparison of domain wall energetics and structures between LiNbO₃ and LiTaO₃ shows the two systems can lead very different domain wall energetics in spite of the similarity in their structures and properties. LiTaO₃ shows a domain wall energy of only one-third of that in LiNbO₃ which explains the difference between two systems. Preferred orientation and shape of domain walls in LiTaO₃ and LiNbO₃ are explained by the differences in the energetics of domain walls and defects-domain wall interactions. For LiNbO₃, the domain wall orientation remains oriented along crystallographic y-axes in congruent as well as stoichiometric LiNbO₃ crystals, since X-wall yields much higher domain wall energy than Y-wall. However, small energy difference between two domain walls in LiTaO₃ can be overcome by defect-domain wall interactions. The stable domain wall

structure of LiTaO_3 is shifted from Y-wall with hexagonal shape to X-wall with triangular shape during the change in stoichiometry.

CHAPTER 7 SURFACE DEPOSITION ON POLYTHIOPHENE MOLECULES

7.1 Introduction

Surface polymerization by ion-assisted deposition (SPIAD) enables the control of thin-film chemistry and morphology on the nanoscale during growth of conducting polymer thin films. Because SPIAD can be performed by a mass-selected beam of thiophene, it can simplify the growth mechanism by eliminating all non-mass-selected sources such as fragment ions, radicals and protons. The SPIAD of thiophene incidents has been carried out by both experimental and in a density functional theory-molecular dynamics (DFT-MD) study [175]. Previous experimental work on SPIAD found that the polymerization process can only occur at specific conditions such as specific ion/neutral ratios and energies of incidents [105, 115]. The previous DFT-MD study considered the deposition of mass-selected beams of thiophene at 100 to 500 eV/molecule energy range with thin film substrate of terthiophene (3T) oligomers. The study predicted that the terthiophenes on the substrate are mainly damaged by incident thiophenes at the energy range [175]. Thus, further study is necessary for optimizing the SPIAD process for polythiophene. As an extension of the previous study, the SPIAD of thiophene incidents is performed with relatively lower incident energy, 25 eV.

We also perform a study of the surface chemistry between a nanocrystalline quantum dot and thiophene polymer chains. PbS and PbSe nanocrystal photovoltaics devices are receiving concentrated attention for their potential usage as a solar cell [176, 177]. Especially, the combination between PbS nanocrystalline and organic materials, so called organic photovoltaics has been widely studied because of the low production cost and easy roll-to-roll processing [178-182]. Multijunction photovoltaics made by a

pair of near infrared and visible active layers could theoretically improve the solar to electrical conversion efficiency by up to 50%. High electron affinity PbS nanocrystals mainly act as an infrared active layer for multijunction photovoltaics, while the polymer layer acts as a visible active layer, leading to enhanced charge transfer. However, most multijunction photovoltaics are limited in their efficiency to 10 ~ 20% which is much below their theoretical limit [183, 184]. Recently, a non-heterojunction high efficiency (50%) photovoltaic device has been suggested using the property of the multiple excitation generation of PbS nanocrystals [185, 186]. Unlike traditional photovoltaic devices which generate one excitation for each observed photon, multiple excitations generated by one photon can improve the efficiency of photovoltaic device to up to 50% of solar energy. However, solar to electrical conversion efficiency is still below 10% because of surface chemistry, charge transfer efficiency, lifetimes of the excitons and other phenomena. [187-189] In this study, therefore, we focus on elucidating the detailed mechanism for the growth and polymerization of polythiophene and the charge transfer mechanism between PbS nanocrystalline and polythiophene layer to improve transferability of excitons generated by photons.

7.2 SPIAD

The mass-selected SPIAD technique is modeled by using a computer simulation tool, Spanish Initiative for Electronic Simulations with Thousands of Atoms (SIESTA). As we discussed on Chapter 2, SIESTA allows us to examine both the electronic structure and the kinetics of molecules using the DFT-MD methodology. Also, the linear scaling with system size of SIESTA allows us to simulate larger supercell systems by improving the high computational cost of plane-wave DFT-MD simulations. Initially, the basis set for Gaussian type electron orbitals is optimized for carbon, hydrogen and

sulfur system. In collaboration with Prof. Julian Gale of the Curtin University of Australia, one of the co-authors of SIESTA, we successfully optimized the necessary basis sets.

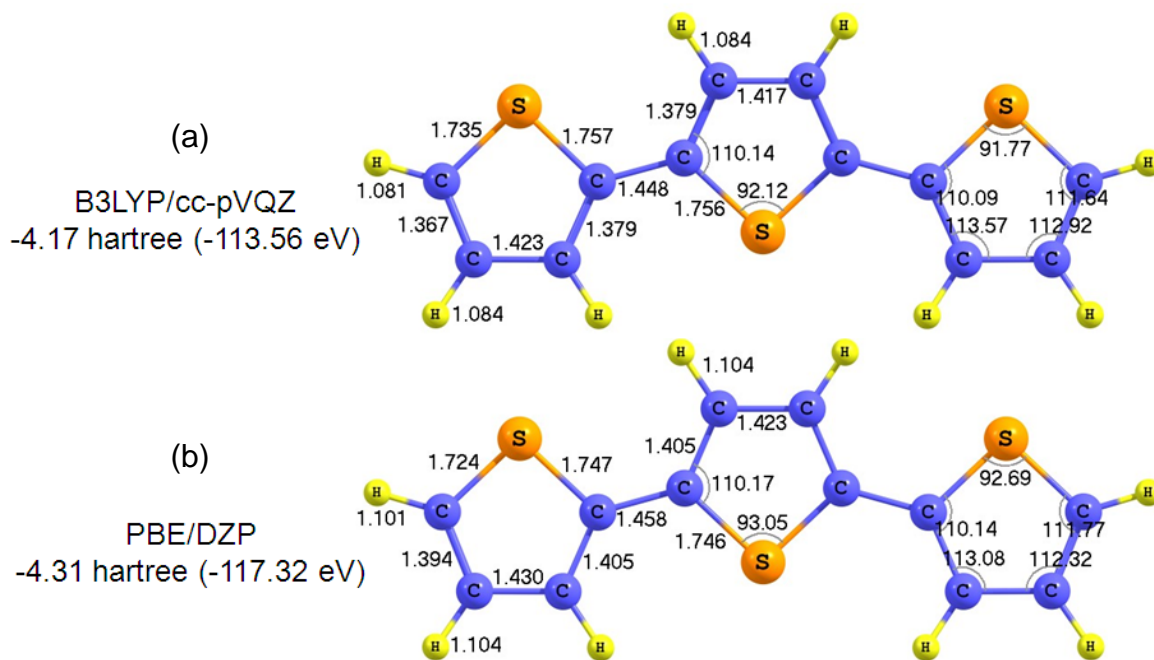


Figure 7-1. Comparison between hybridized HF calculation and linear scaled DFT calculation. Two different methods yield slight difference in bonding energies and structures of 3T polymer chain.

Figure 7-1 shows the comparison between quantum chemical calculation and linearly scaled DFT study for the structure of terthiophene. The B3LYP method [190-193] with correlation-consistent polarized valence quadruple zeta (cc-pVQZ) basis sets is used for hybridized quantum chemical calculation and PBE pseudopotential with DZP basis sets is used for DFT calculation. The energy on the left side of figure 7-1 represents the bonding energy of 3T. The DFT study with optimized basis sets estimate approximately 4 eV stronger bonding than the B3LYP calculation. The difference corresponds to a 3.3% difference in bonding energy of 3T polymer chain. The optimized structures are compared on right side. DFT overestimate the bonding lengths of C-C and C-H, but underestimate the bonding lengths of C-S. Also, the two methods show

small differences in the optimized bonding angle. However, the quantum chemical method requires much larger memory with a longer time scale; the quantum chemical method is approximately 200 times slower than that of DFT calculation. Taking into account the computational costs for the calculation, however, the linear scaled DFT efficiently predict reasonable results within a relatively small sacrifice on accuracy.

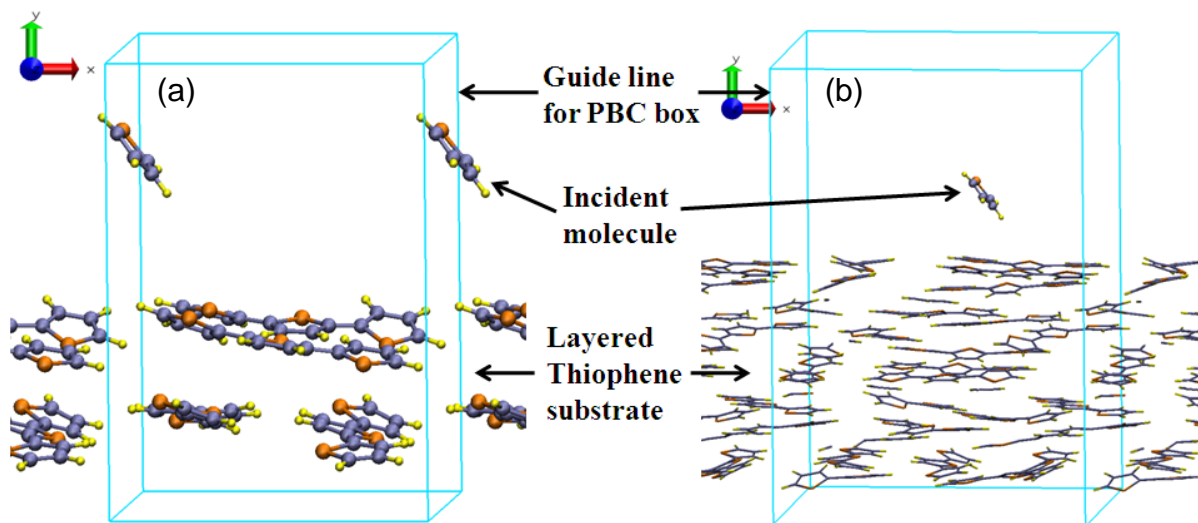


Figure 7-2. The schematics of two structures with different system sizes. (a) Two layered structure with four terthiophenes (3T); Two 3Ts are parallel to each other in each layer. The backbone chains of 3Ts in first layer are perpendicular to that of second layer. Each 3T is separated by 3.5 Å. (b) Five layered structure of thiophene oligomers; Three 3Ts and two dithiophenes are combined in a layer. The backbone chain of each layer is angled 45° from upper layer. The distance between each layer is about 3.5 Å.

To model the SPIAD process, we create substrate structures of two different system sizes: a small simulation cell with only 3T molecules and a large simulation cell with a combination of dithiophene(2T) and terthiophene (3T), see figure 7-2. The large simulation cell includes five-layers of polythiophene with a total of 505 atoms. Thus, each layer has 101 atoms combination of three 3T and two 2T polythiophenes. The small cell includes 92 atoms with two layers with two 3T in each layer. Each polythiophene is separated by 3.5 Å within a layer and between the layers. For the small

system, the density of the substrates are chosen as 1.667 g/cm^3 which is similar to the value, 1.503 g/cm^3 , examined from X-ray study on 3T crystalline. For the large substrate, a relatively smaller density thiophene structure, 1.034 g/cm^3 is chosen to allow the study of the effect of density on reactivity of polythiophene as well as the effect of consecutive deposition.

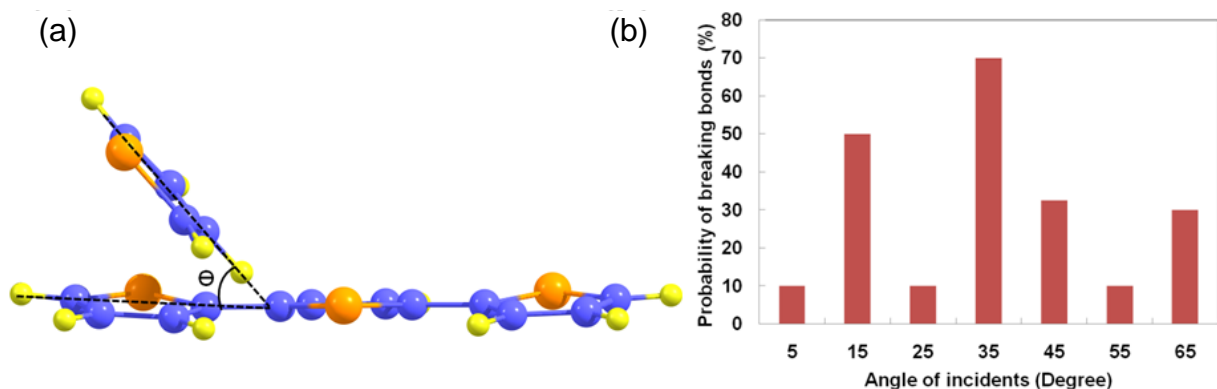


Figure 7-3. The angle between incident thiophene ring and substrate 3T ring is determined in order to study angle dependency of reaction. Probability chart shows that breaking C-S bonds are less correlated with angles of incident molecules from substrate 3T.

Because incident thiophenes with kinetic energy of 35 eV or higher cause damage to polythiophene and form debris after the collision, initial energy, 25 eV is used for incident thiophene molecules for deposition. 100 different trajectories of single thiophene deposition are examined for the small simulation cell. About 25 different trajectories (25% among single deposition trajectories) lead to breaking carbon(C)-sulfur(S) bonds of an incident thiophene or 3Ts in substrate. The C and S ions from the broken sites act as active particles for reaction and actively lead to either polymerization or cross-linking to the incident molecule or to another 3T. Depending on the orientation and deposition sites of incident molecules, different dynamic behaviors are observed. Figure 7-3 shows the probability of breaking the C-S bonds based on the angle between

the incident thiophene and the substrate 3T. The angle between two thiophene rings is chosen for the measuring, see figure 7-3(a). Each trajectory is distinguished depending on the angle and split into a 10 degree bin. As we can see from the figure 7-3(b), no general rule between breaking C-S bonds and the angles increase of the thiophenes is observed; Only one trajectory among 10 attempts successfully lead to the breaking of the C-S bonding at the angle between 0° to 10° , 20° to 30° and 50° to 60° . Therefore, the reactions between incident and substrate 3T are strongly correlated with the collision sites.

Figure 7-4 through 7-7 show four different trajectories observed from the study. The first trajectory, in which an incident thiophene is deposited into the side of a 3T molecule, forms a polymerization between a 3T and an image 3T in substrate, see figure 7-4. With breaking C-S bonds from the incident thiophene, two 3Ts create consecutive polymer chain with a bridge of the incident thiophene. This reaction generates a polymer fragment with a molecular weight, 576 g/mol. Another trajectory shows cross-linking between two 3Ts at different depths in the substrate, see figure 7-5. The incident thiophene breaks a C-S bond by pushing away the sulfur in 3T polymer chain. The carbon ion from the broken C-S bonding actively creates the bonding with carbon from another 3T molecule. This reaction leads to a final product with molecular weight, 492 g/mol which is equivalent to the molecular weight of two 3Ts. The reaction between an incident thiophene and a 3T molecule is also observed from figure 7-6. This reaction is obtained, when the C-S bonds with the incident thiophene is broken during the impact with the substrate. The incident molecule with a broken chain immediately reacts with a substrate 3T to generate a branching polymer fragment. The molecular

weight of final product is 330 g/mol. The fourth reaction shown in figure 7-7 breaks the C-S bonds in the center of 3T molecule. In this case, however, the broken 3T polymer chain fails to create a stable C-C bonding with either incident thiophene or other 3Ts. Therefore, the broken 3T polymer chain remains an active state. The molecular weights of the final products remain unchanged. Therefore, polymerization or crosslinking under 25 eV deposition of a thiophene can be understood as two step processes; breaking C-S bonding and creating stable C-C bonding between polythiophenes.

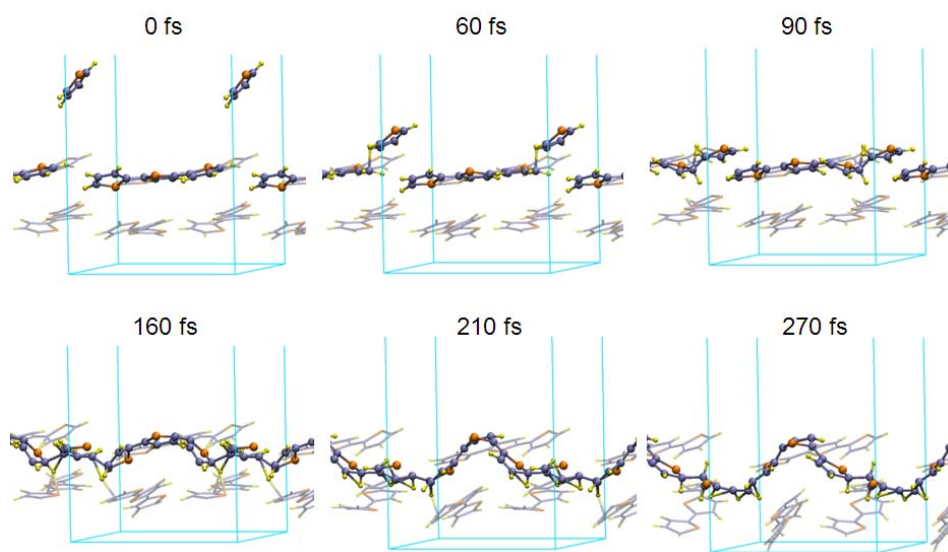


Figure 7-4. Snapshots at different time from DFT-MD simulations of neutral system. Surface polymerization and cross-linkings are observed from depositing of a thiophene molecules with 25 eV on a terthiophene oligomer thin film; polymerization between two 3Ts and an incident thiophene.

Figure 7-8 shows the distribution of molecular weight among successful trajectories leaded to broken C-S bonds. 13 successful trajectories, which successfully lead to new molecular weight products, are only observed among 100 trials. Even though it is difficult to determine probabilities with small number of successful trajectories, we observe 10 successful trajectories for $[3T]C_4H_4S$ resulting from third reaction, two trajectories for $[2T]C_4H_4S[3T]$ and one case for $[3T]C_4H_4S[3T]$. Our study successfully

reproduces different molecular weight products from surface polymerization and cross-linking processes.

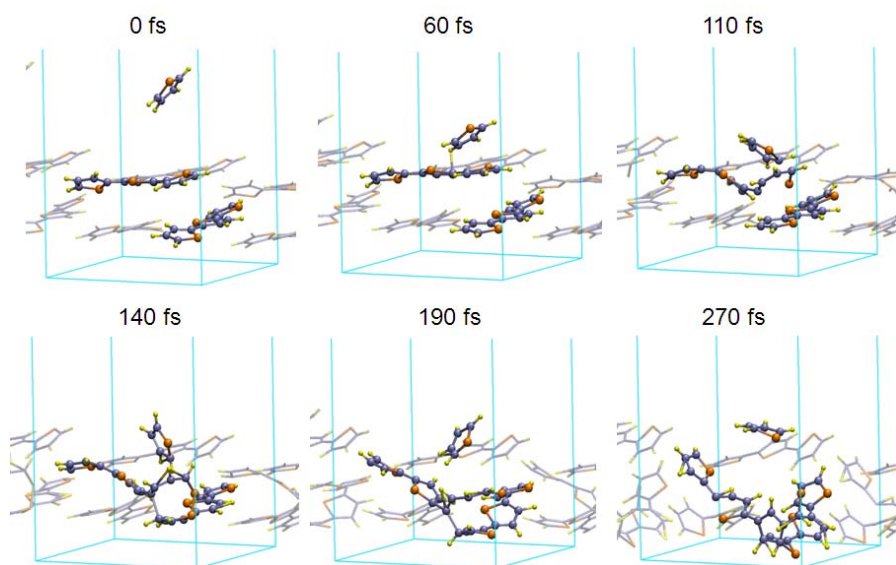


Figure 7-5. Snapshots at different time from DFT-MD simulations of neutral system. Surface polymerization and cross-linkings are observed from depositing of a thiophene molecules with 25 eV on a terthiophene oligomer thin film; crosslinking between two 3Ts.

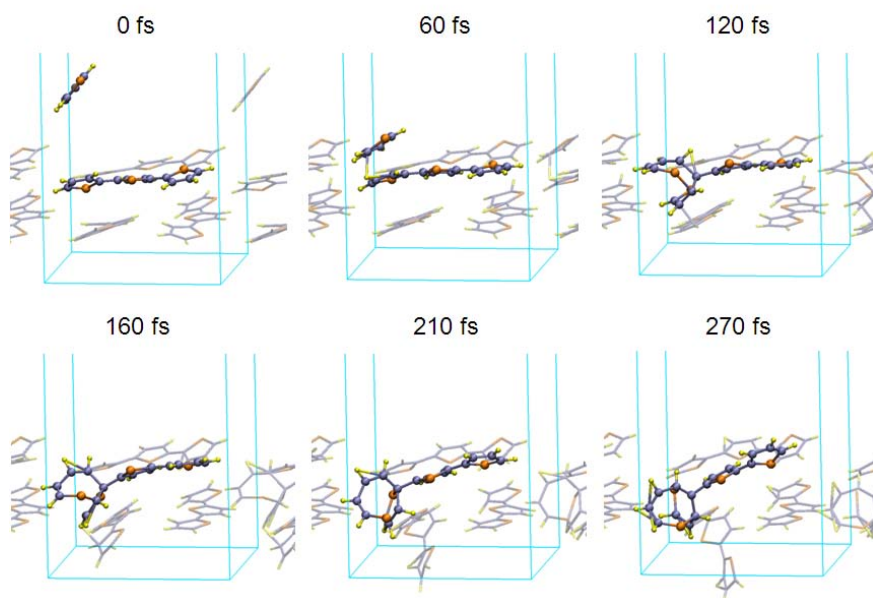


Figure 7-6. Snapshots at different time from DFT-MD simulations of neutral system. Surface polymerization and cross-linkings are observed from depositing of a thiophene molecules with 25 eV on a terthiophene oligomer thin film; polymerization between a 3T and an incident thiophene.

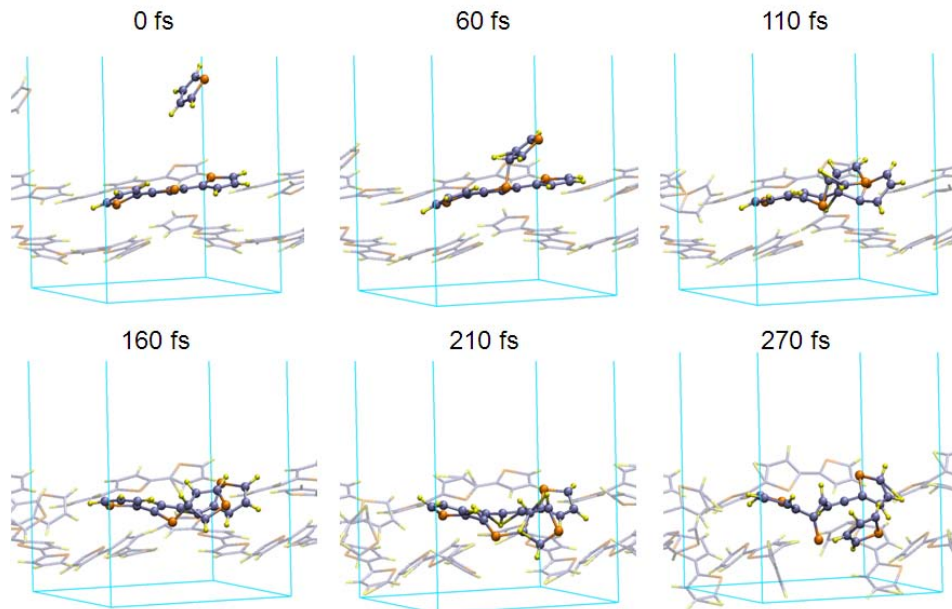


Figure 7-7. Snapshots at different time from DFT-MD simulations of neutral system. Surface polymerization and cross-linkings are observed from depositing of a thiophene molecules with 25 eV on a terthiophene oligomer thin film; broken 3T chain and an incident thiophene.

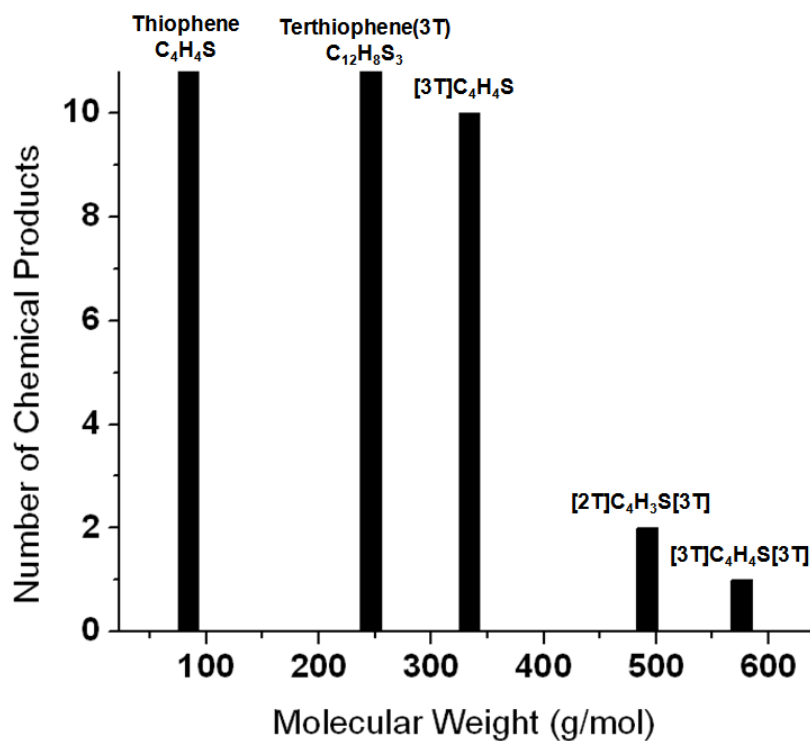


Figure 7-8. The distribution of molecular weight for four different trajectories which lead successful reaction with 3Ts in the substrate.

Because of the very much larger computational cost, only 5 trajectories of single thiophene deposition are performed with 25 eV of incident thiophene in large unitcells. As we observed from small system size results, surface polymerization and cross-linking of 3T with incident thiophene of 25 eV is a relatively low probability event. Moreover, the lower density of the large system also causes a lower reaction rate between polythiophenes. As a result, no polymerization or cross-linking reaction is observed from single deposition trajectories in a large simulation cell. We are currently running consecutive deposition in large unitcell system to characterize accumulated damage.

7.3 C₂H⁺ ion deposition on 3T polymer with PbS nanocrystalline

As we addressed in Sec. 7-1, the combinations of PbS nanocrystalline with polythiophenes has a potential applications for organic photovoltaics. The low electric conductivity between PbS nanoparticle and polythiophenes limits its efficiency for an organic solar cell. This limitation can be overcome with a change in surface morphology between thiophene and PbS nanocrystalline. We perform the simulation study by depositing C₂H⁺ ion on the substrate, in which a PbS nanocluster is surrounded by 2Ts and 3Ts. The positive charge was placed on the system as a whole and was determined to be located on the substrate. An incident energy of 100 eV kinetic energy is considered for the incident C₂H⁺ ion. Our simulation study shows that a bond between PbS nanocluster and a polythiophene is created by a process similar to the growth mechanism, discussed in previous section. Figure 7-9 shows the iso-surface of electronic charge density of DFT-MD. Initially, no bonding between terthiophene and PbS nanocrystalline is observed, as indicated in figure 7-9(a). As C₂H⁺ molecules are deposited into the mixed substrate of polythiophenes and PbS nanocrystalline, induced

bonding between terthiophene and PbS nanocrystalline is predicted to occur. In particular the incident molecule breaks the C-S bonding of 2T and generates the $C_{2T}-C_{in}$ bonding with it. The iso-surface of $C_{2T}-C_{in}$ bonding is clearly connected to the iso-surface of PbS nanocrystalline, see figure 7-9(b). Obviously, 2T creates electronic connection to the PbS nanocrystalline. Therefore, the active polymer chain generated from broken C-S bond of polythiophene can introduce electronic connectivity between thiophene oligomer and PbS quantum dots.

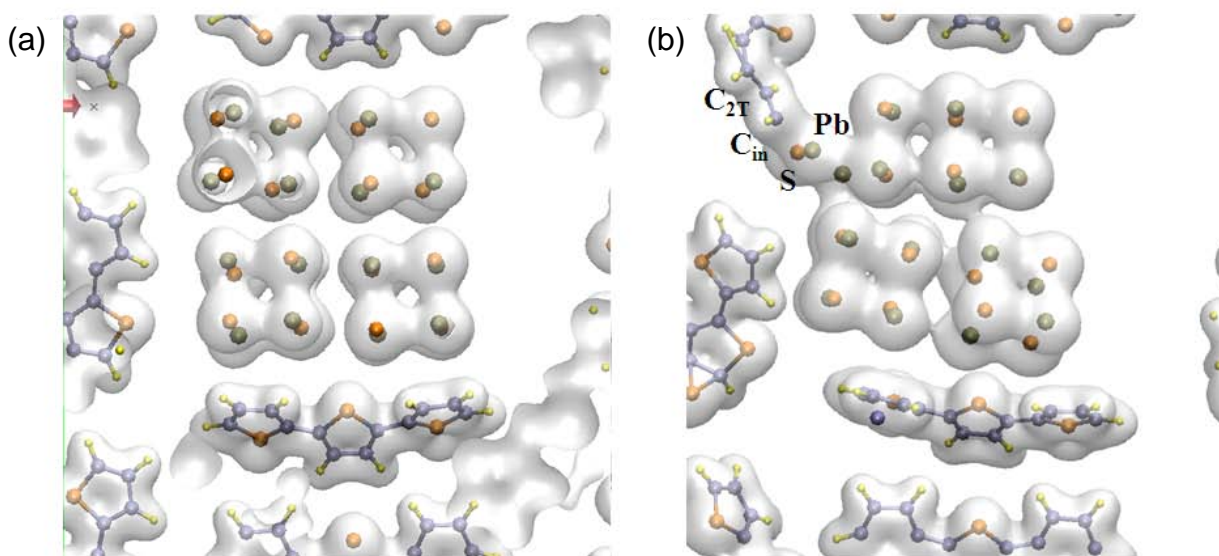


Figure 7-9. The iso-surface of electron density. The $C_{2T}-C_{in}$ bonding between incident particle, C_2H^+ and 2T at the site of the broken C-S bonding leads the connection to PbS nanocrystalline. C_{2T} and C_{in} represent the carbon from 2T and incident particle.

7.4 Conclusions

The growth and cross-linking of polythiophene is simulated using SPIAD method. Many different factors including the kinds of incident particles, collision angles and positions, and kinetic energy of incident particle affect the reactivity during SPIAD. In this study, the possible reaction mechanisms of thiophene incidents with polythiophenes at relatively low kinetic energy collision (25 eV) are demonstrated. The growth and

polymerization mechanism are observed as two step processes; breaking C-S bonding of thiophene and creating C-C bonding between broken bonds. We categorize four different reactions for the growth of thiophene chains. The study on surface reaction between PbS quantum dots and polythiophenes also confirms that broken C-S bonds are a key for further reaction of polythiophenes. We are currently performing simulations with larger cell in order to understand the effect on polymerization and cross-linking processes of polythiophenes from consecutive depositions of thiophenes.

CHAPTER 8 ADATIVE KINETIC MONTE CARLO (AKMC)

8.1 Introduction

Classical MD simulations are limited to short periods of time, almost always less than a microsecond. This is because the time step for MD simulations is in the order of a femtosecond. Thus, a simulation of 1 microsecond require approximately 1 billion steps, which is computationally very expensive. Several mechanisms have been proposed to bridge the time scale gap; parallel replica dynamics [194], temperature accelerated dynamics [195] (TAD) and kinetic Monte Carlo [196, 197] (kMC). Parallel replica dynamics provides a linear acceleration by running a replica of a state in each computing node and accepting the first escape. [198] TAD accelerates dynamics by performing MD simulation at elevated temperature. It obtains the trajectory of dynamics by neglecting non-physical behavior at an interesting temperature. TAD can reproduce true dynamics well, since the approximations are well controlled in. However, it still requires huge amounts of computing time to reproduce rare events. KMC is an alternative method. The kMC does not attempt to reproduce the dynamic trajectory. Instead, it calculates a list of possible transition events, and then chooses to execute one transition at random. The rate of each event will determine the probability of each event in the kMC. The list of transition events is then updated according to the current configuration. A trajectory for the system evolution is obtained by repeating this process. One problem with kMC is that it usually requires approximations to generate a list of possible escape paths. [198] A second problem is that the possible escape mechanism has to be known in advance. If the specified mechanism is not intuitive, it will be very difficult to obtain all possible transition states. The adaptive kinetic monte carlo (akMC)

method can resolve this issue. In akMC, the rate for each of the events can be calculated accurately from transition state theory [199] [200]. The list of events for the system at specific condition can be obtained using either classical interatomic potentials or even first-principles calculations [201] [202]. In this chapter, I will discuss the mechanism of akMC and how this concept is implemented into a code. I will test the code for the dynamic behavior of aluminum atom on an aluminum (111) surface.

8.2 Mechanism

8.2.1 Kinetic Monte Carlo (KMC)

The KMC algorithm simulates the time evolution of a system when processes can occur with known rates, r . At $t=0$, the system is in state i . Then, all kinetic events that are available at the state i are listed with the rate for the each event. We now calculate the total rate, R_{tot} for all events at state i using the cumulative function.

$$R_{tot} = \sum_{j=1}^N r_j \text{ for } j = 1, 2, \dots, N \quad (8-1)$$

where N is the total number of transitions at the state i . Then, one process among the possible kinetic events is chosen randomly with the probability proportional to its rate. The event will be chosen by

$$R_{j-1} < u \times R_{tot} < R_j \quad (8-2)$$

where u is a random number between 0 to 1.

Figure 8-1 shows a schematic illustration of the chosen process. One of processes will be chosen from the distribution of rates proportional to the rate constant.

The chosen event will be performed and the state i will move from another state k . The amount of time spent during this process is now calculated as:

$$\Delta t = -\frac{\log u}{R_{tot}} \quad (8-3)$$

where u is the random number between 0 to 1.

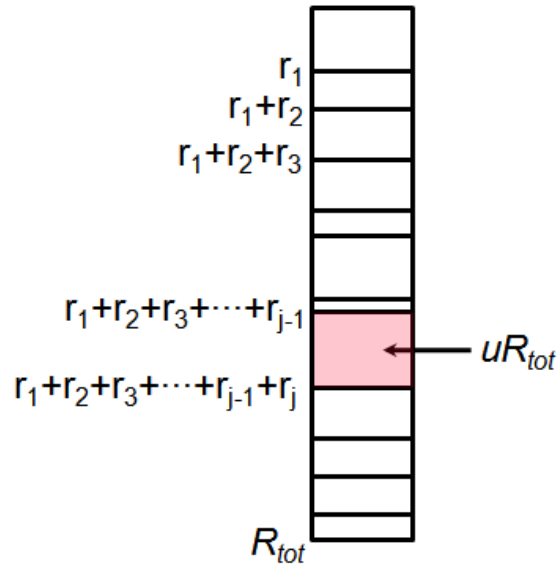


Figure 8-1. Schematic of the procedure for choosing the reaction pathway to advance the system to the next state in the standard KMC algorithm. The size of box is proportional to the rate constant for each event.

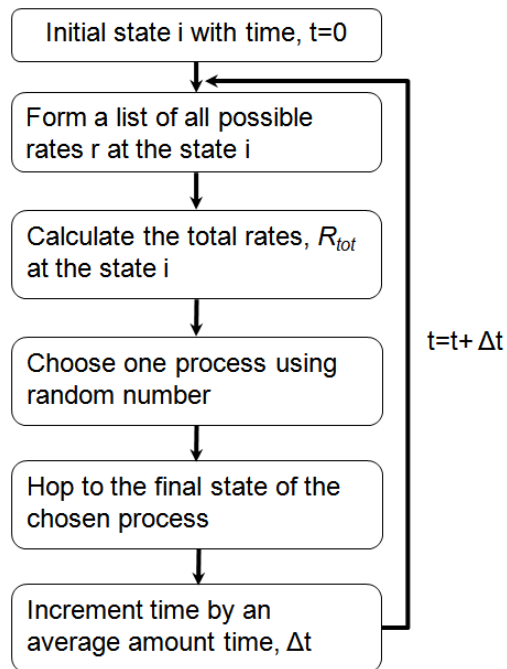


Figure 8-2. Flow chart illustrating the basic steps in the KMC algorithm.

Within the evolution of an accumulated time t by Δt , this process is repeated. Therefore, each step includes the probability of all events, even though that do not occurred. Figure 8-2 shows the flow chart for the KMC procedure.

8.2.2 Adaptive Kinetic Monte Carlo (AKMC)

Because unidentified reaction pathways are almost invariably missing from the list of rates, KMC simulations cannot reproduce the real dynamics. For the diffusion process, atomic movements can be different from those we might give by intuition alone. Although we can get more insight into the mechanism, this approach also cannot guarantee to find all the reactive events that could occur during the evolution of the system. This is the reason AKMC method developed. The AKMC method can reach long time scales while maintaining the accuracy of MD simulation. Henkelman and Jónsson [203] have proposed a variation on the KMC method, in which the list of rates can be obtained at each state. The main idea to this approach is to search for saddle points that are connected to the current state of the system. The dimer method [199] is typically used for searching saddle points. [58]. In the dimer algorithm, atoms climb uphill along the lowest eigenvector of the Hessian matrix until they reach the saddle point at the top. Figure 8-3 shows (a) a schematic view and (b) flow chart of the dimer searching method. The dimer method uses effective forces along the lowest curvature direction in order to find the saddle point. Thus, it is computationally efficient since the first derivatives of the potential is only required. [204] If all saddle points are searched, the list of rates can be obtained from the activation energy for each saddle point. Although the dimer method does not guarantee to find all saddles, most of the low-lying barriers can be found by a large number of randomly initiated searches. [205]

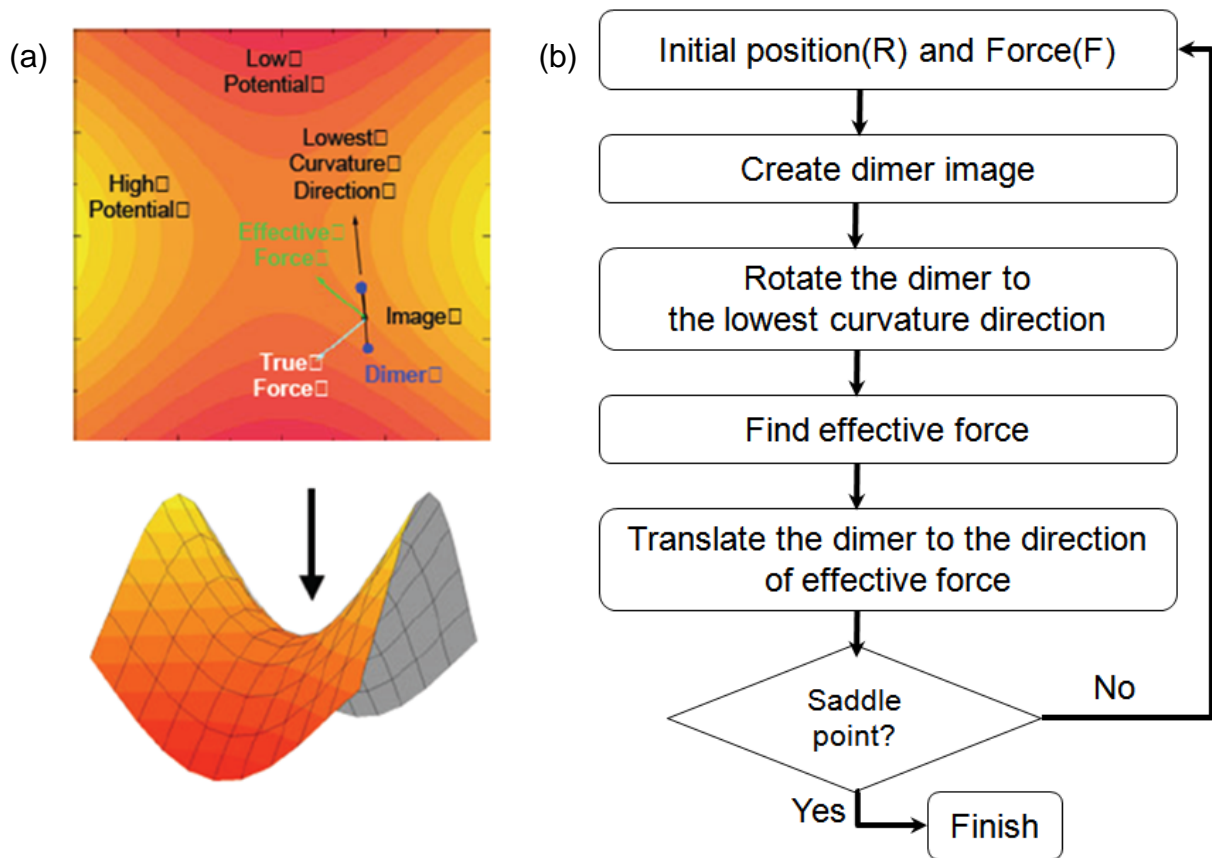


Figure 8-3. (a) The schematic view of dimer saddle point searching mechanism.[199] (b) Flow chart of dimer method.

8.3 Dimer Method with Two Dimensional Potential

I have implemented the dimer method into a new code. A two-dimensional test problem case [199] has been analyzed in order to test the new developed code. The dimer method successfully identifies three different saddle points. Figure 8-4 shows the comparison between our test using the new code and literature results[199]. The comparison shows that our code successfully reproduces the proper dimer behavior with this implemented two-dimensional potential.

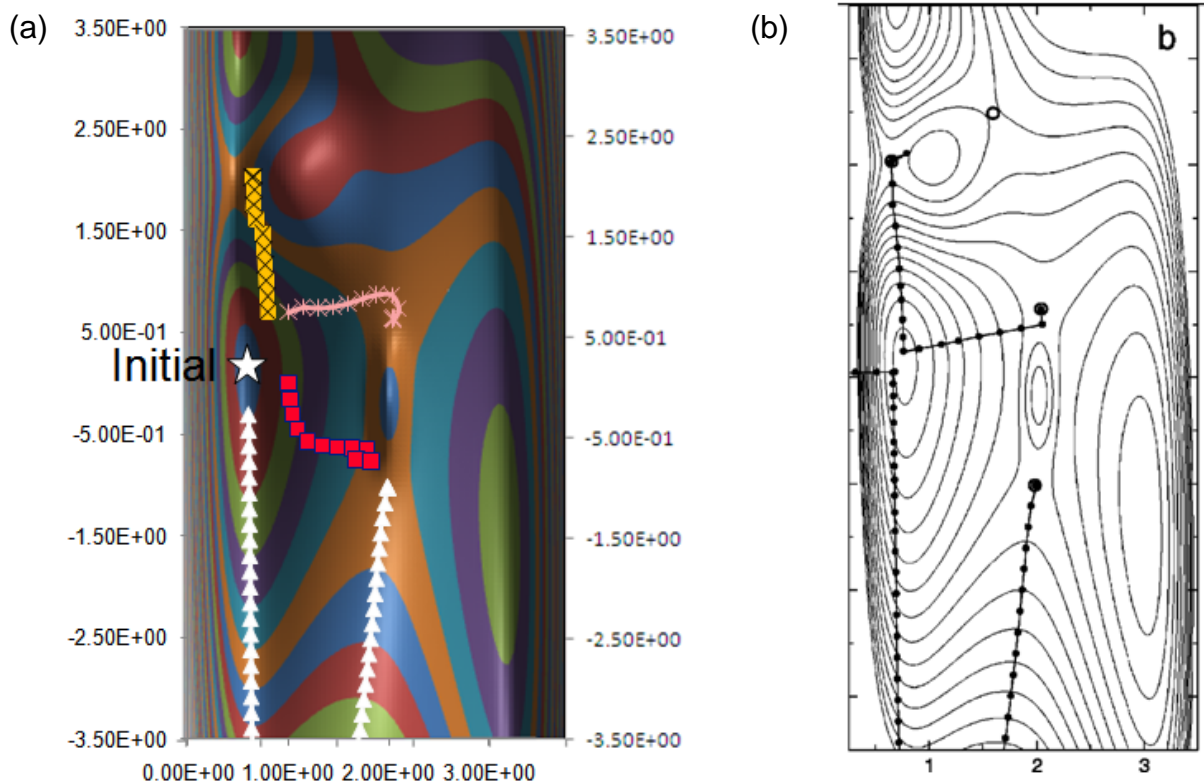


Figure 8-4. The comparison on searching behavior of dimer method between new developed code(a) and literature(b) [199]

8.4 Diffusion Process on (111) Aluminum(Al) Surface

KMC method is now also implemented into the new code. In order to test the code, we simulate the diffusion process of an Al atom adsorbed on (111) Al surface. We used the simple Lennard-Jones (LJ) potential for simplicity of the model problem. The standard form for LJ potential is

$$V_{LJ}(r) = 4\varepsilon_{LJ}[(\sigma_{LJ}/r)^{12} - (\sigma_{LJ}/r)^6] \quad (8-4)$$

where, $\varepsilon_{LJ}=0.392$ eV and $\sigma_{LJ}=2.64\text{\AA}$ are obtained from the literature.[206] A six layered Al structure which has a (111) planar surface is prepared and single Al atom is positioned on the top of the surface. Figure 8-5 shows a schematic view of initial Al structure with (111) surface. The color of the top Al atom is changed for only clarity. The

lines represent the border of the PBC cell box; therefore, atoms are repeated in x and y direction and only z direction remains as surface state with vacuum space. We performed AKMC simulation with the dimer method. Because the FCC structure has ABCABC stacking sequence along the (111) planar direction, two adsorption sites, A and B, are available, see figure 8-6. Thus, we can expect four different diffusion behaviors from two states occupying two sites; A to A, A to B, B to A, B to B. All four processes are observed in our AKMC study. Figure 8-7 shows four possible process obtained from our study. The study shows that the state A has a 0.002 eV lower energy than that of state B. However, only one saddle point with a 0.102 eV higher from the state A, is observed from all different processes. Thus, two different activation processes are possible with activation energies, 0.102 eV from state A and 0.100 eV from state B. We consider the energy at state A as a ground energy. Therefore the energy at state A is zero.

With the dimer method, the adsorbed atom moved to the transition state along the lowest curvature direction. The variation of substrate structure is the result of shifting of atoms along the PBC. The dimer searching steps, identifying saddle points using dimer method, are repeated in order to find out almost all possible transition states. For this study, 12 dimer searching steps are used for each transition event. After searching 12 events of transition, the total rate for a transition event is calculated. Using the random number, one transition event among 12 different trajectories is chosen and accepted. With a different random number, time for the transition event is calculated. In this case, the calculated time for the first transition event is 2.11 ps. Figure 8-7 represents the time

evolution of kinetic process until the AKMC simulation reaches to 0.15ns. 130 transition events occur for this run.

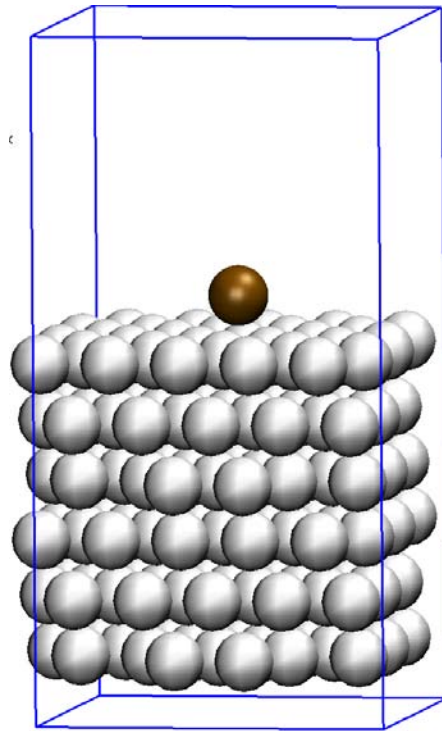


Figure 8-5. The schematic view of six layered initial structure on (111) Al surface. The color of top Al atom is changed to brown for the clarification. The blue line represents the PBC cell box; therefore, atoms are repeated using the PBC in x and y direction and only z direction remains as surface state with vacuum space.

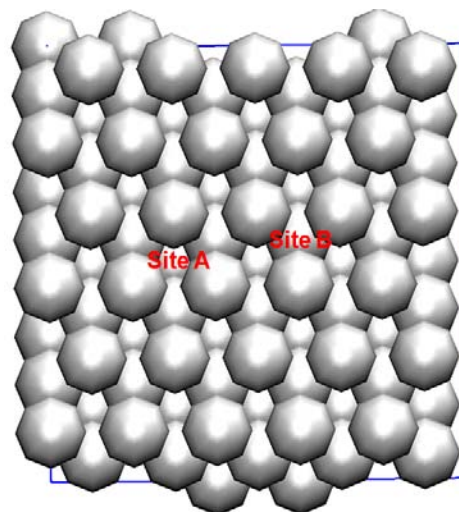


Figure 8-6. Two possible adsorption sites for an Al adatom.

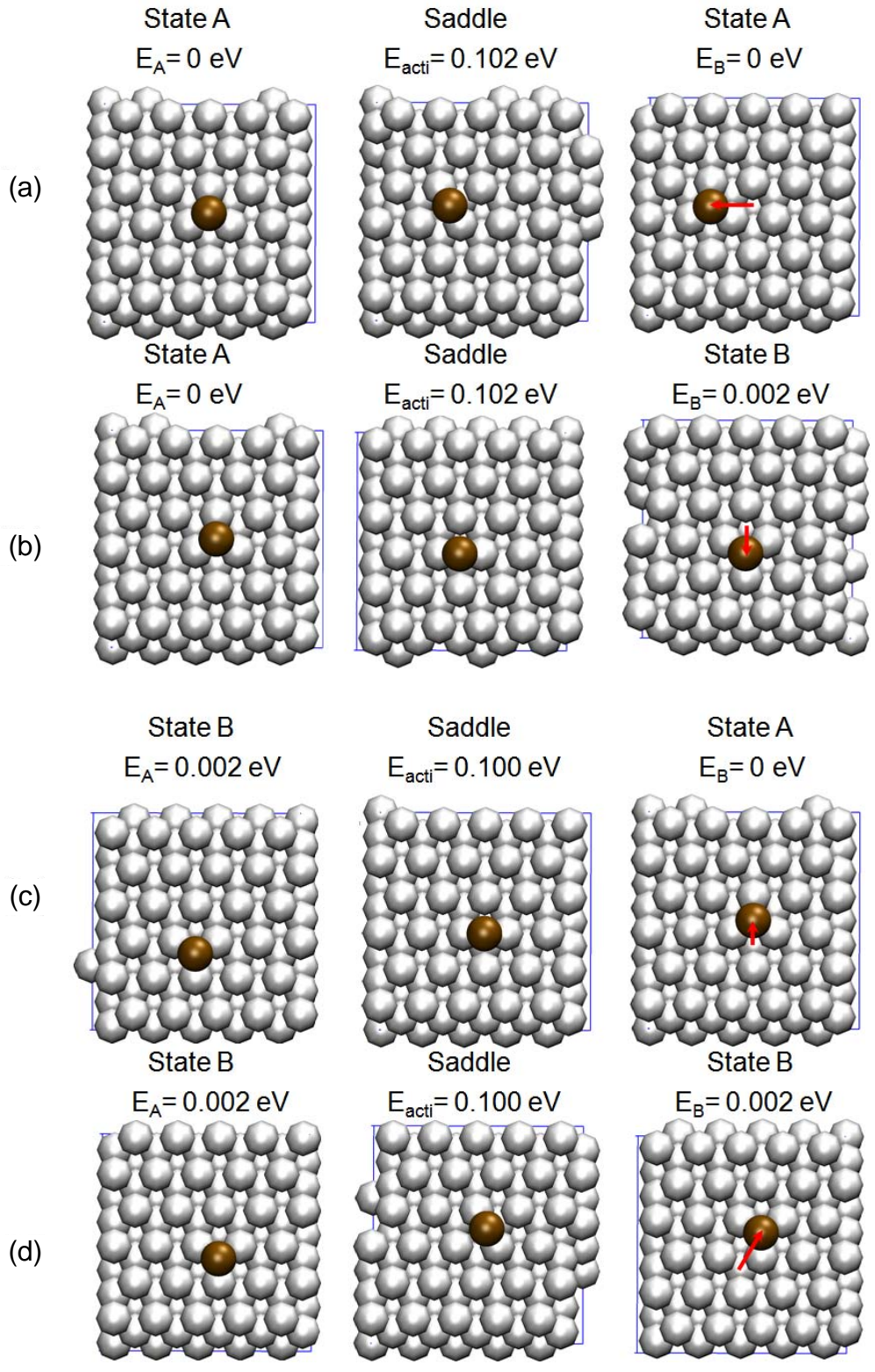


Figure 8-7. Four different diffusion processes of an Al adatom on (111) Al surface; (a) state A to state A, (b) state A to state B (c) state B to state A (d) state B to state B.

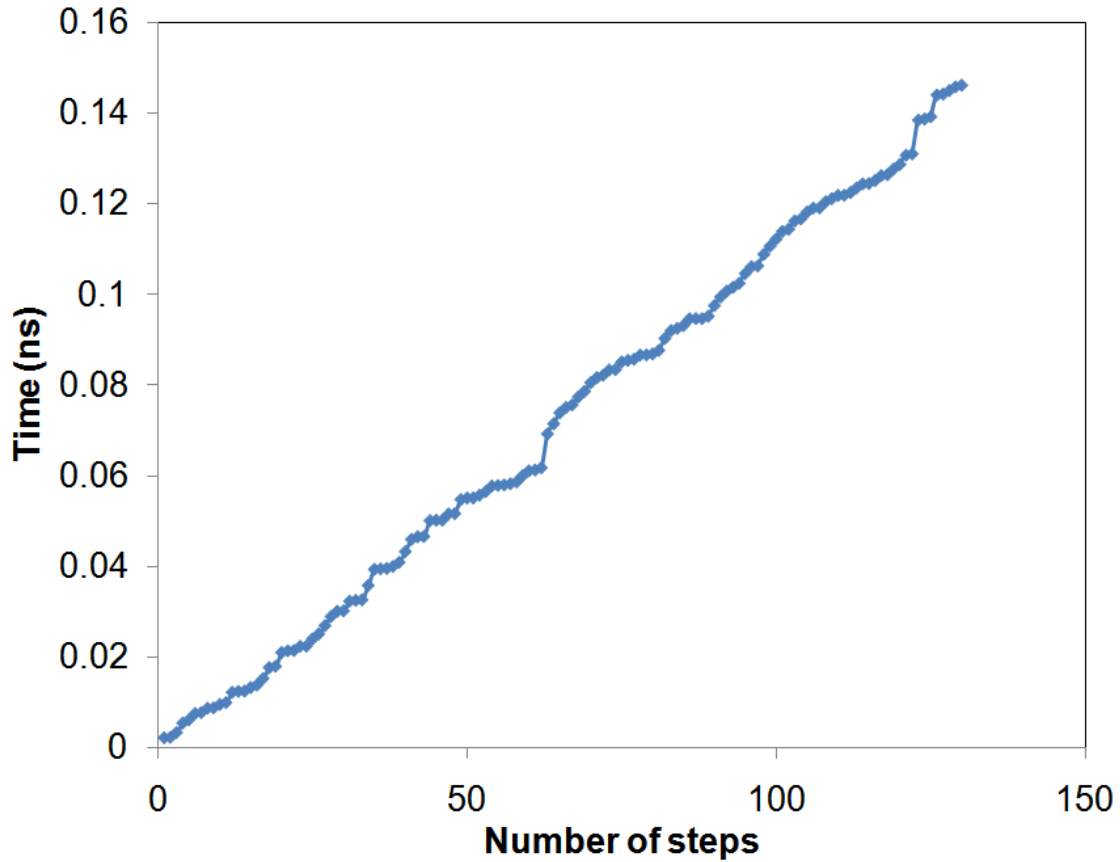


Figure 8-8. The evolution of time for AKMC simulation. 75 transition events occur until it reaches the 0.15 ns.

8.5 Conclusion

The AKMC code was developed and tested for a simple case. The AKMC code does not require the list of rates for the system, because it identifies for the transition states using the dimer method. The implemented dimer method was tested with a two-dimensional potential case. The dimer method successfully identifies possible transition states in the two-dimension potential. The AKMC code was tested with an Al adatom on the (111) Al surface. The AKMC code successfully searched the transition state and performed the trajectories of kinetic events. This work is an initial stage for studying the catalytic behavior on ZnO surface. Further work will combine the AKMC method with other complex potentials, so as to be able to describe other material systems.

CHAPTER 9 GENERAL CONCLUSIONS

Different levels of atomistic simulation methods have been successfully used to understand ferroelectric domain walls, organic-gas surfaces and organic-semiconductor interfaces. Also, an adaptive kinetic Monte Carlo (AKMC) code using dimer transition searching mechanism has been successfully developed in order to study catalytic activities on oxide surfaces.

9.1 Domain Walls

In this thesis, the structure and energetics of 180° domain walls of LiNbO_3 were analyzed using electronic and atomic level simulations. The energetics of two structurally distinct domain walls showed that Y-walls, parallel to c-glide plane, were more favorable than X-walls, perpendicular to c-glide plane. The comparison of activation energies of the two domain walls showed that the Y-wall is energetically less mobile than the X-wall. This energetics showed good agreement with the literature. In addition to the energy comparisons, the structural distinctions of two domain walls were addressed by evaluating atomic displacements near domain walls. Because of the different structural orientations, one Y-wall and two different X-walls were available. Both Y-wall and X-walls caused the atomic displacements along normal and transverse direction as well as longitudinal directions. These displacements resulted in additional polarization components normal to the domain wall (P_n) and transverse to the domain wall (P_t) along with the primary ferroelectric polarization (P_z). Thus, additional variations of polarization components are studied along with a kink-type variation of P_z . For the Y-wall, both of P_n and P_t were observed near the domain wall center. The maximum

magnitude of P_n and P_t was calculated to be $\sim 1.66 \mu\text{C}/\text{cm}^2$ and $0.60 \mu\text{C}/\text{cm}^2$ at the 2.58 \AA away from the Y-wall center. For X-walls, only normal polarization components were observed in addition to the primary ferroelectric polarization, because transverse components are cancelled by equal and opposite displacements of ions near X-walls. The maximum magnitude of P_n was observed to be $0.61 \mu\text{C}/\text{cm}^2$ and $0.71 \mu\text{C}/\text{cm}^2$ for two X-walls at 1.49 \AA away from the X-walls. The presence of P_n and P_t along with P_z required a simultaneous fitting to calculate the domain wall width. However, none of previously defined models were able to fit both components simultaneously. Thus, fits of P_z to single hyperbolic function yielded sharp domain wall width ($\sim 2.1 \text{ \AA}$) for both domain walls. A similar effect has recently observed in recent theoretical calculation in PbTiO_3 .

Defects play an important role for the properties of bulk ferroelectric materials. The structure and energetics of intrinsic [24] [78] and extrinsic defect [155] clusters in LiNbO_3 had been studied by density functional theory (DFT). The pinning of domain wall motion was observed by DFT study on oxygen vacancy-domain wall interactions in PbTiO_3 . [153] However, no study has been made for defects-domain wall interactions for LiNbO_3 . Thus, we performed a simulation study of defects/domain wall interactions using DFT and empirical methods. Our study showed the most of defects/domain wall interactions lowered the defect formation energy significantly. Particular defect structures, Li Frenkel and $\text{Nb}_{\text{Li}}^{\bullet\bullet\bullet\bullet} + 4V_{\text{Li}}'$ were considered. For the Li Frenkel pair, the parallel configuration was energetically more favorable than antiparallel configuration. The interaction between a Li Frenkel pair and domain walls lowered the formation energy by almost one-third for both a Y-wall and two X-walls. For $\text{Nb}_{\text{Li}}^{\bullet\bullet\bullet\bullet} + 4V_{\text{Li}}'$, however,

different energetics between Y-wall and two X-walls were observed. The formation energy of the parallel configurations was lowered by 0.24 eV/defect near a Y-wall; thereby, the parallel configuration was energetically favorable within entire regions across Y-wall. However, possible rearrangement of defect pair between parallel and antiparallel configurations was observed near X-walls. Also, X-walls showed higher defects-domain wall interactions, lowering defect formation energy of $Nb_{Li}^{\bullet\bullet\bullet\bullet} + 4V_{Li}'$ by 0.32 eV/defect, than Y-walls. Therefore, the $Nb_{Li}^{\bullet\bullet\bullet\bullet} + 4V_{Li}'$ defect cluster shows relative strong interaction with X-walls. When we considered the similarity in DFE between $LiNbO_3$ and $LiTaO_3$, we could expect that $Ta_{Li}^{\bullet\bullet\bullet\bullet} + 4V_{Li}'$ defects will also interact stronger with an X-wall than a Y-wall. This is the major reason for switching of stable domain wall direction for $LiTaO_3$. As the number of $Ta_{Li}^{\bullet\bullet\bullet\bullet} + 4V_{Li}'$ clusters increase, X-wall could be energetically favorable in $LiTaO_3$, which has only a small difference in domain wall energies.

The interactions of Y-walls with extrinsic Mg dopants were also studied. Several different reaction mechanisms were considered for the study. Consistent with intrinsic defect clusters, an Mg dopant pair also has a lower formation energy in the vicinity of Y-wall. However, the interactions were relatively weaker than for intrinsic defect pairs. Since defect-domain walls interactions caused the pinning effect of domain wall motion, weaker defect-domain wall interactions could improve the ferroelectric properties of $LiNbO_3$. Therefore, our study successfully supported better optical resistance and relatively lower cohesive and threshold field of Mg doped $LiNbO_3$ observed from experiments.

Similar studies were performed on $LiTaO_3$. Because an empirical potential for $LiTaO_3$ system was not available, we developed an empirical potential for $LiTaO_3$. The

new potential successfully captures the effect of temperature on ferroelectricity, in particular the ferroelectric to paraelectric transition as well as structural parameter and elastic properties of LiTaO_3 . The energetics of domain walls in LiTaO_3 showed the Y-wall was still energetically favorable for LiTaO_3 . However, the difference in energy between Y-wall and X-walls at the minimum energy state is small (3 mJ/m^2 for DFT and 10 mJ/m^2 for empirical) compared to LiNbO_3 (40 mJ/m^2 for DFT and 30 mJ/m^2 for empirical). In addition, the energetics on defects-domain wall interactions demonstrated that defects are more strongly interacting with X-walls than Y-wall. Therefore, the shift of preferred domain wall direction from Y-wall to X-wall in Li deficient congruent LiTaO_3 could be explained by defects/X-wall interactions, which overcome the energy difference between Y-wall and X-wall.

9.2 Organic-Gas Interface

Collision induced chemical reactions at organic-gas interface were also investigated. Using DFT-MD methods, detailed processes for four different reaction mechanisms were revealed. The results provide insights regarding reactions between organic molecules and predict how surface polymerization by ion-assisted deposition (SPIAD) influences the polymerization and crosslinking process of polythiophene.

The mechanism of surface polymerization of terthiophene oligomers was simulated using thiophene incident molecules. The DFT-MD simulations predicted incident thiophenes having 25 eV kinetic energy could possibly yield surface reactions with a low probability (less than 30%). The increase in the kinetic energy of incident thiophene to 35 eV could break the C-C bonds of polythiophene and led to different surface reactions for polythiophenes. Further increases in the kinetic energy caused the damage to polythiophene and formed debris from the collision. The mechanism for

polymerization and crosslinking of polythiophene was understood as a two step processes; breaking C-S bonds of polythiophenes and creating stable C-C bonds. Based on this mechanism, four different reaction processes were observed; polymerization, crosslinking, branched polymer and active state with broken C-S bond. Each reaction showed different probability.

In a similar manner, bonding chemistry at organic-semiconductor interface was also investigated. The incident C_2H^+ molecule with 100 eV kinetic energy was deposited into the PbS nanocrystalline embedded in polythiophenes. The study on charge density distribution across the interface between thiophene and PbS quantum dot showed possible mechanism for creation of bonds. After the collision, a C-S bond from dithiophene were broken and created a new bond with incident particle. This new bond produced the electronic connection between PbS nanocrystalline and polythiophene. Therefore breaking C-S bonds of polythiophenes was a key mechanism for reaction of polythiophenes.

9.3 Metal-gas Interface

Surface diffusion of Al adatom on Al (111) surface was studied with a newly developed AKMC code. Two different sites were available for Al adatom on (111) surface. The study with Lennard-Jones potential obtained from literature showed the energy difference between two different sites was 0.002 eV. AKMC simulations were performed to understand diffusion process of an Al adatom on Al (111) surface. Our study showed that only one transition state was available for surface diffusion of an Al adatom. So, the study yielded two different activation energies and four different diffusion processes. As we denoted two different positions of an adatom as A and B, the activation energy for leaving two sites was 0.100 eV for site A and 0.102 eV for site B. Four different diffusion

processes were A to A, A to B, B to A and B to B. This study will be expanded to understand catalytic activity on ZnO₂ surface.

LIST OF REFERENCES

- [1] C. R. Barrett, W. D. Nix, and A. S. Tetelman, *The Principles of Engineering Materials*. New Jersey: Prentice Hall, 1973.
- [2] R. M. Martin, *Electronic Structure: Basic Theory and Practical Methods* New York: Cambridge University Press, 2004.
- [3] E. Schrodinger, "An undulatory theory of the mechanics of atoms and molecules," *Physical Review*, vol. 28, pp. 1049-1070, 1926.
- [4] M. Born and R. Oppenheimer, "Quantum theory of molecules," *Annalen Der Physik*, vol. 84, pp. 0457-0484, 1927.
- [5] J. C. Slater, "The theory of complex spectra," *Physical Review*, vol. 34, pp. 1293-1322, 1929.
- [6] D. S. Scholl and J. A. Steckel, *Density Functional Theory: A Practical Introduction*. Hoboken, New Jersey: John Wiley & Sons, Inc., 2009.
- [7] P. Hohenberg and W. Kohn, "Inhomogeneous Electron Gas," *Phys. Rev.*, vol. 136, pp. B864-B871, 1964.
- [8] W. Kohn and L. J. Sham, "Self-Consistent Equations Including Exchange And Correlation Effects," *Phys. Rev.*, vol. 140, pp. A1133-A1138, 1965.
- [9] C. J. Cramer, "Essentials of Computational Chemistry: Theories and Models," Second Edition ed: John Wiley & Sons, Ltd, 2004.
- [10] J. P. Perdew, "Accurate Density Functional for the Energy: Real-Space Cutoff of the Gradient Expansion for the Exchange Hole," *Phys. Rev. Lett.*, vol. 55, pp. 1665-1668, 1985.
- [11] N. W. Ashcroft and N. D. Mermin, *Solid State Physics*. New York: Holt, Rinehart and Winston, 1976.
- [12] H. J. Monkhorst and J. D. Pack, "Special points for Brillouin-zone integrations," *Phys. Rev. B*, vol. 13, pp. 5188-5192, 1976.
- [13] S. F. Boys, "Electronic wave functions .1. A general method of calculation for the stationary states of any molecular system," *Proceedings of the Royal Society of London Series a-Mathematical and Physical Sciences*, vol. 200, pp. 542-554, 1950.
- [14] G. Kresse and J. Furthmuller, "Efficiency of ab-initio total energy calculations for metals and semiconductors using a plane-wave basis set," *Comp. Mater. Sci.*, vol. 6, pp. 15-50, 1996.

- [15] G. Kresse and J. Furthmüller, "Efficient iterative schemes for ab initio total-energy calculations using a plane-wave basis set," *Phys. Rev. B*, vol. 54, pp. 11169-11186, 1996.
- [16] D. Vanderbilt, "Soft self-consistent pseudopotentials in a generalized eigenvalue formalism," *Phys. Rev. B*, vol. 41, pp. 7892-7895, 1990.
- [17] P. E. Blochl, "PROJECTOR AUGMENTED-WAVE METHOD," *Phys. Rev. B*, vol. 50, pp. 17953-17979, 1994.
- [18] G. Kresse and J. Joubert, "From Ultrasoft Pseudopotentials to the Projector Augmented-Wave Method," *Phys. Rev. B*, vol. 59, pp. 1758-1775, 1999.
- [19] D. Lee, H. X. Xu, V. Dierolf, V. Gopalan, and S. R. Phillpot, "Structure and energetics of ferroelectric domain walls in LiNbO₃ from atomic-level simulation," *Phys. Rev. B*, p. to be Submitted, 2010.
- [20] J. P. Perdew and W. Yue, "Accurate And Simple Density Functional For The Electronic Exchange Energy - Generalized Gradient Approximation," *Phys. Rev. B*, vol. 33, pp. 8800-8802, 1986.
- [21] Q. K. Li, B. Wang, C. H. Woo, H. Wang, and R. Wang, "First-principles study on the formation energies of intrinsic defects in LiNbO₃," *J. Phys. Chem. Solids*, vol. 68, pp. 1336-1340, 2007.
- [22] M. P. Teter, M. C. Payne, and D. C. Allan, "Solution Of Schrodinger-Equation For Large Systems," *Phys. Rev. B*, vol. 40, pp. 12255-12263, 1989.
- [23] P. Pulay, "Convergence Acceleration Of Iterative Sequences - The Case Of Scf Iteration," *Chem. Phys. Lett.*, vol. 73, pp. 393-398, 1980.
- [24] H. X. Xu, D. Lee, J. He, S. B. Sinnott, V. Gopalan, V. Dierolf, and S. R. Phillpot, "Stability of intrinsic defects and defect clusters in LiNbO₃ from density functional theory calculations," *Phys. Rev. B*, vol. 78, p. 174103, Nov 2008.
- [25] N. Troullier and J. L. Martins, "Efficient Pseudopotentials for Plane-Wave Calculations," *Physical Review B*, vol. 43, pp. 1993-2006, Jan 15 1991.
- [26] J. M. Soler, E. Artacho, J. D. Gale, A. Garcia, J. Junquera, P. Ordejon, and D. Sanchez-Portal, "The SIESTA method for ab initio order-N materials simulation," *Journal of Physics: Condensed Matter*, vol. 14, pp. 2745-2779, 2002.
- [27] G. D. Purvis and R. J. Bartlett, "A Full Coupled-Cluster Singles and Doubles Model - the Inclusion of Disconnected Triples," *Journal of Chemical Physics*, vol. 76, pp. 1910-1918, 1982.

- [28] T. H. Dunning, "Gaussian-Basis Sets for Use in Correlated Molecular Calculations .1. The Atoms Boron through Neon and Hydrogen," *Journal of Chemical Physics*, vol. 90, pp. 1007-1023, Jan 15 1989.
- [29] J. A. Pople, M. Headgordon, and K. Raghavachari, "Quadratic Configuration-Interaction - a General Technique for Determining Electron Correlation Energies," *Journal of Chemical Physics*, vol. 87, pp. 5968-5975, Nov 15 1987.
- [30] R. S. Mulliken, "Electronic Population Analysis On Lcao-Mo Molecular Wave Functions .1," *J. Chem. Phys.*, vol. 23, pp. 1833-1840, 1955.
- [31] J. P. Foster and F. Weinhold, "Natural Hybrid Orbitals," *J. Am. Chem. Soc.*, vol. 102, pp. 7211-7218, 1980.
- [32] P. O. Lowdin, "On The Non-Orthogonality Problem Connected With The Use Of Atomic Wave Functions In The Theory Of Molecules And Crystals," *J. Chem. Phys.*, vol. 18, pp. 365-375, 1950.
- [33] R. F. W. Bader and T. T. Nguyendang, "Quantum-Theory Of Atoms In Molecules - Dalton Revisited," *Adv. Quantum Chem.*, vol. 14, pp. 63-124, 1981.
- [34] G. Henkelman, A. Arnaldsson, and H. Jonsson, "A fast and robust algorithm for Bader decomposition of charge density," *Comp. Mater. Sci.*, vol. 36, pp. 354-360, Jun 2006.
- [35] E. Sanville, S. D. Kenny, R. Smith, and G. Henkelman, "Improved grid-based algorithm for Bader charge allocation," *J. Comput. Chem.*, vol. 28, pp. 899-908, 2007.
- [36] W. Tang, E. Sanville, and G. Henkelman, "A grid-based Bader analysis algorithm without lattice bias," *J. Phys. Condens. Matter*, vol. 21, p. 084204, 2009.
- [37] A. J. Cohen, P. Mori-Sanchez, and W. T. Yang, "Insights into current limitations of density functional theory," *Science*, vol. 321, pp. 792-794, 2008.
- [38] Y. K. Zhang and W. T. Yang, "A challenge for density functionals: Self-interaction error increases for systems with a noninteger number of electrons," *J. Chem. Phys.*, vol. 109, pp. 2604-2608, 1998.
- [39] P. Mori-Sanchez, Q. Wu, and W. T. Yang, "Accurate polymer polarizabilities with exact exchange density-functional theory," *J. Chem. Phys.*, vol. 119, pp. 11001-11004, 2003.

- [40] C. Toher, A. Filippetti, S. Sanvito, and K. Burke, "Self-interaction errors in density-functional calculations of electronic transport," *Phys. Rev. Lett.*, vol. 95, 2005.
- [41] S. H. Ke, H. U. Baranger, and W. T. Yang, "Role of the exchange-correlation potential in ab initio electron transport calculations," *J. Chem. Phys.*, vol. 126, 2007.
- [42] S. Grimme, J. Antony, T. Schwabe, and C. Muck-Lichtenfeld, "Density functional theory with dispersion corrections for supramolecular structures, aggregates, and complexes of (bio)organic molecules," *Organic & Biomolecular Chemistry*, vol. 5, pp. 741-758, 2007.
- [43] R. C. Albers, N. E. Christensen, and A. Svane, "Hubbard-U band-structure methods," *J. Phys. Condens. Matter*, vol. 21, 2009.
- [44] A. J. Cohen, P. Mori-Sanchez, and W. T. Yang, "Development of exchange-correlation functionals with minimal many-electron self-interaction error," *J. Chem. Phys.*, vol. 126, 2007.
- [45] M. P. Allen and D. J. Tildesley, *Computer Simulation of Liquids*, First ed. New York: Oxford University Press Inc., 1987.
- [46] D. Wolf, P. Keblinski, S. R. Phillpot, and J. Eggebrecht, "Exact method for the simulation of Coulombic systems by spherically truncated, pairwise r^{-1} summation," *J. Chem. Phys.*, vol. 110, pp. 8254-8282, May 1999.
- [47] R. A. Buckingham, "The classical equation of state of gaseous helium, neon and argon," *Proceedings of the Royal Society of London Series a-Mathematical and Physical Sciences*, vol. 168, pp. 264-283, 1938.
- [48] J. E. Jones, "On the determination of molecular fields - II From the equation of state of a gas," *Proceedings of the Royal Society of London Series a-Containing Papers of a Mathematical and Physical Character*, vol. 106, pp. 463-477, 1924.
- [49] P. M. Morse, "Diatomic molecules according to the wave mechanics. II. Vibrational levels," *Physical Review*, vol. 34, pp. 57-64, 1929.
- [50] R. S. Chhikara and L. Folks, *The Inverse Gaussian Distribution: Theory, Methodology, and Applications. Statistics, textbooks and monographs* vol. 95. New York: M. DEKKER, 1989.
- [51] K. T. Tang and J. P. Toennies, "An Improved Simple-Model For The Vanderwaals Potential Based On Universal Damping Functions For The Dispersion Coefficients," *J. Chem. Phys.*, vol. 80, pp. 3726-3741, 1984.

- [52] Y. P. Varshni, "Comparative Study Of Potential Energy Functions For Diatomic Molecules," *Reviews of Modern Physics*, vol. 29, pp. 664-682, 1957.
- [53] R. A. Jackson and M. E. G. Valerio, "A new interatomic potential for the ferroelectric and paraelectric phases of LiNbO₃," *J. Phys. Condens. Matter*, vol. 17, pp. 837-843, Feb 2005.
- [54] L. Verlet, "Computer "Experiments" on Classical Fluids. I. Thermodynamical Properties of Lennard-Jones Molecules," *Physical Review*, vol. 159, pp. 98-103, 1967.
- [55] S. Toxvaerd, "Molecular-Dynamics At Constant Temperature And Pressure," *Physical Review E*, vol. 47, pp. 343-350, 1993.
- [56] D. Beeman, "Some Multistep Methods For Use In Molecular-Dynamics Calculations," *Journal of Computational Physics*, vol. 20, pp. 130-139, 1976.
- [57] C. W. Gear, *Numerical Initial Value Problems in Ordinary Differential Equations*. Englewood Cliffs, NJ: Prentice-Hall, 1971.
- [58] M. E. Tuckerman and G. J. Martyna, "Understanding modern molecular dynamics: Techniques and applications," *J. Phys. Chem. B*, vol. 104, pp. 159-178, 2000.
- [59] M. P. Allen and D. J. Tildesley, *Computer Simulation of Liquids*. Oxford: Oxford Science, 2004.
- [60] D. G. Luenberger and Y. Ye, *Linear and Nonlinear Programming*, Third ed. New York: Springer Science+Business media, LLC, 2008.
- [61] M. Parrinello and A. Rahman, "Crystal Structure and Pair Potentials: A Molecular-Dynamics Study," *Phys. Rev. Lett.*, vol. 45, pp. 1196-1199, 1980.
- [62] M. Parrinello and A. Rahman, "Strain fluctuations and elastic constants," *J. Chem. Phys.*, vol. 76, pp. 2662-2666, 1982.
- [63] H. C. Andersen, "Molecular dynamics simulations at constant pressure and/or temperature," *J. Chem. Phys.*, vol. 72, pp. 2384-2393, 1980.
- [64] S. Nosé, "A unified formulation of the constant temperature molecular-dynamics methods," *J. Chem. Phys.*, vol. 81 pp. 511-519, 1984.
- [65] W. G. Hoover, "Canonical Dynamics - Equilibrium Phase-Space Distributions," *Physical Review A* vol. 31, pp. 1695-1697, 1985.

- [66] H. J. C. Berendsen, J. P. M. Postma, W. F. v. Gunsteren, A. DiNola, and J. R. Haak, "Molecular dynamics with coupling to an external bath," *J. Chem. Phys.*, vol. 81 pp. 3684-3690, 1984.
- [67] S. A. Adelman and J. D. Doll, "Generalized Langevin Equation Approach for Atom/Solid-Surface Scattering: Collinear Atom/Harmonic Chain Model," *J. Chem. Phys.*, vol. 61, pp. 4242-4245, 1974.
- [68] S. A. Adelman and J. D. Doll, "Generalized Langevin Equation Approach for Atom-Solid-Surface Scattering - General Formulation for Classical Scattering Off Harmonic Solids," *J. Chem. Phys.*, vol. 64, pp. 2375-2388, 1976.
- [69] K. K. Wong, *Properties of Lithium Niobate*. London: INSPEC, The Institution of Electrical Engineers, United Kingdom, 2002.
- [70] T. Volk and M. Wöhlecke, *Lithium Niobate: Defects, Photorefraction and Ferroelectric Switching*. Berlin: Springer, 2008.
- [71] P. F. Bordui, R. G. Norwood, D. H. Jundt, and M. M. Fejer, "Preparation And Characterization Of Off-Congruent Lithium-Niobate Crystals," *J. Appl. Phys.*, vol. 71, pp. 875-879, 1992.
- [72] Y. H. Han and D. M. Smyth, "Nonstoichiometry And Defects In Linbo3," *American Ceramic Society Bulletin*, vol. 62, pp. 852-852, 1983.
- [73] H. M. Obryan, P. K. Gallagher, and C. D. Brandle, "Congruent Composition And Li-Rich Phase-Boundary Of Linbo3," *Journal of the American Ceramic Society*, vol. 68, pp. 493-496, 1985.
- [74] N. Iyi, K. Kitamura, F. Izumi, J. K. Yamamoto, T. Hayashi, H. Asano, and S. Kimura, "Comparative-Study Of Defect Structures In Lithium-Niobate With Different Compositions," *Journal of Solid State Chemistry*, vol. 101, pp. 340-352, 1992.
- [75] W. Bollmann, "Stoichiometry And Point-Defects In Lithium-Niobate Crystals," *Crystal Research and Technology*, vol. 18, pp. 1147-1149, 1983.
- [76] O. F. Schirmer, O. Thiemann, and M. Wohlecke, "Defects in linbo3 .1. Experimental aspects," *J. Phys. Chem. Solids*, vol. 52, pp. 185-200, 1991.
- [77] H. Donnerberg, S. M. Tomlinson, C. R. A. Catlow, and O. F. Schirmer, "Computer-Simulation Studies Of Intrinsic Defects In Linbo3 Crystals," *Phys. Rev. B*, vol. 40, pp. 11909-11916, Dec 1989.

- [78] H. X. Xu, D. Lee, S. B. Sinnott, V. Dierolf, V. Gopalan, and S. R. Phillpot, "Structure and diffusion of intrinsic defect complexes in LiNbO₃ from density functional theory calculations," *J. Phys. Condens. Matter*, vol. 22, 2010.
- [79] R. M. Araujo, K. Lengyel, R. A. Jackson, L. Kovacs, and M. E. G. Valerio, "A computational study of intrinsic and extrinsic defects in LiNbO₃," *J. Phys. Condens. Matter*, vol. 19, 2007.
- [80] V. Gopalan, V. Dierolf, and D. A. Scrymgeour, "Defect-domain wall interactions in trigonal ferroelectrics," *Ann. Rev. Mater. Res.*, vol. 37, pp. 449-489, 2007.
- [81] P. Paufler, "Complete online set of International tables for crystallography," *Acta Crystallogr., Sect. A: Found. Crystallogr.*, vol. 63(6), p. 483, 2007.
- [82] H. Boysen and F. Altorfer, "A Neutron Powder Investigation Of The High-Temperature Structure And Phase-Transition In Linbo₃," *Acta Crystallogr., Sect. B: Struct. Sci*, vol. 50, pp. 405-414, 1994.
- [83] K. Parlinski and Z. Q. Li, "Ab initio calculations of phonons in LiNbO₃," *Phys. Rev. B*, vol. 61, pp. 272-278, 2000.
- [84] A. V. Postnikov, V. Caciuc, and G. Borstel, "Structure optimization and frozen phonons in LiNbO₃," *J. Phys. Chem. Solids*, vol. 61, pp. 295-299, 2000.
- [85] M. Veithen and P. Ghosez, "First-principles study of the dielectric and dynamical properties of lithium niobate," *Phys. Rev. B*, vol. 65, p. 214302, 2002.
- [86] I. U. o. Crystallography, *International tables for crystallography*. New York: Springer, 2006.
- [87] S. C. Abrahams, J. M. Reddy, and Bernstein, JI, "Ferroelectric lithium niobate .3. Single crystal x-ray diffraction study at 24 degrees c," *J. Phys. Chem. Solids*, vol. 27, pp. 997-&, 1966.
- [88] H. D. Megaw, "A Note On Structure Of Lithium Niobate Linbo₃," *Acta Crystallogr., sect. A: Cryst. Phys., Diffr., Theor. Gen. Crystallogr.*, vol. A 24, pp. 583-&, 1968.
- [89] S. C. Abrahams, Levinste.Hj, and J. M. Reddy, "Ferroelectric lithium niobate .5. Polycrystal x-ray diffraction study between 24 degrees and 1200 degrees c," *J. Phys. Chem. Solids*, vol. 27, pp. 1019-&, 1966.
- [90] A. M. Glazer, "Simple Ways Of Determining Perovskite Structures," *Acta Crystallogr. Sect. A*, vol. 31, pp. 756-762, 1975.
- [91] H. D. Megaw, *Crystal structures - a working approach*. Philadelphia: W. B. Saunders, 1973.

- [92] H. Landolt and R. Börnstein, *Numerical Data and Functional Relations in Science and Technology* vol. 15a. Berlin: Springer, 1981.
- [93] S. R. Phillpot and V. Gopalan, "Coupled displacive and order-disorder dynamics in LiNbO₃ by molecular-dynamics simulation," *Appl. Phys. Lett.*, vol. 84, pp. 1916-1918, Mar 2004.
- [94] O. Auciello, J. F. Scott, and R. Ramesh, "The physics of ferroelectric memories," *Physics Today*, vol. 51, pp. 22-27, Jul 1998.
- [95] A. J. Moulson and J. M. Herbert, *Electroceramics : materials, properties, applications*, Second ed. New York: Wiley, J., 2003.
- [96] D. A. Scrymgeour, V. Gopalan, A. Itagi, A. Saxena, and P. J. Swart, "Phenomenological theory of a single domain wall in uniaxial trigonal ferroelectrics: Lithium niobate and lithium tantalate," *Phys. Rev. B*, vol. 71, p. 184110, May 2005.
- [97] H. S. Nalwa, *Handbook of Organic Conductive Molecules and Polymers*. Chichester: Wiley, 1997.
- [98] T. A. Skotheim, R. L. Elsenbaumer, and J. R. Reynolds, *Handbook of Conducting Polymers*. New York: M. Dekker, 1998.
- [99] F. Jonas and G. Heywang, "Technical applications for conductive polymers," *Electrochim. Acta*, vol. 39, pp. 1345-1347, 1994.
- [100] S. Ghosh and O. Ingan, "Conducting Polymer Hydrogels as 3D Electrodes: Applications for Supercapacitors," *Adv. Mater.*, vol. 11, pp. 1214-1218, 1999.
- [101] M. Gerard, A. Chaubey, and B. D. Malhotra, "Application of conducting polymers to biosensors," *Biosens. Bioelectron.*, vol. 17, pp. 345-359, 2002.
- [102] C. Pratt, "Conducting Polymers," <http://homepage.ntlworld.com/colin.pratt/cpoly.pdf>, 1996.
- [103] D. Fichou, "Handbook of Oligo- and Polythiophenes," Wiley-VCH: Weinheim, 1999.
- [104] A. J. Heeger, "Semiconducting and metallic polymers: The fourth generation of polymeric materials," *J. Phys. Chem. B*, vol. 105, pp. 8475-8491, 2001.
- [105] S. Tepavcevic, Y. Choi, and L. Hanley, "Surface polymerization by ion-assisted deposition for polythiophene film growth," *J. Am. Chem. Soc.*, vol. 125, pp. 2396-2397, 2003.

- [106] G. Tourillon, "Conjugate polymers: processing and applications," in *Handbook of Conducting Polymers*, Third ed. vol. 1, T. A. Skotheim and J. R. Reynolds, Eds.: CRC Press, Taylor & Francis Group, LLC, 2007, p. 293.
- [107] A. J. Heeger, D. Moses, and M. Sinclair, "Nonlinear Excitations And Nonlinear Phenomena In Conductive Polymers," *ACS Symp. Ser.*, vol. 346, pp. 372-380, 1987.
- [108] F. Vanbolhuis, H. Wynberg, E. E. Havinga, E. W. Meijer, and E. G. J. Staring, "The X-Ray Structure And Mndo Calculations Of Alpha-Terthienyl - A Model For Polythiophenes," *Synth. Met.*, vol. 30, pp. 381-389, 1989.
- [109] G. J. Ashwell, *Molecular Electronics*. Taunton, Somerset, England: Research Studies Press, 1992.
- [110] L. Alcácer, *Conducting Polymers; Special Applications : Proceedings of the Workshop Held at Sintra Portugal, July 28-31, 1986*. Dordrecht: D. Reidel, 1987.
- [111] G. A. Inzelt, *Conducting Polymers*. New York: Springer, 2008.
- [112] B. J. Schwartz, "Conjugated polymers as molecular materials : How chain conformation and film morphology influence energy transfer and interchain interactions," *Annu. Rev. Phys. Chem.*, vol. 54, pp. 141-172, 2003.
- [113] J. R. Sheats, "Manufacturing and commercialization issues in organic electronics," *J. Mater. Res.*, vol. 19, pp. 1974-1989, 2004.
- [114] Y. S. Choi, S. Tepavcevic, Z. Xu, and L. Hanley, "Optical and chemical properties of polythiophene films produced via surface polymerization by ion-assisted deposition," *Chem. Mater.*, vol. 16, pp. 1924-1931, 2004.
- [115] S. Tepavcevic, Y. Choi, and L. Hanley, "Growth of novel polythiophene and polyphenyl films via surface polymerization by ion-assisted deposition," *Langmuir*, vol. 20, pp. 8754-8761, 2004.
- [116] Y. Choi, A. Zachary, S. Tepavcevic, C. P. Wu, and L. Hanley, "Polyatomicity and kinetic energy effects on surface polymerization by ion-assisted deposition," *Int. J. Mass spectrom.*, vol. 241, pp. 139-147, 2005.
- [117] S. Tepavcevic, A. T. Wroble, M. Bissen, D. J. Wallace, Y. Choi, and L. Hanley, "Photoemission studies of polythiophene and polyphenyl films produced via surface polymerization by ion-assisted deposition," *J. Phys. Chem. B*, vol. 109, pp. 7134-7140, 2005.

- [118] J. W. Shen, C. Evans, N. Wade, and R. G. Cooks, "Ion-ion collisions leading to formation of C-C bonds at surfaces: An interfacial Kolbe reaction," *J. Am. Chem. Soc.*, vol. 121, pp. 9762-9763, 1999.
- [119] N. Wade, C. Evans, S. C. Jo, and R. G. Cooks, "Silylation of an OH-terminated self-assembled monolayer surface through low-energy collisions of ions: a novel route to synthesis and patterning of surfaces," *J. Mass Spectrom.*, vol. 37, pp. 591-602, 2002.
- [120] H. Usui, "Polymeric film deposition by ionization-assisted method for optical and optoelectronic applications," *Thin Solid Films*, vol. 365, pp. 22-29, 2000.
- [121] J. Y. Kim, E. S. Kim, and J. H. Choi, "Poly[2-(N-carbazolyl)-5-(2-ethylhexyloxy)-1,4-phenylenevinylene]/tris(8-hydroxyquinoline) aluminum heterojunction electroluminescent devices produced by cluster beam deposition methods," *J. Appl. Phys.*, vol. 91, pp. 1944-1951, 2002.
- [122] L. Hanley, Y. Choi, and S. Tepavcevic, *Materials Research Society Symposium Proceeding*, pp. 804, JJ5.3.1-JJ5.3.6, 2004.
- [123] I. Jang, B. Ni, and S. B. Sinnott, "Study of angular influence of C₃H₅⁺ ion deposition on polystyrene surfaces using molecular dynamics simulations," *Journal of Vacuum Science & Technology a-Vacuum Surfaces and Films*, vol. 20, pp. 564-568, 2002.
- [124] D. G. Lim, B. S. Jang, S. I. Moon, C. Y. Won, and J. Yi, "Characteristics of LiNbO₃ memory capacitors fabricated using a low thermal budget process," *Solid-State Electronics*, vol. 45, pp. 1159-1163, 2001.
- [125] J. Macario, P. Yao, R. Shireen, C. A. Schuetz, S. Y. Shi, and D. W. Prather, "Development of Electro-Optic Phase Modulator for 94 GHz Imaging System," *J. Lightwave Technol.*, vol. 27, pp. 5698-5703, 2009.
- [126] A. Tehranchi and R. Kashyap, "Efficient wavelength converters with flattop responses based on counterpropagating cascaded SFG and DFG in low-loss QPM LiNbO₃ waveguides," *Optics Express*, vol. 17, pp. 19113-19119, 2009.
- [127] A. M. Prokhorov and Y. S. Kuz'minov, *Physics and Chemistry of Crystalline Lithium Niobate* Taylor & Francis, 1990.
- [128] L. Arizmendi, "Photonic applications of lithium niobate crystals," *Phys. Status Solidi A-Appl. Res.*, vol. 201, pp. 253-283, Jan 2004.

- [129] V. Gopalan, M. J. Kavas, M. C. Gupta, T. E. Schlesinger, and D. D. Stancil, "Integrated quasi-phase-matched second-harmonic generator and electrooptic scanner on LiTaO₃ single crystals," *IEEE Photonics Technol. Lett.*, vol. 8, pp. 1704-1706, Dec 1996.
- [130] V. Soluch and M. Lysakowska, "Surface acoustic waves on X-cut LiNbO₃," *IEEE Trans. Ultrason. Ferroelectr. Freq. Control*, vol. 52, pp. 145-147, Jan 2005.
- [131] J. Padilla, W. Zhong, and D. Vanderbilt, "First-principles investigation of 180 degrees domain walls in BaTiO₃," *Phys. Rev. B*, vol. 53, pp. R5969-R5973, Mar 1996.
- [132] A. Goldman, *The Handbook of Modern Ferromagnetic Materials* 1st edition ed. New York: Springer, 1999.
- [133] B. Meyer and D. Vanderbilt, "Ab initio study of ferroelectric domain walls in PbTiO₃," *Phys. Rev. B*, vol. 65, p. 104111, 2002.
- [134] K. C. Kao, *Dielectric Phenomena in Solids* 1st edition ed. New York: Academic Press, 2004.
- [135] D. Lee, R. K. Behera, P. Wu, H. X. Xu, S. B. Sinnott, S. R. Phillpot, L. Q. Chen, and V. Gopalan, "Mixed Bloch-Néel-Ising character of 180° ferroelectric domain walls," *Phys. Rev. B*, vol. 80, p. 060102(R), August 2009.
- [136] A. F. Devonshire, "Theory Of Barium Titanate .2," *Philos. Mag.*, vol. 42, pp. 1065-1079, 1951.
- [137] V. A. Zhirnov, "A Contribution To The Theory Of Domain Walls In Ferroelectrics," *Zh. Eksp. Teor. Fiz.*, vol. 35, p. 1175, 1958.
- [138] V. L. Ginzburg, "Some Remarks On Phase Transitions Of The 2nd Kind And The Microscopic Theory Of Ferroelectric Materials," *Fiz. Tverd. Tela*, vol. 2, p. 2031, 1960.
- [139] F. Jona and G. Shirane, *Ferroelectric crystals*. Oxford: Pergamon Press, 1962.
- [140] L. N. Bulaevskii, "Thermodynamic Theory Of Domain Walls In Ferroelectric Materials With The Perovskite Structure," *Fiz. Tverd. Tela (St. Petersburg)*, vol. 5, p. 3183, 1963.
- [141] Y. Ishibashi, "Computational Method Of Activation-Energy Of Thick Domain-Walls," *J. Phys. Soc. Jpn.*, vol. 46, pp. 1254-1257, 1979.

- [142] Y. Ishibashi and I. Suzuki, "The Structure, The Formation And The Activation-Energies Of A Domain-Wall In Crystals Undergoing The 1st Order Transition," *J. Phys. Soc. Jpn.*, vol. 53, pp. 1093-1096, 1984.
- [143] S. Choudhury, Y. L. Li, N. Odagawa, A. Vasudevarao, L. Tian, P. Capek, V. Dierolf, A. N. Morozovska, E. A. Eliseev, S. Kalinin, Y. S. Cho, L. Q. Chen, and V. Gopalan, "The influence of 180 degrees ferroelectric domain wall width on the threshold field for wall motion," *J. Appl. Phys.*, vol. 104, p. 084107, 2008.
- [144] M. Leslie and M. J. Gillan, "The Energy And Elastic Dipole Tensor Of Defects In Ionic-Crystals Calculated By The Supercell Method," *Journal of Physics C-Solid State Physics*, vol. 18, pp. 973-982, 1985.
- [145] M. F. Mott and M. J. Littleton, "Conduction in polar crystals. I. Electrolytic conduction in solid salts," *Transactions of the Faraday Society*, vol. 34, pp. 0485-0499, 1938.
- [146] C. G. Van de Walle and J. Neugebauer, "First-principles calculations for defects and impurities: Applications to III-nitrides," *Journal of Applied Physics*, vol. 95, pp. 3851-3879, Apr 15 2004.
- [147] K. Reuter and M. Scheffler, "Composition, structure, and stability of RuO₂(110) as a function of oxygen pressure," *Physical Review B*, vol. 65, pp. -, Jan 15 2002.
- [148] J. He, R. K. Behera, M. W. Finnis, X. Li, E. C. Dickey, S. R. Phillpot, and S. B. Sinnott, "Prediction of high-temperature point defect formation in TiO₂ from combined ab initio and thermodynamic calculations," *Acta Materialia*, vol. 55, pp. 4325-4337, Aug 2007.
- [149] A. F. Kohan, G. Ceder, D. Morgan, and C. G. Van de Walle, "First-principles study of native point defects in ZnO," *Physical Review B*, vol. 61, pp. 15019-15027, Jun 1 2000.
- [150] I. P. Zibrov, V. P. Filonenko, P. E. Werner, B. O. Marinder, and M. Sundberg, "A new high-pressure modification of Nb₂O₅," *Journal of Solid State Chemistry*, vol. 141, pp. 205-211, Nov 15 1998.
- [151] J. B. Goodenough and A. Hamnett, *Physics of Non-Tetrahedrally Bonded Binary Compounds III*. Berlin: Springer-Verlag, 1984.
- [152] S. Kim, V. Gopalan, K. Kitamura, and Y. Furukawa, "Domain reversal and nonstoichiometry in lithium tantalate," *J. Appl. Phys.*, vol. 90, pp. 2949-2963, 2001.
- [153] L. X. He and D. Vanderbilt, "First-principles study of oxygen-vacancy pinning of domain walls in PbTiO₃," *Phys. Rev. B*, vol. 68, 2003.

- [154] H. Donnerberg, S. M. Tomlinson, C. R. A. Catlow, and O. F. Schirmer, "Computer-Simulation Studies Of Extrinsic Defects In Linbo3 Crystals," *Phys. Rev. B*, vol. 44, pp. 4877-4883, 1991.
- [155] H. X. Xu, D. Lee, S. B. Sinnott, V. Gopalan, V. Dierolf, and S. R. Phillpot, "Structure and energetics of Er defects in LiNbO3 from first-principles and thermodynamic calculations," *Phys. Rev. B*, vol. 80, 2009.
- [156] F. Abdi, M. Aillerie, P. Bourson, and M. D. Fontana, "Defect structure in Mg-doped LiNbO3: Revisited study," *J. Appl. Phys.*, vol. 106, 2009.
- [157] H. Z. Jin and J. Zhu, "Size effect and fatigue mechanism in ferroelectric thin films," *J. Appl. Phys.*, vol. 92, pp. 4594-4598, Oct 2002.
- [158] B. S. Razbirin, "Curie Temperature Of The Ferroelectric Litao3 Edge Luminescence Of Crystals," *Soviet Physics-Solid State*, vol. 6, pp. 254-255, 1964.
- [159] S. H. Wemple, Didomeni.M, and I. Camlibel, "Relationship Between Linear And Quadratic Electro-Optic Coefficients In Linbo3 Litao3 And Other Oxygen-Octahedra Ferroelectrics Based On Direct Measurement Of Spontaneous Polarization," *Appl. Phys. Lett.*, vol. 12, pp. 209-&, 1968.
- [160] R. G. Batchko, V. Y. Shur, M. M. Fejer, and R. L. Byer, "Backswitch poling in lithium niobate for high-fidelity domain patterning and efficient blue light generation," *Appl. Phys. Lett.*, vol. 75, pp. 1673-1675, 1999.
- [161] K. T. Gahagan, V. Gopalan, J. M. Robinson, Q. Z. X. Jia, T. E. Mitchell, M. J. Kawas, T. E. Schlesinger, and D. D. Stancil, "Integrated electro-optic lens/scanner in a LiTaO3 single crystal," *Applied Optics*, vol. 38, pp. 1186-1190, 1999.
- [162] D. Psaltis and G. W. Burr, "Holographic data storage," *Computer*, vol. 31, pp. 52-+, 1998.
- [163] K. Kitamura, J. K. Yamamoto, N. Iyi, S. Kimura, and T. Hayashi, "Stoichiometric Linbo3 Single-Crystal Growth By Double Crucible Czochralski Method Using Automatic Powder Supply-System," *J. Cryst. Growth*, vol. 116, pp. 327-332, 1992.
- [164] L. Tian, V. Gopalan, and L. Galambos, "Domain reversal in stoichiometric LiTaO3 prepared by vapor transport equilibration," *Appl. Phys. Lett.*, vol. 85, pp. 4445-4447, 2004.

- [165] V. Gopalan, N. A. Sanford, J. A. Aust, K. Kitamura, Y. Furukawa, N. Hari Singh, M.Sc, and Ph.D, "Crystal growth, characterization, and domain studies in lithium niobate and lithium tantalate ferroelectrics," in *Handbook of Advanced Electronic and Photonic Materials and Devices* Burlington: Academic Press, 2001, pp. 57-114.
- [166] V. Gopalan, T. E. Mitchell, Y. Furukawa, and K. Kitamura, "The role of nonstoichiometry in 180 degrees domain switching of LiNbO₃ crystals," *Appl. Phys. Lett.*, vol. 72, pp. 1981-1983, 1998.
- [167] K. Kitamura, Y. Furukawa, K. Niwa, V. Gopalan, and T. E. Mitchell, "Crystal growth and low coercive field 180 degrees domain switching characteristics of stoichiometric LiTaO₃," *Appl. Phys. Lett.*, vol. 73, pp. 3073-3075, 1998.
- [168] V. Y. Shur, "Kinetics of ferroelectric domains: Application of general approach to LiNbO₃ and LiTaO₃," *Journal of Materials Science*, vol. 41, pp. 199-210, 2006.
- [169] S. C. Abrahams, E. Buehler, W. C. Hamilton, and S. J. Laplaca, "Ferroelectric lithium tantalate .3. Temperature-dependence of structure in ferroelectric phase and paraelectric structure at 940 degrees k," *J. Phys. Chem. Solids*, vol. 34, pp. 521-532, 1973.
- [170] I. Takanaga and J. Kushibiki, "Elastic constants of multidomain LiTaO₃ crystal," *J. Appl. Phys.*, vol. 86, pp. 3342-3346, 1999.
- [171] A. M. Glass, "Dielectric Thermal And Pyroelectric Properties Of Ferroelectric Litao₃," *Physical Review*, vol. 172, pp. 564-&, 1968.
- [172] R. Peierls, "The size of a dislocation," *Proc. Phys. Soc*, vol. 52, pp. 34-37, Jan 1940.
- [173] R. T. Smith and F. S. Welsh, "Temperature Dependence Of Elastic, Piezoelectric, And Dielectric Constants Of Lithium Tantalate And Lithium Niobate," *J. Appl. Phys.*, vol. 42, pp. 2219-&, 1971.
- [174] V. Gopalan and M. C. Gupta, "Observation of internal field in LiTaO₃ single crystals: Its origin and time-temperature dependence," *Appl. Phys. Lett.*, vol. 68, pp. 888-890, 1996.
- [175] W. D. Hsu, S. Tepavcevic, L. Hanley, and S. B. Sinnott, "Mechanistic studies of surface polymerization by ion-assisted deposition," *Journal of Physical Chemistry C*, vol. 111, pp. 4199-4208, 2007.
- [176] E. H. Sargent, "Solar Cells, Photodetectors, and Optical Sources from Infrared Colloidal Quantum Dots," *Adv. Mater.*, vol. 20, pp. 3958-3964, 2008.

- [177] A. L. Rogach, A. Eychmuller, S. G. Hickey, and S. V. Kershaw, "Infrared-emitting colloidal nanocrystals: Synthesis, assembly, spectroscopy, and applications," *Small*, vol. 3, pp. 536-557, Apr 2007.
- [178] A. A. R. Watt, D. Blake, J. H. Warner, E. A. Thomsen, E. L. Tavenner, H. Rubinsztein-Dunlop, and P. Meredith, "Lead sulfide nanocrystal: conducting polymer solar cells," *J. Phys. D-Appl. Phys.*, vol. 38, pp. 2006-2012, Jun 2005.
- [179] D. H. Cui, J. Xu, T. Zhu, G. Paradee, S. Ashok, and M. Gerhold, "Harvest of near infrared light in PbSe nanocrystal-polymer hybrid photovoltaic cells," *Appl. Phys. Lett.*, vol. 88, p. 3, May 2006.
- [180] K. P. Fritz, S. Guenes, J. Luther, S. Kumar, N. S. Saricifitci, and G. D. Scholes, "IV-VI nanocrystal-polymer solar cells," *J. Photochem. Photobiol. A-Chem.*, vol. 195, pp. 39-46, Mar 2008.
- [181] S. J. Kim, W. J. Kim, A. N. Cartwright, and P. N. Prasad, "Carrier multiplication in a PbSe nanocrystal and P3HT/PCBM tandem cell," *Appl. Phys. Lett.*, vol. 92, p. 3, May 2008.
- [182] A. M. Zachary, I. L. Bolotin, D. J. Asunskis, A. T. Wroble, and L. Hanley, "Cluster Beam Deposition of Lead Sulfide Nanocrystals into Organic Matrices," *Acs Applied Materials & Interfaces*, vol. 1, pp. 1770-1777, 2009.
- [183] M. A. Green, "Photovoltaics: technology overview," *Energy Policy*, vol. 28, pp. 989-998, 2000.
- [184] A. Goetzberger, C. Hebling, and H. W. Schock, "Photovoltaic materials, history, status and outlook," *Materials Science & Engineering R-Reports*, vol. 40, pp. 1-46, 2003.
- [185] V. I. Klimov, "Detailed-balance power conversion limits of nanocrystal-quantum-dot solar cells in the presence of carrier multiplication," *Appl. Phys. Lett.*, vol. 89, p. 3, Sep 2006.
- [186] M. C. Hanna and A. J. Nozik, "Solar conversion efficiency of photovoltaic and photoelectrolysis cells with carrier multiplication absorbers," *J. Appl. Phys.*, vol. 100, p. 8, Oct 2006.
- [187] M. T. Trinh, A. J. Houtepen, J. M. Schins, T. Hanrath, J. Piris, W. Knulst, A. Goossens, and L. D. A. Siebbeles, "In spite of recent doubts carrier multiplication does occur in PbSe nanocrystals," *Nano Lett.*, vol. 8, pp. 1713-1718, Jun 2008.
- [188] G. I. Koleilat, L. Levina, H. Shukla, S. H. Myrskog, S. Hinds, A. G. Pattantyus-Abraham, and E. H. Sargent, "Efficient, stable infrared photovoltaics based on solution-cast colloidal quantum dots," *ACS Nano*, vol. 2, pp. 833-840, May 2008.

- [189] J. M. Luther, M. Law, M. C. Beard, Q. Song, M. O. Reese, R. J. Ellingson, and A. J. Nozik, "Schottky Solar Cells Based on Colloidal Nanocrystal Films," *Nano Lett.*, vol. 8, pp. 3488-3492, Oct 2008.
- [190] A. D. Becke, "A New Mixing Of Hartree-Fock And Local Density-Functional Theories," *J. Chem. Phys.*, vol. 98, pp. 1372-1377, 1993.
- [191] C. T. Lee, W. T. Yang, and R. G. Parr, "Development Of The Colle-Salvetti Correlation-Energy Formula Into A Functional Of The Electron-Density," *Phys. Rev. B*, vol. 37, pp. 785-789, 1988.
- [192] S. H. Vosko, L. Wilk, and M. Nusair, "Accurate Spin-Dependent Electron Liquid Correlation Energies For Local Spin-Density Calculations - A Critical Analysis," *Can. J. Phys.*, vol. 58, pp. 1200-1211, 1980.
- [193] P. J. Stephens, F. J. Devlin, C. F. Chabalowski, and M. J. Frisch, "Ab-Initio Calculation Of Vibrational Absorption And Circular-Dichroism Spectra Using Density-Functional Force-Fields," *J. Phys. Chem.*, vol. 98, pp. 11623-11627, 1994.
- [194] A. F. Voter, "Parallel replica method for dynamics of infrequent events," *Phys. Rev. B*, vol. 57, pp. 13985-13988, 1998.
- [195] M. R. Sorensen and A. F. Voter, "Temperature-accelerated dynamics for simulation of infrequent events," *J. Chem. Phys.*, vol. 112, pp. 9599-9606, Jun 2000.
- [196] A. B. Bortz, M. H. Kalos, and J. L. Lebowitz, "New Algorithm For Monte-Carlo Simulation Of Ising Spin Systems," *Journal of Computational Physics*, vol. 17, pp. 10-18, 1975.
- [197] D. T. Gillespie, "General Method For Numerically Simulating Stochastic Time Evolution Of Coupled Chemical-Reactions," *Journal of Computational Physics*, vol. 22, pp. 403-434, 1976.
- [198] A. F. Voter, F. Montalenti, and T. C. Germann, "Extending the time scale in atomistic simulation of materials," *Ann. Rev. Mater. Res.*, vol. 32, pp. 321-346, 2002.
- [199] G. Henkelman and H. Jonsson, "A dimer method for finding saddle points on high dimensional potential surfaces using only first derivatives," *J. Chem. Phys.*, vol. 111, pp. 7010-7022, 1999.

- [200] D. Sheppard, R. Terrell, and G. Henkelman, "Optimization methods for finding minimum energy paths," *J. Chem. Phys.*, vol. 128, 2008.
- [201] J. Jacobsen, K. W. Jacobsen, P. Stoltze, and J. K. Norskov, "Island Shape-Induced Transition From 2d To 3d Growth For Pt/Pt(111)," *Phys. Rev. Lett.*, vol. 74, pp. 2295-2298, Mar 1995.
- [202] L. J. Xu and G. Henkelman, "Adaptive kinetic Monte Carlo for first-principles accelerated dynamics," *J. Chem. Phys.*, vol. 129, 2008.
- [203] G. Henkelman and H. Jonsson, "Long time scale kinetic Monte Carlo simulations without lattice approximation and predefined event table," *J. Chem. Phys.*, vol. 115, pp. 9657-9666, 2001.
- [204] A. F. Voter, "Hyperdynamics: Accelerated molecular dynamics of infrequent events," *Phys. Rev. Lett.*, vol. 78, pp. 3908-3911, 1997.
- [205] G. Henkelman and H. Jonsson, "Multiple time scale simulations of metal crystal growth reveal the importance of multiatom surface processes," *Phys. Rev. Lett.*, vol. 90, 2003.
- [206] P. Puri and V. Yang, "Effect of particle size on melting of aluminum at nano scales," *Journal of Physical Chemistry C*, vol. 111, pp. 11776-11783, 2007.

BIOGRAPHICAL SKETCH

Donghwa Lee was born in South Korea. He earned his bachelor's degree in materials science and engineering in 2004 from Korea University, South Korea. He joined the Department of Materials Science and Engineering at the University of Florida in 2005. He joined the doctoral degree at the University of Florida (UF), Gainesville. He started working with Prof. Hans J. Seifert for a year. After Prof. Seifert left, Lee joined the computational science focus group under Prof. Simon R. Phillpot. He received his M.S in materials science and engineering from the University of Florida in fall of 2007. He is completing his Ph. D. degree in August 2010. His research focused on using computational simulation methods to characterize different material system.